

University of *Ljubljana*  
Faculty of *Chemistry and Chemical Technology*



Doctoral programme in CHEMICAL SCIENCES

Field of CHEMICAL ENGINEERING

Doctoral dissertation

**Study of selected processes and parameters influencing the internal  
resistance in lithium–sulfur batteries**

**Študij vpliva izbranih procesov in parametrov na notranjo upornost  
litij–žveplovih akumulatorjev**

Sara Drvarič Talian

*Mentor: Assoc. Prof. Robert Dominko*

Ljubljana, 2018



Komisija za oceno primernosti teme in za oceno doktorske disertacije imenovana na seji senata UL FKKT dne 17. 3. 2017

Imenovanje mentorja na seji senata UL FKKT dne 16. 6. 2017

Komisija za zagovor imenovana na seji senata UL FKKT dne 21. 9. 2018

Datum zagovora: 9. 10. 2018

**Mentor: izr. prof. dr. Robert Dominko**

**Člani komisije za zagovor doktorske disertacije:**

prof. dr. Marija Bešter Rogač

Fakulteta za kemijo in kemijsko tehnologijo Univerze v Ljubljani

prof. dr. Miran Gaberšček

Kemijski inštitut, Ljubljana

zasl. prof. dr. Emanuel Peled

Tel Aviv University, Tel Aviv

Statement of authorship of the doctoral dissertation

I, Sara Drvarič Talian, confirm the authorship of the doctoral dissertation entitled: Study of selected processes and parameters influencing the internal resistance in lithium–sulfur batteries.

With my signature I declare that:

- The doctoral dissertation is the result of my individual work under the mentorship of Assoc. Prof. Robert Dominko.
- I have consistently cited all scientific literature used in the work.
- The electronic form of the doctoral dissertation is identical to the printed form.

Ljubljana, 23. 7. 2018

Sara Drvarič Talian

I would like to thank my family, friends and work colleagues for the support and help received during the years I was working on my doctoral dissertation. Every new idea, approach, a joke or a cup of tea was appreciated. I can say I have learned something valuable from each individual I spent time with.

*The scientist is not a person who gives the right answers; he's one who asks the right questions.*

*– Claude Lévi-Strauss*

## Izvelek

Čedalje večja potreba po energiji poleg povečanega vpliva na okolje pomeni tudi večji pritisk na raziskovalce s področja elektrokemije in znanosti o materialih. Pospešeno se iščejo zanesljivi shranjevalniki električne energije z visoko energijsko gostoto. Novejšo alternativo predstavljajo litij-žveplov akumulatorji, ki zaradi lažjega, dostopnejšega in cenejšega katodnega materiala ter možnosti izmenjave dveh elektronov na žveplu obetajo ugodnejšo teoretično specifično kapaciteto in energijsko gostoto.

Za razumevanje dosežene napetosti, kapacitete, moči in energije akumulatorja je predvsem potrebno razumeti procese, ki med njegovim delovanjem potekajo ter kateri izmed njih to delovanje omejujejo. Vplive posameznih procesov si lahko predstavljamo kot prispevke k notranji upornosti akumulatorja, iz tega vidika pa je bila pripravljena tudi ta doktorska disertacija.

Najprej smo določili vpliv fizikalnokemijskih lastnosti elektrolitov na osnovi ionske tekočine na notranjo upornost in delovanje litij-žveplovih akumulatorjev. S tem znanjem smo se usmerili v iskanje elektrolitov z zmanjšano topnostjo polisulfidnih intermediatov, kar smo uspeli doseči z uporabo fluoriranih etrov. Na osnovi takega elektrolita smo uspešno pripravili visokoenergijsko celico z majhno količino dodanega elektrolita.

Razločitev med prispevki anode in katode k notranji upornosti je bila opravljena s testi simetričnih celic. Ugotovili smo, da ima v izbranih elektrolitih reakcija in difuzija  $\text{Li}^+$  iona na anodi v primerjavi s pozitivno elektrodo majhen prispevek, ki se med delovanjem akumulatorske celice še zmanjšuje. Zato smo se osredotočili na katodne prispevke elektrokemije polisulfidov na elektrodah iz ogljika. Vpliv kemijske reakcije in prispevka difuzije na notranjo upornost je bil raziskan na sistemu s poenostavljeno geometrijo, preko katerega smo uspeli nedvoumno določiti izvor ter velikost prispevkov elektrokemije polisulfidov na ogljikovih elektrodah. Zaznana in opisana je bila tudi disproporcionacija polisulfidnih zvrsti.

S sestavo poenostavljenih akumulatorskih celic (steklasti ogljik|Li) so bili prispevki k notranji upornosti Li-S akumulatorske celice bolj natančno raziskani, s tem pa smo dopolnili razumevanje impedančnih spektrov »tradicionalnih« akumulatorskih celic s poroznimi katodami. Opisan je bil tudi vpliv neprevodnega filma  $\text{Li}_2\text{S}$ , ki v celici nastaja kemijsko in elektrokemijsko. Zaradi tvorbe poroznih struktur ta film ne pasivira elektrode, kljub temu pa zaradi osiromašenja elektrolita znatno vpliva na notranjo upornost in delovanje Li-S akumulatorja. Tako smo dosegli boljše razumevanje impedančnega odziva Li-S akumulatorskih celic in omejitev pri njihovem delovanju.

**Ključne besede:** Li-žveplov akumulator, impedančna spektroskopija, notranja upornost, elektroliti, fizikalno-kemijske lastnosti, disproporcionacija, mehanizem odlaganja  $\text{Li}_2\text{S}$ , osiromašenje elektrolita

## Summary

The increasing world's energy demands are resulting in an escalation of the pressure on the environment as well as a boost in the electrochemical field of science for research and development of new, reliable and high energy sources. Li–sulfur secondary batteries are one of the prominent possibilities of future battery systems with a promise of better theoretic specific capacities and energy densities.

In order to understand the achieved voltage, capacity, power and energy of a Li-S battery, it is paramount to understand the processes which take place during its operation and which of them limit its performance. The influence of a given process can be visualized by the size of its contribution to the internal resistance of the battery. This is also the stand point, from which the research in this dissertation has been conducted.

Starting with the electrolyte resistance, the influence of the electrolyte's physicochemical properties on battery performance was evaluated by the use of an electrolyte system based on an ionic liquid. Since this study showed that the solubility of polysulfides in the electrolyte is a very important parameter, our focus shifted to electrolytes with fluorinated ether compounds, which showed sparing solubility of  $\text{Li}_2\text{S}_x$  species. Fluorinated ether electrolytes were also used to construct high-energy cells with low electrolyte amount.

The charge-transfer reaction and diffusion contributions from the anode and the cathode were distinguished using symmetrical cells. We have learned that the anode's contributions in the used electrolytes are significantly smaller than the cathode contribution and even reduce in size with further cycling. We therefore focused on studying polysulfide electrochemistry on carbon surfaces. The cell setup was simplified by using glassy carbon electrodes. With that, we were successful in identifying the origin of each contribution. Disproportionation of polysulfides was also detected and evaluated.

By assembly of simplified full cells (glassy carbon||Li), the contributions to the internal resistance of Li–S battery cells was studied. This knowledge was then used to complete the understanding of the impedance spectra of a “conventional” porous cathode Li–S cell. The deposition of  $\text{Li}_2\text{S}$ , which forms electrochemically and chemically in the cell, was also described. Since this film forms porous structures, the electrode is not passivated, although this process still significantly influences the total internal resistance due to polysulfide species depletion. In summary, this work enabled thorough understanding of the Li–sulfur battery impedance response and provided insight into the reasons behind its performance limitations.

**Keywords:** Li–sulfur battery, impedance spectroscopy, internal resistance, electrolyte, physicochemical properties, disproportionation,  $\text{Li}_2\text{S}$  film formation, electrolyte depletion.

## Index

Izvleček	v
Summary	vi
Index	vii
List of abbreviations	x
List of symbols	xi
List of publications from the doctoral thesis work	xii
1 Introduction.....	1
1.1 Definition of a battery and its components .....	1
1.2 Primary and secondary battery technology history .....	2
1.3 Battery characteristics .....	3
1.3.1 Voltage .....	3
1.3.2 Capacity.....	4
1.3.3 Other characteristics .....	4
1.4 Techniques used for battery characterization .....	5
1.5 Lithium–sulfur batteries .....	7
1.5.1 Mechanism of operation .....	7
1.5.2 Problems and challenges.....	9
1.5.3 Common materials and parameters.....	11
1.5.4 Li–S battery impedance.....	14
2 Aim and hypotheses of the thesis .....	15
3 Materials and methods.....	17
3.1 A list of used materials .....	17
3.2 Battery components preparation and cell assembly .....	18
3.2.1 Cathode manufacturing and polysulfide synthesis.....	18
3.2.2 Preparation of electrolyte solutions .....	18
3.2.3 Cell assembly.....	19
3.3 Electrochemical measurements.....	19
3.3.1 Galvanostatic experiments.....	20
3.3.2 Impedance spectroscopy .....	20

3.4	Other analyses .....	22
3.4.1	Determination of electrolyte physicochemical properties.....	22
3.4.2	UV-vis spectroscopy .....	23
3.4.3	IR spectroscopy.....	23
3.4.4	Scanning electron microscopy .....	24
3.4.5	X-ray absorption spectroscopy .....	25
4	Results and discussion .....	26
4.1	High frequency resistive intercept contribution (electrolyte investigation) .....	29
4.1.1	Influence of the electrolyte's physicochemical properties on battery performance.....	30
4.1.2	Electrolytes with poor polysulfide solubility .....	40
4.2	Reaction and diffusion contributions in the Li–S impedance spectra.....	50
4.3	Anode's contribution .....	53
4.3.1	Lithium reaction with polysulfides.....	53
4.4	Cathode's contribution .....	59
4.4.1	Investigation of polysulfide electrochemistry on carbon surfaces .....	60
4.4.2	Porous carbon cathode impedance.....	70
4.4.3	Cathode impedance change with SOC and the origin of Li–S capacity limitation.....	72
5	Conclusions.....	84
6	Razširjen povzetek v slovenskem jeziku .....	88
6.1	Litij–žveplovevi akumulatorji.....	88
6.1.1	Mehanizem delovanja .....	88
6.1.2	Težave in izzivi.....	88
6.1.3	Pogosto uporabljani materiali.....	89
6.1.4	Notranja upornost Li–S akumulatorja .....	91
6.2	Hipoteze .....	92
6.3	Rezultati in diskusija.....	93
6.3.1	Visokofrekvenčni odsek na realni osi.....	94
6.3.2	Anodni prispevek k notranji upornosti .....	100
6.3.3	Katodni prispevek k notranji upornosti .....	101
6.4	Zaključek.....	108

7	Literature .....	112
8	List of figures .....	121
9	List of tables.....	127
10	Attachments .....	128

## List of abbreviations

AC	Alternating current
ACV	Alternating current voltammetry
CV	Cyclic voltammetry
DC	Direct current
DEME	N,N-Diethyl-N-methyl-N-(2-methoxyethyl)ammonium cation
DOL	1,3-dioxolane
FIB	Focused ion beam
GITT	Galvanostatic intermittent titration technique
GC	Glassy carbon
HSAL	High surface area lithium
ILq	Ionic liquid
Li-ion	Lithium-ion
Li-S	Lithium-sulfur
OCV	Open circuit voltage
SEI	Solid electrolyte interphase
SEM	Scanning electron microscope
TDI	4,5-dicyano-2-(trifluoromethyl)imidazole anion
TEGDME	Tetraglyme
TFEE	1,1-(1,1,2,2-tetrafluoroethoxy)ethane
TFSI	bis(trifluoromethanesulfonyl)imide anion
XAS	X-ray absorption spectroscopy
XRD	X-ray diffraction

## List of symbols

$E_{\text{cell}}$	Cell open circuit voltage	$\phi$	Phase shift
$E^0$	Standard cell potential	$\omega$	Angular frequency
$R$	Gas constant	$\pi$	Number pi
$T$	Temperature	$\nu$	Frequency
$z$	Number of electrons transferred	$X$	Molar ratio
$F$	Faraday's constant	$\kappa$	Conductivity
$a$	Activity	$\rho$	Density
$\Delta G$	Gibbs free energy	$C_{\text{dl}}$	Double layer capacitance
$V$	Cell potential	$I_0$	Exchange current
$\eta$	Overpotential	$A$	Surface area
$I$	Current	$k^0$	Rate constant of the reaction
$R_{\Omega}$	(Ohmic) resistance	$c$	Concentration
$C$	Capacity	$\alpha$	Transfer coefficient
$t$	Time	$D$	Diffusion coefficient
$q$	Coulombic efficiency	$L$	Diffusion length
$Q$	Charge	$\varepsilon$	Porosity
$E$	Energy	$\tau$	Tortuosity
$Z$	Impedance	$p, q$	Stoichiometric factors

## List of publications from the doctoral thesis work

Drvarič Talian, S; Moskon, J; Dominko, R; Gaberscek, M: Reactivity and Diffusivity of Li Polysulfides: A Fundamental Study Using Impedance Spectroscopy. *ACS Appl. Mater. Interfaces*, **2017**, *9*, 29760–29770, IF 8.0.

Drvarič Talian, S; Bešter-Rogač, M; Dominko, R: The physicochemical properties of a [DEME][TFSI] ionic liquid-based electrolyte and its influence on the performance of lithium–sulfur batteries. *Electrochim. Acta*, **2017**, *252*, 147–153, IF 5.1.

Drvarič Talian, S; Jeschke, S; Vizintin, A; Pirnat, K; Arčon, I; Aquilanti, G; Johansson, P; Dominko, R: Fluorinated Ether Based Electrolyte for High-Energy Lithium–Sulfur Batteries: Li<sup>+</sup> Solvation Role Behind Reduced Polysulfide Solubility. *Chem. Mater.*, **2017**, *29*, 10037–10044, IF 9.9.

Drvarič Talian, S; Kapun, G; Moškon, J; Dominko, R; Gaberšček, M: Does deposition of Li<sub>2</sub>S indeed limit the operation of a Li-S system? *Submitted*.

## 1 Introduction

The modern world is practically run on electricity. Consequently, very few individuals would know or want to survive in a world without lightbulbs, cars, computers, phones or other various household or kitchen appliances. Batteries are one of the forefront players in the field of electrical energy providing devices. This is a result of an increasing amount of gadgets striving for portable versions, the ability of producing them in assorted, often lightweight forms and due to the possibility of applications in various fields ranging from small toys, phones or lap-tops and all the way to electrically powered cars, trains or planes. Since global warming issues became more pressing and a quest to diverge away from fossil fuels began, the latter – transportation – technology is becoming progressively developed. Another important battery application stems from the fact that renewable energy sources (wind or solar power) usually provide surges of energy at intermittent times, which needs to be stored in batteries for use when energy is not directly available.

With all of these technological advances, of course, follows a wide field of battery research, a small part of which is described in this work.

### 1.1 Definition of a battery and its components

An electrochemical cell is a unit that provides electrical energy on the basis of chemical energy, which is stored inside it. Strictly speaking, a battery is defined as a device consisting of two or more connected electrochemical cells, but the usage of the word by the consumers more often indicates the product which is powering the device, no matter how many electrochemical cells it contains. The chemical energy stored inside the cells is used on the basis of electrochemical reactions taking place on its electrodes. These can be irreversible and the battery is called a primary one, or reversible, when the battery can be recharged and is labelled a secondary battery.<sup>1</sup>

A cell consists of three main active components:

- **Negative electrode**, where during discharge electrochemical oxidation takes place. It is often called the anode. From the anode, the electrons move through the external circuit towards the opposite electrode (Figure 1a). When charging the cell, the reaction is reversed and reduction occurs (Figure 1b).
- **Positive electrode**, where reduction reaction occurs during discharge, also called the cathode. There, electrons are being accepted by the chemical elements or compounds. Similarly, during charge, the reactions are reversed.

- **Electrolyte** provides closure to the circuit by enabling the ion transport between the electrodes. It usually consists of a solution of salts in aqueous or nonaqueous mixture of solvents. Ionic liquid based, polymeric or solid electrolytes have also been applied.<sup>2</sup>

When charging a battery, the terminology of the electrodes – the cathode and the anode – is usually reversed, following the consensus of naming them according to what reaction is taking place.<sup>2</sup> In this work, however, the term cathode will always be used for the positive electrode and the term anode for the negative one, regardless, whether discharging or charging of the battery cell is taking place.

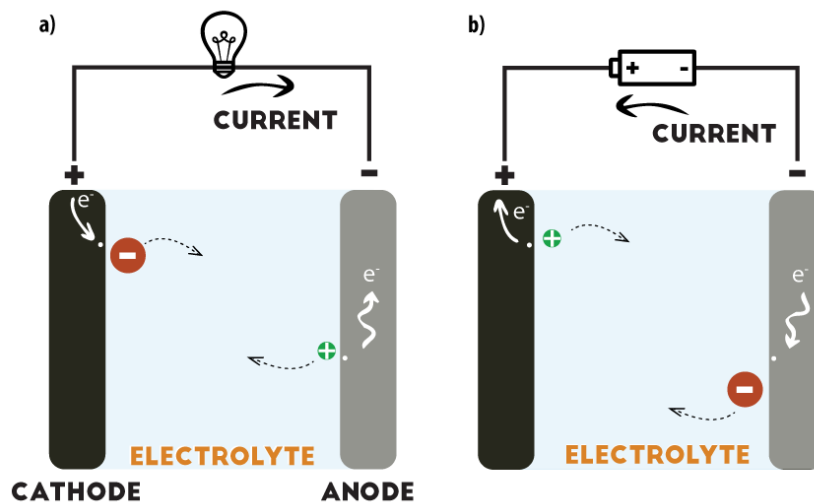


Figure 1: Battery operation during a) discharge and b) charge.

The inactive components of the battery cell consist of the casing and the separator. The latter is included for the prevention of electronic contact between the electrodes which would discharge the battery through the internal short circuit. At the same time ionic current in the electrolyte should not be hindered. The most common form of separators in modern batteries is a thin plastic or glassy fibre sheet with sufficient pore volume intended for electrolyte retention.<sup>1</sup>

## 1.2 Primary and secondary battery technology history

Alessandro Volta, who assembled a copper–zinc cell in 1800, is usually referred to as the father of the first battery. On the other hand, the pioneer practical battery was the Daniell cell built in 1836 by John Frederic Daniell. This one was based on the same redox couple, but solved some of its issues by using two different electrolytes separated with a membrane. The next big breakthrough came from Georges Leclanche in 1886, when primary battery consisting out of zinc and carbon was constructed.<sup>3</sup>

The first secondary battery that could be recharged by passing through a reverse current is the lead-acid cell. It was invented by Gaston Planté in 1859 and consisted out of a lead anode and lead dioxide cathode, both of which were immersed in a solution of sulfuric acid.<sup>4</sup> From then on, the work on batteries expanded into the field of alkaline solutions, which were developed almost simultaneously in Sweden by Jungner (nickel–cadmium battery) and in USA by Edison (nickel–iron battery).<sup>3</sup>

Today, primary and secondary batteries are available in a variety of different sizes and electrochemistries. In the past few decades, primary zinc batteries from Leclanche were improved to alkaline batteries and a myriad of advances were made on lead–acid batteries. They are still one of the best known systems and are used in large quantities in the automotive field and valued for the high currents they can produce. Alongside, completely different technologies were developed and marketed, for example the nickel–metalhydride and lithium–ion (Li–ion) batteries.<sup>5</sup>

### 1.3 Battery characteristics

The most important characteristics of a battery are its voltage and capacity. Besides that, Coulombic efficiency, energy, internal impedance and self-discharge rate could also be of great importance. With capacity and energy, specific or density values are commonly acquired, which give the value per mass or volume of the active material in the battery cell (the weight or volume of other battery components is usually not taken into account).<sup>5</sup>

#### 1.3.1 Voltage

Voltage is the difference in potentials of the two electrodes, which depend upon the chemical nature of the reactions and also other factors such as temperature and concentrations (Equation 1).<sup>2</sup> The open circuit voltage (OCV,  $E_{cell}$ ) is defined as Equation 2.<sup>1</sup> The thermodynamic data of the cell reactions can be used to derive the cell voltage in the reversible battery system through Equation 3.<sup>6</sup>

$$E_{cell} = E^0 - \frac{RT}{zF} \ln \frac{a_{products}}{a_{reactants}} \quad (1)$$

$$E_{cell} = E_{cathode} - E_{anode} \quad (2)$$

$$\Delta G = -zFE^0 \quad (3)$$

When the cell is under load, its voltage depends on the current, temperature, state of charge and its history.<sup>1</sup> Because of polarization phenomena and internal ohmic resistance, the cell can never be discharged at its theoretical voltage.

The polarization comprises of two different contributions – activation and concentration polarization. The activation polarization measures the difficulty of the charge transfer reaction from a kinetic standpoint. The concentration polarization on the other hand is connected with accumulation or depletion of the active material near the electrode's surface, which is caused by difficulty of diffusion away from or towards the electrode, where it is formed or being used. Both are present at the positive and at the negative electrode (Equation 4,  $\eta_+$ ,  $\eta_-$ ).<sup>2</sup> When current is flowing through an external circuit, the potential inside the cell is also changed due to ohmic polarization which consists of the resistance of the electrolyte and the contact resistances between the battery cell components (Equation 4,  $R_\Omega$ ).<sup>6</sup>

$$V = E_{cell} - (\eta_a + \eta_c)_+ - (\eta_a + \eta_c)_- - IR_\Omega \quad (4)$$

### 1.3.2 Capacity

The capacity of a battery is defined as the electrical charge that can be drawn from the battery (Equation 5).

$$C = \int_0^t I(t) \cdot dt \quad (5)$$

The discharge parameters that influence the capacity reached are the current used, the voltage cut-off limits, temperature and active mass loading. Besides that, the history of the battery cell should also be taken into consideration when comparing capacity data.<sup>1</sup>

More commonly, the measure of specific capacity is used, where the capacity value is divided with the mass of the active material inside the cell ( $\text{Ah kg}^{-1}$ ).

### 1.3.3 Other characteristics

When secondary battery is charged, the electrical energy from an external power source is being transformed to chemical energy inside the battery cell. The charge used for this ( $Q_c$ ) is usually greater than the charge delivered in the next discharge ( $Q_d$ ). This is due to incomplete conversion of the current to chemical energy, because of side reactions or in some cases also

due to particles disconnection from the composite electrode. The charging efficiency is expressed as **Coulombic efficiency** ( $q$ ) by Equation 6.<sup>2</sup>

$$q = \frac{Q_d}{Q_c} \quad (6)$$

**Energy** of the battery is a function of both the voltage and the current (Equation 7). Since capacity measurements are usually conducted with galvanostatic experiments, energy is calculated by multiplying the measured capacity with the average discharge voltage. As is the case of capacity, specific energy ( $\text{Wh kg}^{-1}$ ) or energy density ( $\text{Wh L}^{-1}$  or  $\text{Wh cm}^{-3}$ ) is often stated.<sup>1</sup>

$$E = \int_0^t U(t) \cdot I(t) \cdot dt \quad (7)$$

**Internal impedance** of a battery is given as Equation 8.  $Z_+$  and  $Z_-$  are the sum of the impedance of both the positive and the negative electrodes, while  $R_\Omega$  corresponds to the internal ohmic resistance<sup>6</sup> as described in Section 1.3.1. Impedance characterizes the resistance that a battery gives when the current flows.

$$Z = Z_+ + Z_- + R_\Omega \quad (8)$$

Impedance is a complex characteristic and is usually determined with impedance spectroscopy, where small amplitude alternating current (AC) of different frequencies is applied.<sup>1</sup>

**Self-discharge** is the loss of charge with the battery being idle and at open circuit voltage. With different chemistries, the reason behind self-discharge can be different.<sup>1</sup> With Li–S batteries it is described in Section 1.5.2.

## 1.4 Techniques used for battery characterization

Techniques used for determination of most common battery characteristics (summarized in Section 1.3) are usually galvanostatic (chronopotentiometric) experiments, which give the voltage vs. capacity characteristic as pictured in Figure 2 and impedance spectroscopy for battery impedance determination. Other electrochemical techniques that are also commonly

used are cyclic voltammetry (CV), potentiostatic (chronoamperometric) experiments and when dealing with precipitation of solids also electrochemical quartz crystal microbalance (eQCM). All of these aforementioned methods are non-destructive.

For elucidation of material properties or mechanisms during battery operation, complementary analytical tools can be used. These are usually destructive and require disassembly of previously used cells, although in some cases, special electrochemical cells have been developed for *operando* measurements. Examples of various techniques are X-ray absorption spectroscopy (XAS), X-ray diffraction (XRD), numerous modes of microscopy or spectroscopy, tools for determination of electrolyte's physicochemical properties or similar complementary techniques for other characterisations, such as pore size determination.<sup>6</sup>

## 1.5 Lithium–sulfur batteries

Li-ion batteries, which have been thoroughly studied and widely commercialized in the past decades, exhibit some drawbacks which are hard to work around. Their energy density ( $300 \text{ Wh kg}^{-1}$ ) limits the use of the technology in electric automobiles, which in turn have a low driving range (cca 350 km), before the batteries need to be recharged. The cathode material is usually comprised of lithiated oxides of transition metals and represents the biggest restriction in the case. Most of those elements can accept only one electron per active atom, which results in a specific theoretic capacity of the batteries below  $300 \text{ mAh g}^{-1}$ . Furthermore, the technology is also facing high production costs with the use of cobalt or nickel cathode materials.<sup>7</sup>

Lithium–sulfur batteries, which employ lighter, easily accessible and cheaper cathode materials, represent a newer alternative. Since sulfur enables a two electron per mole redox reaction, lithium–sulfur batteries promise better theoretic specific capacities ( $1675 \text{ mAh g}^{-1}$ ) and energy densities ( $2500 \text{ Wh kg}^{-1}$ ).<sup>7,8</sup>

### 1.5.1 Mechanism of operation

Lithium–sulfur batteries work on the basis of sulfur reduction to lithium polysulfides ( $\text{Li}_2\text{S}_n$ ) and  $\text{Li}_2\text{S}$ .<sup>9</sup> In Figure 2, a typical galvanostatic response from a Li–S cell is depicted. The bottom part of the curve applies to the discharging of the cell and the upper part to charging. The higher voltage plateau at 2.3–2.4 V corresponds to the conversion of solid sulfur to soluble polysulfides and the lower plateau at 2.1–2.0 V to the reduction of the polysulfides towards an insoluble lithium sulfide.<sup>10</sup>

A Li–S battery cell is usually constructed out of a composite cathode consisting of sulfur in a carbon matrix, Li metal foil as the anode and a separator filled with the electrolyte (Figure 2-1).<sup>11</sup> Through discharge, the sulfur in the cathode gets dissolved and reduced to lithium polysulfide species, which are soluble in the electrolyte. As long as undissolved solid sulfur is present, the potential remains close to constant (high voltage plateau, Figure 2-2).<sup>12</sup> When the active mass is reduced to soluble polysulfides the voltage drops (Figure 2-3). The final product,  $\text{Li}_2\text{S}$ , starts to form and due to reduced solubility precipitate on the electrode surface. This happens throughout the lower voltage plateau (Figure 2-4).<sup>13</sup> Ideally, at the end of discharge, all of the sulfur would be deposited back on the electrode surface in the form of lithium sulfide (Figure 2-5). Through discharge, Li is oxidized and stripped away from the surface as  $\text{Li}^+$  ions.<sup>8</sup>

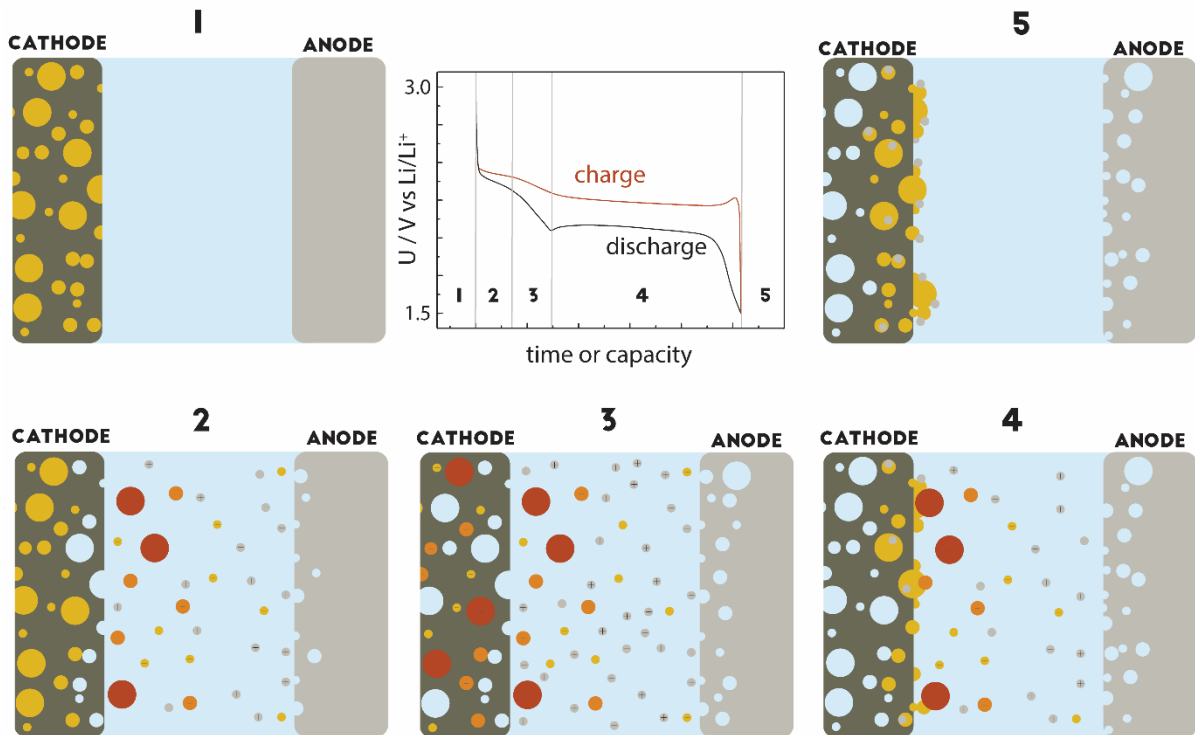


Figure 2: Stages of discharge of Li–S battery. Yellow, red and orange circles represent sulfur and different length polysulfide species. Grey circles represent  $\text{Li}^+$  ions formed by Li stripping.

In charging, the processes are generally reversed, although  $\text{Li}_2\text{S}$  dissolution and sulfur deposition phenomena are sometimes not temporally separated (Figure 3, cathode), which gives rise to a single charge plateau.<sup>14</sup> A problem which also arises is electrodeposition of lithium on its metal surface, which forms dendrites (Figure 3, anode). In Li-ion batteries, this problem was avoided by incorporating Li inside a graphite matrix. Although solving the dendrite problem, the use of graphite anode unfortunately lowers the capacity of the cell.<sup>15</sup>

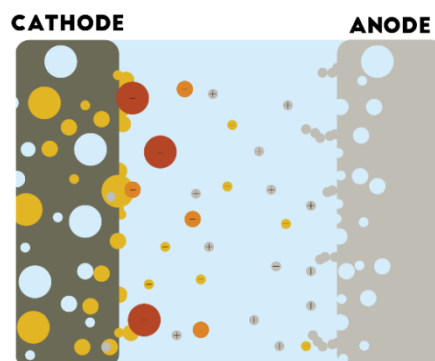


Figure 3: Schematic depiction of Li-S battery during charge with solid sulfur and  $\text{Li}_2\text{S}$  forming on the cathode and lithium dendrites on the anode. Yellow, red and orange circles represent sulfur and different length polysulfide species. Grey circles represent  $\text{Li}^+$  ions in solution and Li atoms deposited in dendritic form.

### 1.5.2 Problems and challenges

Multiple factors impede the commercialization of the Li–S technology. The first one is the insulating nature of sulfur and the final discharge product,  $\text{Li}_2\text{S}$ . This means that for fabrication of the positive electrodes, conductivity additives must be included, which dilute the active mass. Furthermore, the final discharge precipitate ( $\text{Li}_2\text{S}$ ) can cover the available surface area of the electrode or clog its pores (Figure 4) and increase the energy needed for further electrochemical reactions.<sup>16</sup>

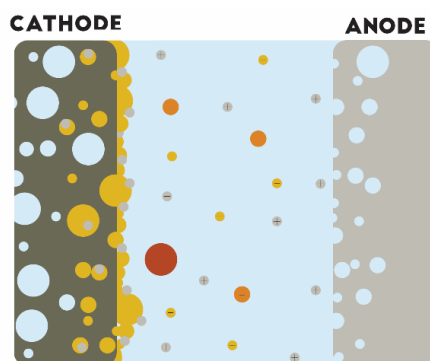


Figure 4: Insulating nature of the final discharge product can cause clogging of the available positive electrode surface area. Yellow, red and orange circles represent sulfur and different length polysulfide species. Grey circles represent  $\text{Li}^+$  ions formed by Li stripping.

When discharging the cell, an additional problem can arise from the difference of densities between the starting elemental sulfur and the final product,  $\text{Li}_2\text{S}$ , which would correspond to an almost 80% of volumetric expansion. That change could collapse the pore structure of the positive electrode and result in poor electronic connections and lower capacities.<sup>17</sup>

Lithium–sulfur battery cells have poor charging coulombic efficiency due to the polysulfide redox shuttle effect. Long-chain polysulfides are soluble in the used electrolytes and can also pass through the separator pores to the anode surface (Figure 5).

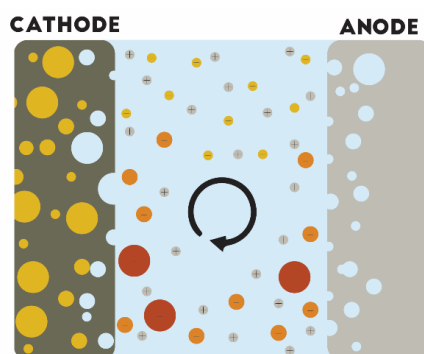


Figure 5: Polysulfide redox shuttle phenomenon. Yellow, red and orange circles represent sulfur and different length polysulfide species. Grey circles represent  $\text{Li}^+$  ions formed by Li stripping.

This means that during charging, the long-chain polysulfides migrate through the separator and get reduced to short-chain polysulfides on the anode instead of getting completely oxidized to sulfur on the cathode. These short-chain species can diffuse back, get oxidized and the cycle continues. In practice this phenomenon causes loss of active material and difficulty in completely charging the battery. For a similar reason, lithium–sulfur batteries also exhibit high self–discharge rate (Figure 6).<sup>18</sup>

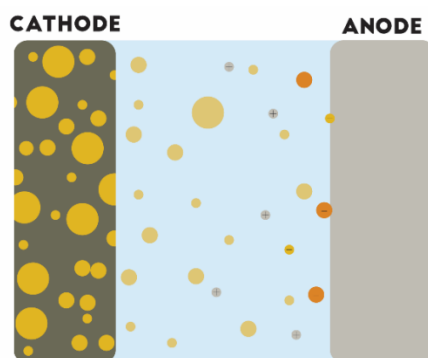


Figure 6: Self-discharge phenomenon in Li–S batteries due to dissolution of sulfur from the cathode. Yellow, red and orange circles represent sulfur and different length polysulfide species. Grey circles represent  $\text{Li}^+$  ions.

A special problem that becomes prominent at high current densities are lithium dendrites, which form due to uneven electrocrystallization of metallic lithium (Figure 7). These can in time grow through the porous separator and form an internal short circuit in the cell.<sup>19</sup>

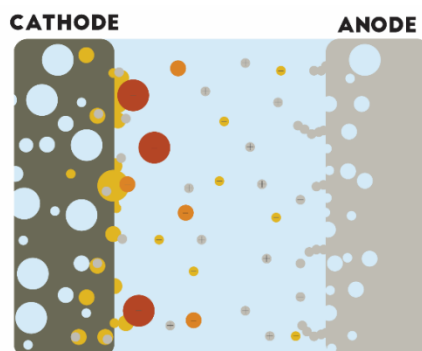
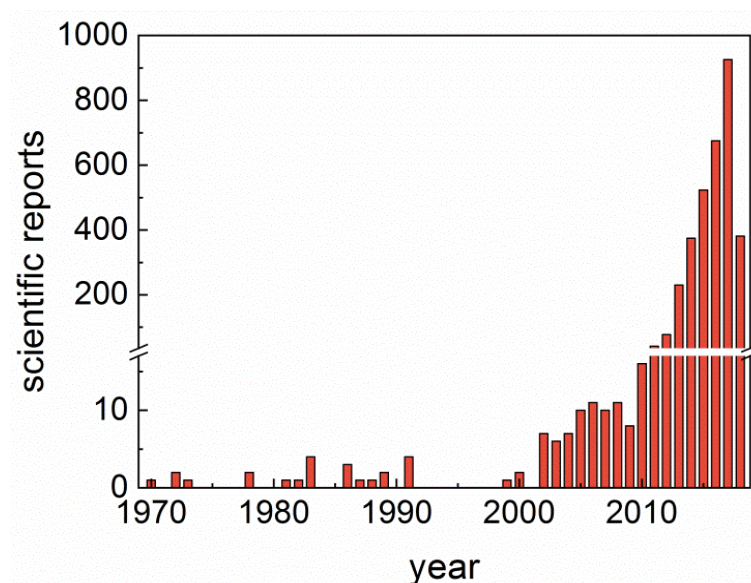


Figure 7: Dendritic growth of lithium during charging. Yellow, red and orange circles represent sulfur and different length polysulfide species. Grey circles represent  $\text{Li}^+$  ions in solution and Li atoms deposited in dendritic form.

### 1.5.3 Common materials and parameters

In the 1960s, when the first patent on the topic of a Li–S battery was filed<sup>20</sup>, the number of publications were few. The setup of the cell was generally very similar to the modern one – lithium anode, organic electrolyte and sulfur, which was mixed with a carbon additive and attached to the current collector to form the cathode<sup>21–23</sup> or added as the electrolyte (catholyte) solution in the form of polysulfides<sup>24</sup>. Polysulfide electrochemistry was studied<sup>25</sup> and modifications in the electrolyte composition made<sup>26</sup> with the final goal of transforming the battery system into a rechargeable one<sup>27</sup>.

The interest in the technology resurfaced in the beginning of the new millennium, when polymeric electrolytes were investigated<sup>28–32</sup>. After 2010, the number of reports drastically increased (Figure 8). Consequently, there were 926 publications in 2017 dealing with the topic, proving a wide appeal of the technology with researchers coming from almost 50 different countries.<sup>33</sup> With that amount of work done on the system it is therefore hard to fully recap all the research. Here the common materials applied and reasons behind the proposed improvements will be discussed. The summary will be made for the active battery parts (the electrodes and the electrolyte) as well as the separator.



### **a) Electrodes**

Cathode manufacturing for Li–S batteries is a process with multitude of parameters that could be controlled or changed. Although starting with a fully charged battery (elemental sulfur) is most common, reports about cathode materials consisting of  $\text{Li}_2\text{S}$ <sup>34–37</sup> and polysulfide species were also made, the latter being of special interest for redox flow batteries<sup>38–40</sup>.

Sulfur is a nonconductive substance, so it is important to mix it with conductivity additives (usually carbons) before cathode preparation. There are multiple ways of how incorporation of sulfur particles inside a carbon matrix is achieved. Available reports offer the options of melt<sup>41</sup>, vapor phase<sup>42</sup> or solution infiltrations<sup>43</sup>, mechanical intrusions<sup>44</sup> and chemical reaction depositions<sup>45</sup>.

Of course, choosing just any carbon won't give the best battery performance. One of the concepts for minimizing the extent of the polysulfide shuttle is encapsulation of sulfur, which could supposedly reduce the polysulfide dissolution and diffusion. Common materials used for this vary from carbon black materials<sup>46</sup>, nanotubes<sup>18,47</sup>, carbon nanofibers<sup>48</sup> to reduced graphene oxide<sup>49</sup> and graphene<sup>50</sup>. Here, the properties of those matrixes are important – their surface area, pore size and pore size distribution<sup>8</sup>. Other than carbon, metal oxides are also of interest, since the surface modifications of the material could enhance the polysulfide adsorption and entrapment.<sup>44,51,52</sup>

In the end, the cathode performance is conditioned by not only its porous matrix structure, but also by the loading of sulfur<sup>53</sup>, the thickness of the electrode<sup>54</sup>, binders and solvents used during its manufacturing<sup>55</sup>.

The surface of the lithium metal foil used in Li–S batteries is constantly changing due to reactions with the electrolyte and polysulfide species that diffuse through the separator. These phenomena produce a passivation layer called the solid electrolyte interphase (SEI). The electrode also changes due to aforementioned dendritic growth.<sup>56</sup> Everything combined equals to a need of a large excess of Li inside the cell. Protection of lithium is usually done on three different bases – either by electrolyte alterations, separator alterations or lithium surface modifications, which range from ex-situ<sup>57,58</sup> and in-situ<sup>59,60</sup> formations of stable passive layers to using Li alloys.<sup>19,61</sup>

### **b) Electrolyte**

For use in batteries in general, electrolytes must allow for easy ion transport (having good ionic conductivity), while also being electronically insulating in order to minimize self-discharge. They should be stable thermally, electrochemically and mechanically and should not be toxic. The solvent used in the electrolyte should enable sufficient supporting salt dissolution (high dielectric constant), while still maintaining low viscosity. Because these

demands are sometimes contradicting, binary mixtures of electrolytes and solvents are usually used to merge different physical and chemical properties sought for.<sup>62</sup> Besides basic guidelines, the role of physicochemical properties of electrolytes in the Li–S batteries is not thoroughly understood.

Through the discharge, the electrolyte inside the Li–S battery acts in various roles in the processes of dissolution, oxidation/reduction reactions and crystallization. First few reports of polysulfide electrochemistry research were with the use of tetrahydrofuran based electrolytes.<sup>25</sup> Today the field varies, although linear and cyclic ethers are most commonly used, usually employing the lithium bis(trifluoromethanesulfonyl)imide (LiTFSI) salt.<sup>16</sup>

Besides the solvents mentioned, an interesting group of electrolytes are also ionic liquids (ILq). They not only exhibit low volatility, good thermal stability and high conductivity but they also illustrate lower polysulfide solubilities, which could hinder the extent of polysulfide redox shuttle.<sup>63</sup> Designing ionic liquids for Li–S battery application usually means changing the cation structure, while anions typically remain the same as in Li<sup>+</sup> salts.<sup>64</sup> Again, the most common one is [TFSI], which supposedly enhances the formation of an effective and stable SEI on the anode.<sup>65</sup> Ionic liquids can be used on their own or in a combination with other solvents to adjust the desired properties.<sup>66</sup>

All solid state Li–S batteries<sup>67</sup> and ones with polymer electrolytes<sup>29,68–71</sup> are also of interest in the field, since their use could reduce the loss of active material, improve Coulombic efficiencies during cycling and minimize the otherwise high self-discharge rate, all caused due to high rates of polysulfide dissolution.<sup>63</sup>

Changing the electrolyte is a simple way of how to incorporate beneficial additives inside the cell. The most “famous” one for Li–S batteries is LiNO<sub>3</sub><sup>72</sup>, which is supposed to preserve the metal anode, suppress the redox shuttle and through that increase the Coulombic efficiencies and sulfur utilization.<sup>73</sup> Besides nitrates, a number of different organic or inorganic additives have been proposed, some with a similar function of stabilizing the Li<sup>59,74</sup> and some with redox mediator function on the cathode side<sup>36,75</sup>.

Ultimately, with the quest on producing batteries as lightweight as possible, the amount of electrolyte per mass of active material is important<sup>76</sup> and a subject of a multitude of research groups with reports as low as 3 μL per mg of sulfur<sup>77</sup>.

### *c) Separator*

Glassy fiber or polyolefinic separators (Celgard®) are commonly used in Li–S batteries, although improvements can be made through functionalizing the separator<sup>78</sup> or adding additional interlayers, which help stop polysulfide diffusion and protect the anode<sup>79</sup>.

#### 1.5.4 Li–S battery impedance

One of the basic battery properties of battery cells is their internal impedance, which influences the voltage and the capacity of the battery cell during use. Through these parameters, the power and energy attained are also dependent upon it. The technique of electrochemical impedance spectroscopy (EIS) is usually employed for the research of the internal impedance in batteries.

In the Li–S batteries this technique has already been used to measure the internal impedance of Li–S cells during the first discharge and charge, with speculations on the origin of different contributions.<sup>80</sup> A similar study has also been conducted by using dynamic impedance measurements, where the cell is not left to relax to OCV before impedance spectra is measured, rather an alternating signal is superimposed upon the direct current used for charging or discharging the battery.<sup>81</sup>

EIS has also been employed to examine the limiting factor during battery discharge, which was attributed to electrode passivation due to formation of solid reaction products.<sup>82</sup> A similar cause has been speculated to influence the size of charge transfer resistance and capacity fade<sup>83,84</sup>, while a different report was able to distinguish between anode and cathode capacity fade contributions<sup>85</sup>. A report of simulations of Li-S battery impedance response has also been published<sup>86</sup>, while EIS is also a technique which is commonly used to evaluate the reason behind a superior performance of new electrode materials.<sup>87,88</sup>

In general, the impedance response is depended upon the electrolyte and contact resistances (internal resistance) and the impedances of both the electrodes, where the contributions are from charge-transfer reactions and diffusion of redox active species. These contributions are usually complicated by the solid electrolyte interphase (SEI) formation on the Li metal surface<sup>89</sup>, and a layer of sulfur or Li<sub>2</sub>S, which forms on the cathode surface at different states of charge<sup>82,84,86</sup>. These complex mechanisms are further obscured by the fact that they occur on the surface of either very rough (lithium) or highly porous (carbon) electrode. When nearing the end of discharge, at least one of the contributions listed increases the overpotential of the cell until the voltage cut-off is reached and the discharge ends (for Li-S cells usually far from theoretical capacity value).

## 2 Aim and hypotheses of the thesis

The aim of this doctoral dissertation was to examine the Li–S battery on the basis of its internal impedance and to determine its influence on the electrochemical behavior. We focused on the cathode processes, the electrolyte impact and the interaction of the two components.

With it, we aim to understand how the physicochemical properties of the electrolytes influence the internal resistance and the cycling behavior of the batteries. The knowledge could then be used to design a better electrolyte composition. Furthermore, the impedance response of the electrodes will be examined and the processes which most significantly contribute to it studied and elucidated.

This dissertation first focuses on explaining the basics of battery components and characteristics (Section 1.1) and a brief summary of primary and secondary battery technology is made (1.2). The electrochemical and other analytical techniques, which are used for the determination of battery characteristics (1.3) are presented and explained (1.4). Since lithium–sulfur (Li–S) batteries were the main focus of the work, state of the art on that topic is summarised, and the problems that the system faces elucidated (Section 1.5).

A list of materials among with specifications for various electrochemical and analytical methods used is stated in Section 3.

The resistive intercept and the electrolyte's influences on it were studied by varying the electrolyte's physicochemical properties (Section 4.1). Using the symmetrical cells approach, the contributions were divided between both electrodes and further elucidated (Section 4.2). More attention was given to the cathode response, where glassy carbon electrodes were used to investigate the polysulfide electrochemistry (Section 4.4). The knowledge gathered was then used to elucidate the origins of contributions to internal resistance in conventional porous electrode Li–S cells (Section 4.4.2). Since the final insoluble discharge product,  $\text{Li}_2\text{S}$ , was found to have a profound impact on the battery impedance response, its crystallisation mechanism and morphology was investigated (Section 4.4.3).

At the end of the thesis, conclusions, literature information, a list of tables and figures as well as a summary in Slovene language is given (Section 6).

**Hypotheses of the thesis are as follows:**

Internal resistance of a lithium–sulfur battery cell could be characterized with the use of impedance spectroscopy.

In a lot of systems the internal resistance of a battery cell can be studied through measuring the impedance spectra of the system in the relaxed state. If the potential of the plateau is stable enough, the measurement can also be done dynamically (with current passing through the system). Li–S redox system is complex due to the solubility of polysulfides and its shuttle effect phenomenon, which means that the system is constantly changing. This results in special challenges when conducting such experiments. We propose that we can design a proper experiment allowing us to study the contributions to the internal resistance of the lithium–sulfur system.

Physicochemical properties of the electrolyte (viscosity, density, conductivity, solubility of polysulfide species) influence the performance of lithium–sulfur batteries.

Highest frequency contribution in the impedance spectra corresponds to the resistance of the electrolyte, which is of course connected with its conductivity. Due to the solubility of polysulfides this resistance changes during cycling of the battery.<sup>90</sup> We assume that other electrolytes' physicochemical properties also influence the performance of lithium–sulfur batteries. Viscosity of the electrolyte will probably influence the diffusion of electroactive species to and from the electrode surface. Salt concentration will likely influence polysulfide solubility. Same we can claim for different solvents, where polysulfides have different solubility. All those parameters have an influence on the internal resistance.

Metallic lithium anodes' contribution to the internal resistance will be negligible due to dendritic growth and surface area increase.

Dendritic growth of Li is a relatively known phenomenon.<sup>56,91–93</sup> We suspect that the anode contribution will decrease with cycling of the battery cell and become negligible.

Porous cathode build out of carbon-sulfur composite has the most significant contribution to the internal resistance of the lithium–sulfur battery cell. A contributing factor is, among others, the deposition of an insulating layer of  $\text{Li}_2\text{S}$  across its surface.

Last stage of discharge is the formation of lithium sulfide, which is poorly soluble in used electrolytes and insulating in nature. It deposits on the electrode surface and by that closes its pores, reduces surface available for electrochemical reactions and increases the cathodes' contribution to the internal resistance.

### 3 Materials and methods

#### 3.1 A list of used materials

- ENSACO 350G carbon, Imerys, 777 m<sup>2</sup> g<sup>-1</sup> surface area, total pore volume 0.98 cm<sup>3</sup> g<sup>-1</sup>, average pore size 6 nm
- Printex XE2 conductivity additive, Degussa, 950 m<sup>2</sup> g<sup>-1</sup> surface area
- *N*-methylpyrrolidone (NMP), Merck, 872-50-4
- Polyvinylidene fluoride (PVDF), Aldrich, 24937-79-9
- Polytetrafluoroethylene (PTFE), 60 wt.% dispersion in water, Aldrich, 9002-84-0
- Li foil, ribbon 110 μm thick, FMC
- 1,3-dioxolane (DOL), anhydrous, Aldrich, 646-06-0
- Tetraethylene glycol dimethyl ether (TEGDME), Aldrich, 143-24-8
- Lithium bis(trifluoromethylsulfonyl) imide (LiTFSI), 99.95%, Aldrich, 9076-65-6
- Tetrahydrofuran (THF), Aldrich, 109-99-9
- Sulfur powder, 99.98%, Aldrich, 7704-34-9
- *N,N*-Diethyl-*N*-methyl-*N*-(2-methoxyethyl)ammonium bis(trifluoromethanesulfonyl)imide ([DEME][TFSI]), Solvionic, 99.9%, AmSF708A50
- 1,1-(1,1,2,2-tetrafluoroethoxy)ethane (TFEE), Apollo Scientific, PC450236
- Sulfolane, Aldrich, 126-33-0
- Triplex foil PET-Al-PE, Amba Co.
- Nickel foil, 99.9%, 0.0125 mm, Goodfellow
- Glassy fiber paper Whatman, GF/A (260 μm) and GF/D (670 μm)
- Celgard 2400 microporous membrane, thickness of 25 μm
- Glassy carbon SIGRADUR D discs (16 mm φ and 12 mm φ, thickness 0.5 mm), HTW
- Li permeable ceramic membrane LICGC Type AG01 Li<sub>1+x+y</sub>Al<sub>x</sub>Ti<sub>2-x</sub>Si<sub>y</sub>P<sub>3-y</sub>O<sub>12</sub>, 150 μm thick, OHARA
- Carbon coated Al foil, 25 μm thick
- Carbon coated Al mesh, app. 50 μm thick
- Freudenberg H14 carbon felt paper, 150 μm thick, app. 15 cm<sup>2</sup>/cm<sup>2</sup> surface area
- Freudenberg FS2225 non-woven polyolefin separator, 150 μm
- Lithium 4,5-dicyano-2-(trifluoromethyl)imidazole (LiTDI), Solvionic, 99.9%, S026A10

## 3.2 Battery components preparation and cell assembly

### 3.2.1 Cathode manufacturing and polysulfide synthesis

For cathode manufacturing, the sulfur/carbon composite was prepared by mixing sulfur and ENSACO 350G carbon in 2:1 weight ratio. The mixture was then heated to 155 °C for 5 hours under argon atmosphere. The C-S composite with 66 wt.% of sulfur was mixed with the conductivity additive (Printex XE2) and binder (PVDF) in 80:10:10 wt.% ratio in NMP solvent. The slurry obtained by ball milling was then casted on primed aluminum foil with Doctor Blade applicator and dried overnight at 50 °C (SP-55 EASY drier, Kambič). The finished electrodes had an active mass loading of approximately 1 mg of S per cm<sup>2</sup>.

For high-energy cell's cathodes, the composite was prepared in our lab and sent to Fraunhofer ISIT for cathode manufacturing. There it was mixed with Printex XE2 and PVDF in the same weight ratio, casted on Al foil and dried. The active mass loading on the electrodes was approximately 4 mg of S per cm<sup>2</sup>.

Cathodes intended for cells used in *operando* XAS measurements were prepared differently due to sulfur self-absorption effects<sup>13</sup>. The cathodes were made out of a composite with 25 wt.% of sulfur. It was mixed with PTFE and Printex XE2 in anhydrous isopropanol in the same mass ratio as for the standard cathodes. These Teflon electrodes were pressed on carbon coated aluminum mesh and had an active mass loading of app. 0.5 mg of S per cm<sup>2</sup>.

When active mass was added as a catholyte solution, polysulfides of desired chain length were previously synthesised. The synthesis was done by dissolving stoichiometric amounts of lithium foil and sulfur powder in THF inside the glovebox (LABmaster, MBRAUN). The mixture was then mixed at elevated temperatures (50–70 °C) until all the powder and metal dissolved. The polysulfides were isolated under reduced pressure inside the glovebox with tubing connected to an outside rotary evaporator. Polysulfide solutions of desired nominal concentrations were prepared by dissolving the calculated amount of polysulfide in powder form in the chosen electrolyte. When catholyte was the means of active mass addition, the solution was added to the positive electrode manufactured without the addition of sulfur. In that case, ENSACO 350G carbon was mixed with pVdF in 9:1 mass ratio and casted as a suspension in NMP on Al foil in various thicknesses. These electrodes were dried similarly as the ones with added sulfur.

### 3.2.2 Preparation of electrolyte solutions

Electrolyte solutions were prepared out of previously dried solvents and salts inside the glovebox. The Li<sup>+</sup> salt was weighed inside a volumetric flask, dissolved and filled to the markings with the prepared mixture of solvents. When testing the [DEME][TFSI] (N,N-Diethyl-

N-methyl-N-(2-methoxyethyl)ammonium bis(trifluoromethanesulfonyl)imide ionic liquid) and 1,3-dioxolane (DOL) electrolyte system, the solutions were prepared by mass.

### 3.2.3 Cell assembly

Pouch cells were assembled inside the glovebox by adding a stated amount of electrolyte with a Handystep® electronic pipette (BRAND) and 100 µL PD-Tips onto the cathode and separator. All the separators used were previously dried in a vacuum dryer at elevated temperatures (VS-25 DC, Kambič). The amount of electrolyte added depended upon the type of separator used. Experiments were made with Celgard 2400 separator, two different glassy fibre separators (Whatman GF/A and GF/D), Freudenberg FS2225 non-woven polyolefin separators or OHARA ceramic membrane. Li foil was used as received from FMC Lithium corporation. The pouch cell was vacuum sealed.

For *operando* measurements, modified Swagelok or pouch cells were used:

- For UV-vis experiments, coffee bags were constructed with a 170 µm quartz window. A hole was made in the Li anode before assembly. Thicker separator was used in order to minimize light absorption in the cathode. Due to that, higher electrolyte loadings were also used.<sup>94,95</sup>
- For XAS experiment, a special Swagelok cell with 13 µm thick Be window and cathodes with lower sulfur loading as described in Section 3.2.1 were used.<sup>10,13,96</sup>

For glassy carbon cells a carbon disc instead of the porous electrode was added and a catholyte solution of polysulfides replaced the electrolyte.

## 3.3 Electrochemical measurements

Cells were tested with different electrochemical measurements. Most common for battery performance evaluation were galvanostatic experiments. For impedance response determination, cells were tested with impedance spectroscopy. Our battery cells were tested on VMP3, MPG2 or SP200 potentiostat/galvanostat instruments from Bio-logic. The data was processed in EC-Lab V11.10 and Origin 8.1 software. When temperature stabilisation was needed, the cells were placed inside a LAUDA E200 thermostat filled with silicone insulator oil Kryo 51.

### 3.3.1 Galvanostatic experiments

As described in Section 1.4, galvanostatic experiments on batteries are the most common and supply a voltage-capacity characteristic, from which capacity, overpotential and Coulombic efficiency could be determined.

Battery cycling was conducted with a chosen C-rate in the range of 1.5 to 3.0 V vs. Li/Li<sup>+</sup>. With some experiments, C-rate capability test was performed to determine how the cell handles different currents. The program was as follows: C/20–C/10–C/5–C/2–1C (5 cycles each) – C/10 (75 cycles) in the same potential range of 1.5–3.0 V vs. Li/Li<sup>+</sup>.

Galvanostatic intermittent titration technique (GITT) was used to determine the open circuit voltage of the cell (OCV) at various depths of discharge (DOD). A battery was first discharged or charged for a chosen amount of time, until the current was stopped and the potential relaxation followed until  $dE/dt$  was less than 15 mV h<sup>-1</sup>. The experiment was then repeated until the potential reached the cut off voltage.

The program for lithium stripping and deposition tests was as follows: first cycle of stripping and deposition was done to 2 mAh cm<sup>-2</sup> with a current of 0.5 mA cm<sup>-2</sup>. The consecutive 50 cycles were with the same current until 1 mAh cm<sup>-2</sup> capacity was achieved. In the last cycle, first cycle settings were repeated. Unless stated otherwise, the size of electrodes was 2 cm<sup>2</sup> in all tested cells.

### 3.3.2 Impedance spectroscopy

With impedance spectroscopy, the excitation signal consists out of a small amplitude alternating voltage of different frequencies ( $\omega=2\pi\nu$ ). The impedance response of the system is a quotient between the voltage and current response and is defined as Equation 9 ( $U_0$  and  $I_0$  are voltage and current amplitudes,  $\phi$  is the phase shift).<sup>97</sup>

$$Z(\omega) = \frac{U(\omega)}{I(\omega)} = \frac{U_0}{I_0} e^{-i\phi} = \frac{U_0}{I_0} [\cos(\phi) - i \cdot \sin(\phi)] \quad (9)$$

As a result an impedance spectrum is obtained, where imaginary part of impedance is usually plotted as a function of the real part and each point corresponds to one frequency of the alternating signal (Nyquist plot, Figure 9).

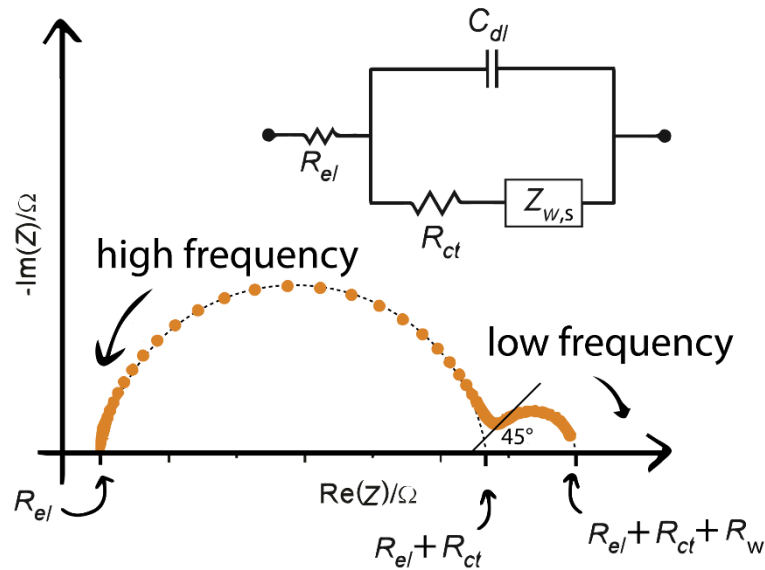


Figure 9: An example of a simple impedance spectrum in Nyquist plot representation with its equivalent circuit model.

The spectra include information about resistive and capacitive contributions. Depending on the frequency and the shape, one could (in theory) distinguish between the resistance of the electrolyte (Figure 9,  $R_{el}$ ), the charge transfer reaction (Figure 9,  $R_{CT}$  and  $C_{dl}$ ) and diffusion contributions (Figure 9,  $Z_w$ ). In practice however, spectra explanation is usually complicated due to the contributions overlapping. The shape of the spectra can be fitted with an equivalent electrical circuit model, which consists out of a series of resistors and capacitors.<sup>98,99</sup>

#### a) General impedance response of a simple redox system with two symmetrical electrodes

In a redox system where an oxidized (Ox) and reduced (Red) species are present in the electrolyte between two symmetrical electrodes, two main processes are taking place during impedance spectroscopy measurement. The species react following a redox reaction (Equation 10) and they diffuse to and from the electrodes (the migration of the redox active species is neglected due to the supporting electrolyte used).<sup>97</sup> This type of scenario gives a Randles-like equivalent circuit, where the response depends upon the electrolyte resistance ( $R_{el}$ ), a charge transfer resistance ( $R_{ct}$ ), Warburg impedance for diffusion contribution ( $Z_w$ ) and double layer capacitance ( $C_{dl}$ ) (Figure 9). If one wishes to explicitly show that the cell is constructed out of two identical electrodes, it should be noted that in the Randles circuit in Figure 9 the  $R_{ct}$ ,  $Z_w$  and  $C_{dl}$  elements are all a result of two identical contributions from each of the electrodes in series ( $R_{ct} = 2R_{ct}'$ ,  $Z_w = 2Z_w'$  and  $C_{dl} = C_{dl}'/2$ ).



Even if just a single electrode is considered, there are in principle two Warburg diffusion features present, one for each of the present species. In practice, however, the Warburg resistances for the two species can be significantly different and one of the features would prevail over the smaller one, or, both can be very similar and merge into one (Figure 9, one Warburg feature present at low frequencies).

Experiments conducted on our cells were done on three different bases – potentiostatic electrochemical impedance spectroscopy (PEIS), galvanostatic electrochemical impedance spectroscopy (GEIS) and alternating current voltammetry (ACV). The first one is an experiment, where a constant voltage is set and an alternating voltage potential is superimposed. Measurements were done with 10.0 mV (rms) voltage amplitude starting with the highest frequency the instruments achieved (1 MHz or 20 kHz). Low frequency limit was varied from 10 mHz down to 20  $\mu$ Hz. When PEIS measurements were done during battery cycling, the current was first stopped and the cell left to relax before the impedance spectrum was measured.

For GEIS dynamic measurements, a set current is applied to the cell and that value superimposed with an alternating current signal. Experiments with GEIS were done through the first discharge of the battery cell. The current amplitude was chosen to be 10-times smaller than the current used for cycling and the frequency range such that a satisfying number of spectra were recorded until the battery potential reached the cut off voltage.

ACV measurements are conducted by applying a small amplitude AC potential with a set frequency and amplitude during a potential sweep. As a result, the change in current is measured. The plot is usually given as the amplitude of the AC current signal being a function of the DC component of the potential.

Impedance spectra were further processed and fitted using ZView version 3.4f.

### 3.4 Other analyses

Electrochemical tests were sometimes coupled with other analytical techniques to elucidate the mechanisms of operation or determine the properties of the materials.

#### 3.4.1 Determination of electrolyte physicochemical properties

Physicochemical properties of different mixtures of ionic liquid [DEME][TFSI] and 1,3-dioxolane with LiTFSI salt were determined through analysis of conductivity, viscosity and

density. The extent of polysulfide dissolution into the electrolyte was also evaluated by help of impedance spectroscopy as described in the results and discussion section.

Density of the electrolyte solutions was measured with Anton Paar DMA 500 vibration type density meter in the temperature range of 273.15–333.15 K with 5 K interval.

For electrolyte viscosity determination, micro Ubbelohde viscometers from SI Analytics GmbH (536 10 capillary I, 536 20 capillary II and 536 30 capillary III) and ViscoSystem\_AVIS 370 were employed. They were determined in multiple parallels at each chosen temperature. Kinematic viscosity was later calculated as a product of the viscometer constant and average flow time. By multiplying this value with the determined density, dynamic viscosity was attained.

Conductivity of the electrolytes was measured with capillary cells<sup>100</sup> with different cell constants ( $\sim 3 < B'/\text{cm}^{-1} < \sim 85$ ). Nine cells in a custom-made housing were used and calibrated with dilute potassium chloride solutions.<sup>101</sup> The cells were connected to LCR Meter Agilent 4284 A, which enables conductivity measurements at multiple frequencies. Frequencies chosen were in 500 Hz interval from 500 Hz to 10 kHz. The end value for electrolyte conductivity was determined by extrapolation to infinite frequencies. Oil bath temperature was maintained with calibrated Pt-100 resistance thermometer (MPMI 1004/300 Merz) connected to HP 3458 A multimeter. A custom-developed software was used for data acquisition and temperature control.<sup>102</sup> Electrolyte solutions were transferred to the cells in inert atmosphere.

### 3.4.2 UV-vis spectroscopy

The pouch cell manufacture and assembly was done the same as described in published works.<sup>94,95</sup> The cells were placed in a UV-vis spectrometer Perkin-Elmer Lambda 950. Cells were galvanostatically cycled using an SP200 potentiostat or in some cases left at OCV with impedance spectroscopy measurements. During that, the UV-vis spectra were recorded *operando* from 800 nm to 250 nm.

### 3.4.3 IR spectroscopy

For some electrolyte mixtures, ATR-IR measurements were performed on a Bruker Vertex 80 instrument equipped with liquid nitrogen cooled mercury cadmium telluride (MCT) detector and a Specac Silver gate ATR with a Ge crystal. The spectra were measured in absorbance mode with 256 scans at a resolution of  $2 \text{ cm}^{-1}$  in the range of  $4000\text{--}500 \text{ cm}^{-1}$ . Processing (automatic baseline correction and atmospheric compensation) of the spectra was performed in OPUS version 7.0 software.

#### 3.4.4 Scanning electron microscopy

For scanning electron microscopy (SEM) analysis of the materials, a field-emission scanning electron microscope (FE SEM) Supra 35VP from Zeiss, Germany was used. If the samples analysed were sensitive to the atmosphere, they were prepared inside the glovebox on a custom made holder, which was vacuumed inside the glovebox antechamber and opened when exposed to vacuum inside the SEM instrument. SEM micrographs were usually collected with the electron gun accelerating voltage of 1 kV, a low setting due to instability of the materials under the electron beam.

Samples subjected to FIB cross-sectional analysis were attached to Al-stubs by using carbon tape, transferred from the glovebox to the sputter coater PECS 682 (Precision Etching Coating System – model 682, Gatan, USA) in inert atmosphere and coated with 20 nm layer of Pt. After coating, samples were transferred back to the glovebox, vacuum sealed and transferred to the FIB instrument without exposing them to air atmosphere.

Focus Ion Beam – Scanning electron Microscope was used for cross-section analyses. FIB-SEM Helios Nanolab 650i (FEI, USA) is equipped with energy dispersive spectrometer X-MAX 50 (Oxford, UK) and Pt gas injection system. Since the sample was highly sensitive to the ion beam, surface was protected with 200 nm “Insitu” deposited platinum. Additional Pt was deposited on top of the initial layer by using Ga<sup>+</sup> ion beam (30 kV @ 0.23 nA). The final thickness of the Pt surface protective layer was 800 nm. Cross-sections were done by focused Ga<sup>+</sup> ions at 30 kV @ 9.4 nA with reducing currents to 0.23 nA for final ion polishing. Images of the surface and cross-sections were captured using low electron energy (2 kV @ 50 pA) beam and ETD detector. Phase contrast images and detailed information were acquired using pre-monochromated electron beam (1 kV) and 25 pA beam current and InColumn integrated SE/BSE detectors.

### 3.4.5 X-ray absorption spectroscopy

*Operando* sulfur K-edge XANES measurements were done at the XAFS beamline of Elettra synchrotron in Basovizza, Trieste in fluorescence-detection mode<sup>96</sup>. A Si (111) double crystal monochromator with 0.3 eV resolution at 2.5 keV was used. Higher-order harmonics were eliminated by placing a double-flat silica mirror at a grazing angle of 8 mrad. The intensity of the monochromatic X-ray beam was measured by a 30 cm-long ionization chamber detector, which was filled with a mixture of 1970 mbar of He and 30 mbar of N<sub>2</sub>. The signal in fluorescence mode was detected with a KETEK GmbH AXAS-M silicon drift detector with an area of 80 mm<sup>2</sup>. The battery prepared in a Swagelok cell was mounted on the sample holder and placed in a chamber after the first ionization detector.<sup>10,13</sup> The chamber was filled with 10% atmospheric overpressure of He.

To diminish self-absorption effects, Sulfur K-edge XANES measurements done in fluorescence detection mode require low ratio of sulfur in the cathode composite.<sup>13</sup> The absorption spectra were measured relative to the S K-edge (2472 eV) within the interval of –150 to +300 eV. In the XANES region (up to 2490 eV), energy steps of 0.2 eV were used. For higher energies we adopted equidistant k steps of 0.03 Å<sup>-1</sup>, with an integration time of 5 s. The energy calibration was established with an absorption measurement of native sulfur in transmission-detection mode. The maximum for the edge peak was set to 2472.0 eV.<sup>10,13</sup> The absolute energy reproducibility was ±0.05 eV or better for the measured spectra.

The XAS spectra were collected in a series of consequent scans (52 minutes of measuring time) during discharge of the battery. The analysis of the spectra was performed with Demeter program package ATHENA<sup>103</sup>. Sulfur K-edge XANES fluorescence spectra were normalized to a unit K-edge jump and corrected for dead time.<sup>10,13</sup>

## 4 Results and discussion

For Li–S battery internal impedance response evaluation, three batteries with different electrolytes were prepared and tested. The electrolytes were 1 M LiTFSI salt solutions in [DEME][TFSI]:DOL 1:2, sulfolane:DOL 1:1 and TEGDME (tetraethylene glycol dimethyl ether):DOL 2:1 mixture. The ratios were chosen so that the viscosities of the final electrolyte solutions were similar and close to 5 mPa·s. The battery cells were constructed with an excess of electrolyte (60  $\mu\text{L}$  per mg S) in order to remain free of the phenomena that leads to battery failure due to cells drying up. To accommodate the excess of electrolyte, thick glassy fibre separator (GF/D) was used. The reason why the separator and the electrolyte amount were chosen was also poor wettability shown when using sulfolane based electrolytes with Celgard separators. Cathodes (1.5  $\text{cm}^2$ ) used were constructed in the laboratory according to the procedure described in the experimental section and had an active mass loading of approximately 1  $\text{mg}_\text{S}/\text{cm}^2$ .

First, impedance spectra were recorded on fresh cells from 1 MHz to 10 mHz with an amplitude of 10.0 mV (rms). The batteries were then discharged at C/20 for a period of 1 hour (Figure 10, green) before stopping the current and leaving them at OCV for 15 minutes (Figure 10, red). Impedance spectrum was recorded with the same settings as were used on fresh cells (Figure 10, blue) before C/20 current was applied again. After the voltage of 1.5 V was reached, the current was reversed and the same measurement done through charge. Voltage cut-off for charge was 3.0 V vs. Li/Li<sup>+</sup>.

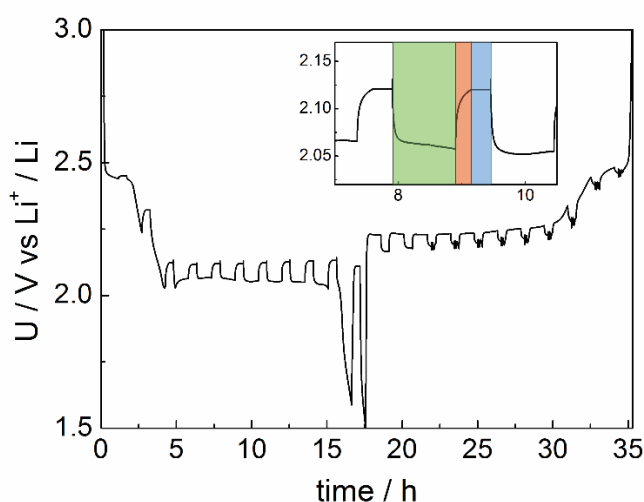


Figure 10: Voltage curve during one cycle of impedance spectra measurement at different DOD. Insert shows three parts of the program during discharge – green is the galvanostatic period, red relaxation time and blue PEIS measurement.

50 cycles of galvanostatic cycling with intermittent impedance measurements were done. The capacities and efficiencies the batteries reached are shown on Figure 11. If we compare the three tested electrolytes, we can conclude that in terms of capacity reached and its fade, sulfolane and TEGDME based electrolyte work very similar, with the latter having better efficiencies. The ionic liquid electrolyte has poor capacity, but the best Coulombic efficiency.

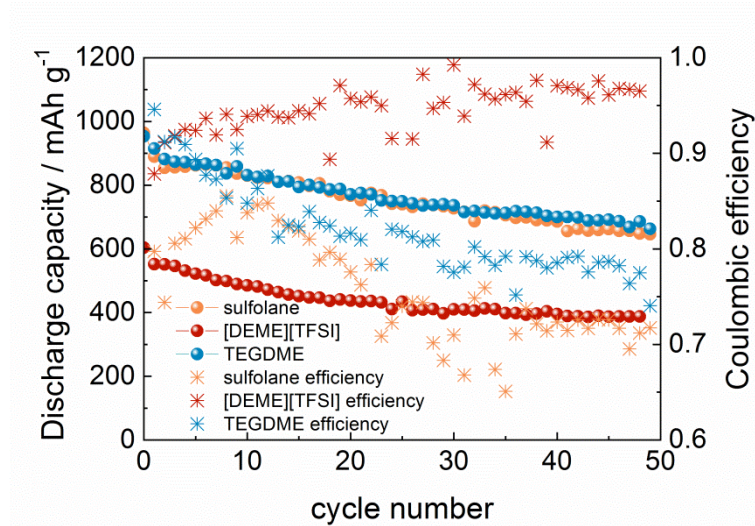


Figure 11: Specific discharge capacities and Coulombic efficiencies through 50 cycles of the experiment with intermittent impedance spectra measurements.

The spectra measured were then extracted and fitted in ZView with a simple equivalent circuit model (Figure 12). The evolution of the four contributions was followed through different depths of discharge and multiple cycles of battery use. The sum of all resistances was usually around 1-2 k $\Omega$ , which corresponds well with the internal impedance calculated from galvanostatic experiments.

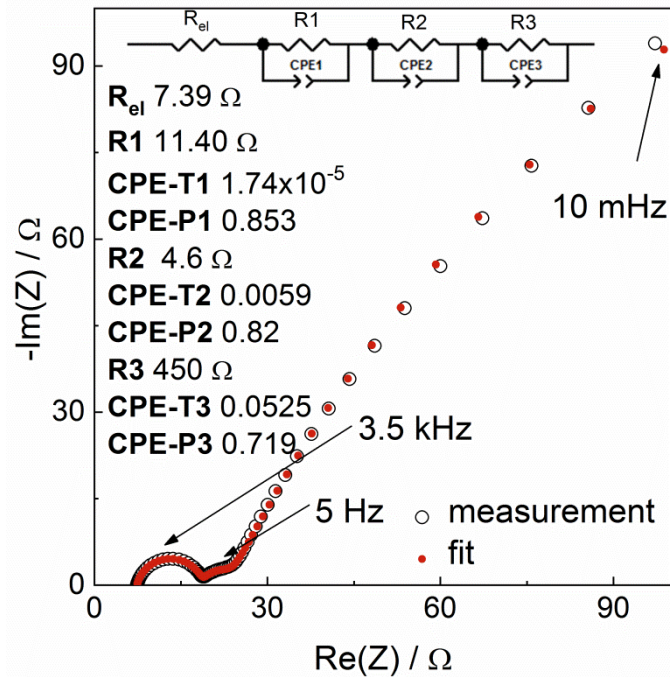


Figure 12: A typical impedance spectrum of a Li-S battery cell (sulfolane based electrolyte) in the first cycle at app. 50% DOD (white circles). Fit (red circles) with the equivalent circuit model shown.

Reprinted with permission from reference <sup>104</sup>. Copyright 2017 American Chemical Society.

The R1 contribution (Figure 12) was the only one we could unequivocally attribute to the electrolyte (and contact resistance). The origin and significance of the other three semicircle contributions were later investigated with symmetrical anode-anode and cathode-cathode cells. We do not claim for this equivalent circuit model to be physically explainable and directly linked to an electrolyte resistance ( $R_{el}$ ) and three different processes taking place inside the cell (RC1-RC3). We used it since it was the simplest one that fit well with the measurements and could enable us to follow the change each contribution goes through with battery aging.

#### 4.1 High frequency resistive intercept contribution (electrolyte investigation)

The resistive intercept ( $R_{el}$  in Figure 12) is, as explained, a sum of the electrolyte and contact resistances. Since the cell setup is optimised, we have little effect on the latter. Li–S batteries exhibit a distinctive curve in their electrolyte resistance response through discharge and charge of the cell.<sup>12,90</sup> The same shape can be seen in the three electrolytes tested (Figure 13). The initial resistive intercept increases through the high-voltage plateau and reaches a maximum just before the precipitation of  $\text{Li}_2\text{S}$  starts in the bottom voltage plateau. In charge, a similar (reverse) thing happens, although the resistance never decreases back down to its starting value.

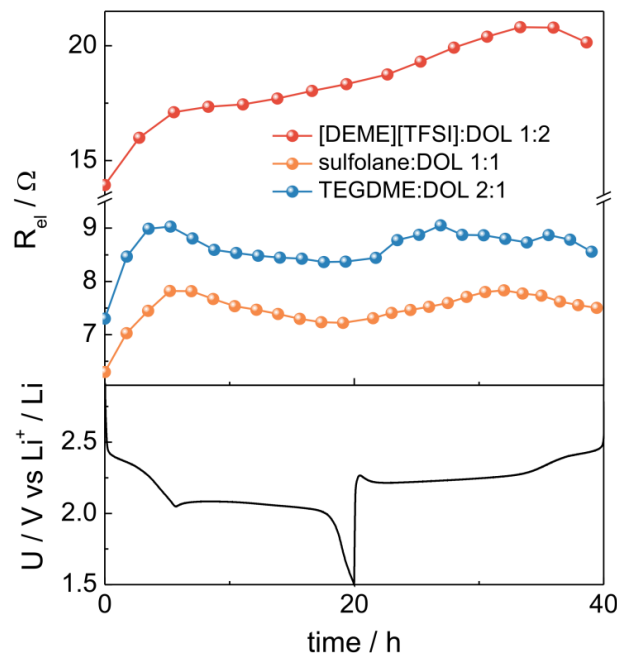
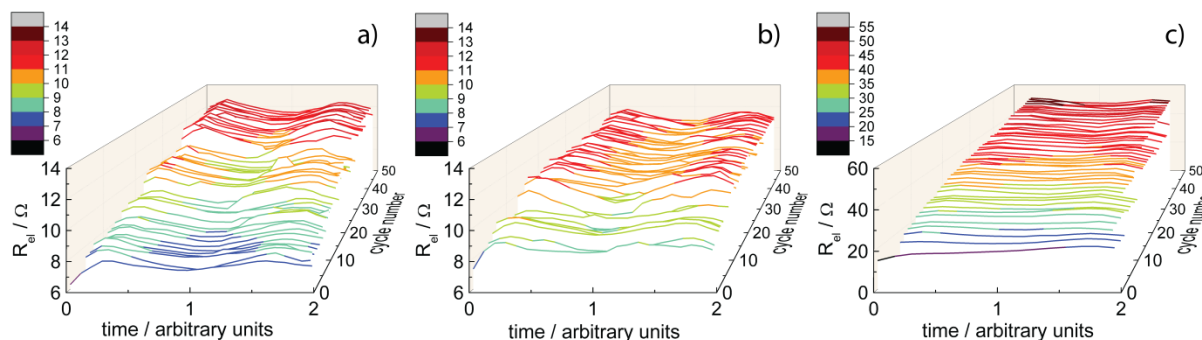


Figure 13: Resistive intercept change through the first cycle for the three electrolytes tested.

The reason behind this curve is in polysulfide dissolution into the electrolyte, which makes it more viscous and disables the ion transport. After the amount of dissolved polysulfides decreases due to  $\text{Li}_2\text{S}$  precipitation, the resistance also decreases. Since the initial value is never reached, it is implied that some polysulfides that dissolve into the electrolyte never precipitate.

This change was monitored through the 50 cycles of the experiment. On Figure 14 you can see the results for all three electrolytes. X-axis is for time, but the discharge and charge duration was both normalized. This means that with further cycling, although less capacity was reached, the data for discharge is always plotted between 0 and 1 and data for charge between 1 and 2. Y-axis and its scale for resistance is the same in the cases of sulfolane and

TEGDME based electrolytes, and stretched to larger values for the ionic liquid. Blue colour significates low resistances and red higher resistances. Cycle number increases with going further into Z-axis.



**Figure 14:** Resistive intercept change through 50 cycles at different DOD for three different electrolytes – a) 1 M LiTFSI in sulfolane:DOL 1:1, b) 1 M LiTFSI in TEGDME:DOL 2:1 and c) 1 M LiTFSI in [DEME][TFSI]:DOL 1:2.

Results for sulfolane and TEGDME based electrolytes are again very similar (Figure 14a and b). The characteristic shape described in Figure 13 is seen through the cycles. The values first increase and level out from the starting 8  $\Omega$  to approximately 12  $\Omega$ . Sulfolane shows greater increase in values. For [DEME][TFSI] the sharp increase seen in the first cycle (Figure 13) continues with resistances reaching just above 50  $\Omega$  by the end of the experiment (Figure 14c).

#### 4.1.1 Influence of the electrolyte's physicochemical properties on battery performance

##### *a) Determination of physicochemical properties of [DEME][TFSI]:DOL electrolyte system*

To enable better understanding of the electrolyte and its physicochemical properties influence on the battery performance, the [DEME][TFSI]:DOL electrolyte system was chosen for further study. Different physicochemical properties (conductivity, viscosity, density, solubility of polysulfides) of the electrolyte mixtures were evaluated and later their trends compared to battery performances (specific capacity reached, capacity fade, Coulombic efficiency, overpotential and internal resistance).<sup>105</sup>

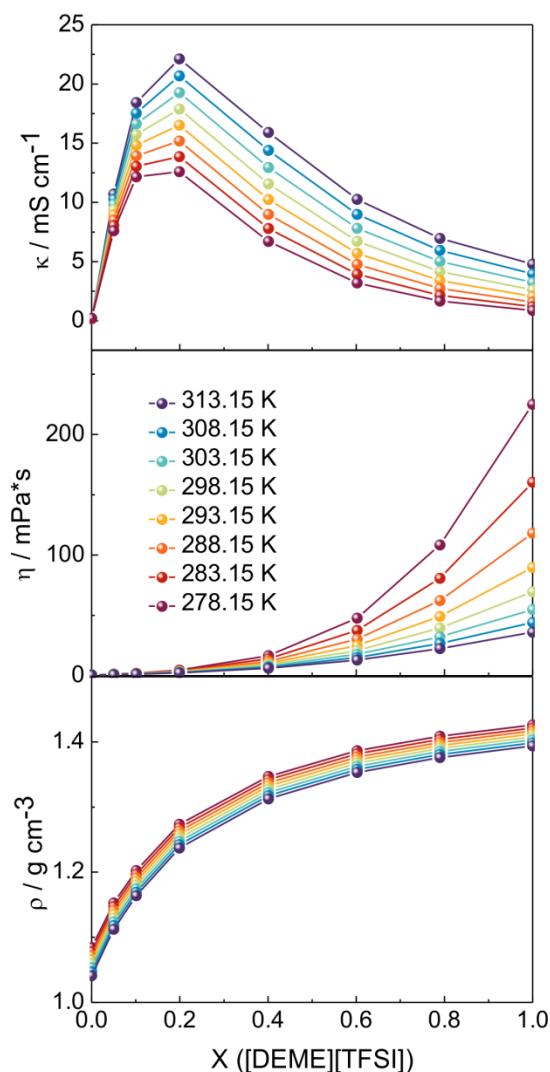


Figure 15: Physicochemical properties of [DEME][TFSI]:DOL mixtures without LiTFSI salt at different molar ratios and temperatures a) conductivity, b) dynamic viscosity, c) density.

First, the physicochemical properties of the binary mixtures without the added salt were measured. To do this, eight different molar mixtures of [DEME][TFSI] and DOL were prepared. As evident from Figure 15a, conductivity of binary mixtures without the added salt initially increases with increasing the molar ratio of the ionic liquid content. This happens due to the addition of more charge carriers. Afterwards, the values decline due to higher viscosity. Higher temperatures equal higher conductivities, with the peak conductivity remaining at the same composition, which is around  $X_{[\text{DEME}][\text{TFSI}]} = 0.2$ .

Viscosity increases from 0.5 mPa·s to over 200 mPa·s and is a function of both the temperature and ionic liquid content. With high contents of [DEME][TFSI], a 5 K temperature increase causes a greater increase in viscosity, than it did at lower molar ratios (Figure 15b).

Density's increment is steeper at low ionic liquid contents and levels out at low dioxolane content. Heating the mixtures changes the density for roughly the same amount at all the molar ratios tested (Figure 15c). Data from these measurements is shown in Table 1 - Table 3.

**Table 1: Densities of [DEME][TFSI] and dioxolane at various molar ratios at temperatures between 278.15 K and 313.15 K.**

X([DEME][TFSI])	$\rho$ (g cm <sup>-3</sup> )							
T [K]	278.15	283.15	288.15	293.15	298.15	303.15	308.15	313.15
0.000	1.084	1.078	1.072	1.066	1.060	1.053	1.047	1.041
0.050	1.153	1.147	1.141	1.136	1.130	1.124	1.118	1.112
0.101	1.202	1.197	1.191	1.186	1.180	1.175	1.169	1.164
0.199	1.273	1.268	1.263	1.258	1.253	1.247	1.242	1.237
0.401	1.347	1.342	1.337	1.332	1.327	1.322	1.317	1.312
0.602	1.387	1.382	1.377	1.372	1.367	1.363	1.358	1.353
0.790	1.409	1.404	1.399	1.395	1.390	1.385	1.381	1.376
1.000	1.426	1.421	1.417	1.412	1.408	1.403	1.398	1.394

**Table 2: Dynamic viscosities of [DEME][TFSI] and dioxolane at various molar ratios at temperatures between 278.15 K and 313.15 K.**

X([DEME][TFSI])	$\eta$ (mPa·s)							
T [K]	278.15	283.15	288.15	293.15	298.15	303.15	308.15	313.15
0.000	0.75	0.71	0.66	0.63	0.59	0.56	0.53	0.51
0.050	1.31	1.22	1.14	1.07	0.99	0.94	0.88	0.83
0.101	2.06	1.91	1.78	1.67	1.56	1.45	1.37	1.30
0.199	4.63	4.09	3.69	3.34	3.09	2.84	2.59	2.41
0.401	16.60	13.95	11.87	10.24	8.94	7.87	6.97	6.21
0.602	47.74	37.54	30.32	24.96	20.81	17.62	15.01	13.03
0.790	108.37	80.70	62.22	49.07	39.47	32.18	26.67	22.44
1.000	225.00	160.34	118.23	89.70	69.59	54.88	44.09	36.04

**Table 3: Conductivities of [DEME][TFSI] and dioxolane at various molar ratios at temperatures between 278.15 K and 313.15 K.**

X([DEME][TFSI])	$\kappa$ (mS cm <sup>-1</sup> )							
T [K]	278.15	283.15	288.15	293.15	298.15	303.15	308.15	313.15
0.000	0.21	0.19	0.18	0.18	0.18	0.17	0.17	0.17
0.050	7.61	8.06	8.51	8.95	9.40	9.84	10.28	10.72
0.101	12.16	13.04	13.93	14.83	15.73	16.63	17.53	18.43
0.199	12.60	13.87	15.18	16.51	17.88	19.27	20.68	22.12
0.401	6.71	7.81	8.99	10.24	11.56	12.95	14.39	15.90
0.602	3.19	3.93	4.77	5.70	6.71	7.81	8.99	10.26
0.790	1.66	2.15	2.74	3.40	4.16	5.01	5.94	6.97
1.000	0.87	1.19	1.59	2.06	2.61	3.25	3.97	4.78

***b) Determination of physicochemical properties of LiTFSI:[DEME][TFSI]:DOL electrolyte system***

Further tests were conducted on mixtures chosen around the maximum conductivity ( $X = 0.101, 0.199, 0.401$ ). Nine electrolytes were prepared with three different concentrations of LiTFSI salt (0.1 M, 0.5 M, 1.0 M). Its physicochemical properties were tested the same way as described for previous mixtures and are shown in Table 4 - Table 6. On Figure 16 only the values at room temperatures (298.15 K) are shown for clarity. Values for electrolytes without LiTFSI addition are also depicted for comparison.

At different salt concentrations, the conductivity change because of an increase in ionic liquid content shows a different trend (Figure 16a). This is coherent with the conductivity trend of the electrolyte without the supporting salt (Figure 15a). With low salt concentrations the conductivity maximum is still at the same molar ratio of  $X = 0.199$ . An increase in LiTFSI concentration produces a change similar to increasing the content of the ionic liquid – a decrease in the conductivity. Thus, the electrolytes with higher LiTFSI concentrations have the highest conductivities at highest ratios of dioxolane. It should also be noted, that conductivity values represented here are for both anion and cation migration.

Viscosity (Figure 16b) and density (Figure 16c) of the electrolyte solutions increase with higher ionic liquid contents and higher LiTFSI molarities. Comparing the change due to increasing the lithium salt concentration at the same molar content of the ionic liquid gives an increase in density, which is approximately the same at all the different ionic liquid contents that were tested. For viscosity, the difference in that same scenario increases with decreasing the dioxolane content.

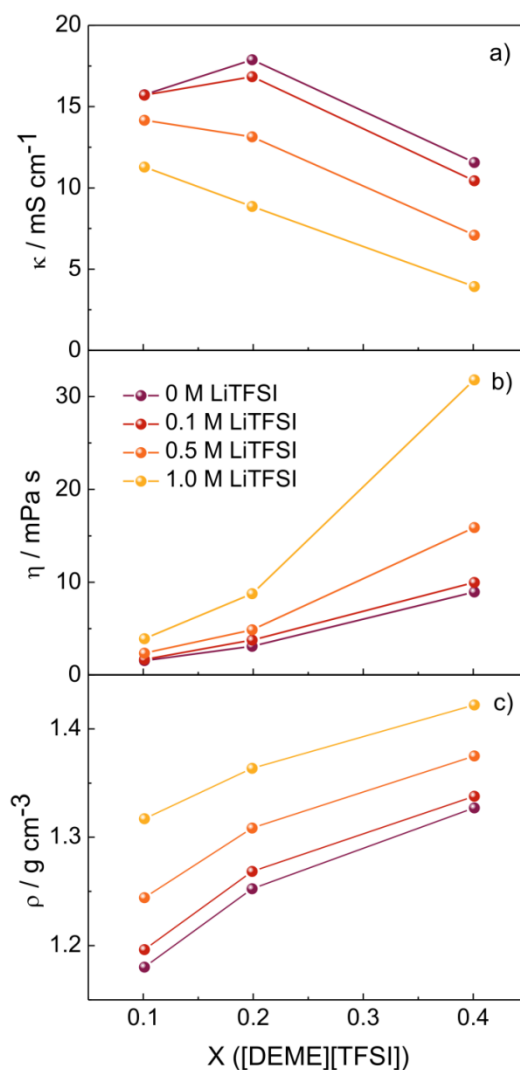


Figure 16: Physicochemical properties of [DEME][TFSI]:DOL:LiTFSI mixtures at 298.15 K a) conductivity, b) dynamic viscosity, c) density.

Table 4: Densities of [DEME][TFSI] and dioxolane at various molar ratios and different LiTFSI salt concentrations at temperatures between 278.15 K and 313.15.

c(LiTFSI)	X([DEME][TFSI])	$\rho$ (g cm <sup>-3</sup> )							
		278.15	283.15	288.15	293.15	298.15	303.15	308.15	313.15
0.1	0.101	1.219	1.213	1.207	1.202	1.196	1.191	1.185	1.180
0.5	0.101	1.267	1.261	1.255	1.250	1.244	1.239	1.233	1.227
1.0	0.101	1.328	1.322	1.317	1.311	1.305	1.300	1.294	1.288
0.1	0.199	1.289	1.284	1.279	1.274	1.268	1.263	1.258	1.253
0.5	0.199	1.330	1.324	1.319	1.314	1.309	1.303	1.298	1.293
1.0	0.199	1.385	1.380	1.374	1.369	1.364	1.358	1.353	1.347
0.1	0.401	1.358	1.353	1.348	1.343	1.338	1.333	1.328	1.323
0.5	0.401	1.395	1.390	1.385	1.380	1.375	1.370	1.365	1.360
1.0	0.401	1.443	1.438	1.432	1.427	1.422	1.417	1.412	1.407

**Table 5: Kinematic viscosities of [DEME][TFSI] and dioxolane at various molar ratios and different LiTFSI salt concentrations at temperatures between 278.15 K and 313.15.**

c(LiTFSI)	X([DEME][TFSI])	$\eta$ (mPa·s)							
		278.15	283.15	288.15	293.15	298.15	303.15	308.15	313.15
T [K]									
0.1	0.101	2.26	2.08	1.93	1.80	1.69	1.57	1.46	1.39
0.5	0.101	3.34	3.02	2.77	2.56	2.35	2.16	2.00	1.87
1.0	0.101	6.04	5.40	4.76	4.28	3.92	3.58	3.30	2.94
0.1	0.199	5.71	4.94	4.45	4.00	3.77	3.43	3.23	2.91
0.5	0.199	8.05	6.98	6.15	5.45	4.88	4.40	3.99	3.64
1.0	0.199	15.85	13.31	11.44	9.88	8.76	7.72	6.85	6.20
0.1	0.401	19.03	15.86	13.49	11.52	9.98	8.72	7.70	6.87
0.5	0.401	33.69	27.13	22.45	18.75	15.88	13.53	11.80	10.29
1.0	0.401	80.50	61.93	48.75	39.01	31.80	26.33	22.08	18.76

**Table 6: Conductivities of [DEME][TFSI] and dioxolane at various molar ratios and different LiTFSI salt concentrations at temperatures between 278.15 K and 313.15**

c(LiTFSI)	X([DEME][TFSI])	$\kappa$ (mS cm <sup>-1</sup> )							
		278.15	283.15	288.15	293.15	298.15	303.15	308.15	313.15
T [K]									
0.1	0.101	12.07	12.96	13.87	14.79	15.70	16.63	17.55	18.48
0.5	0.101	10.63	11.50	12.38	13.26	14.16	15.06	15.96	16.85
1.0	0.101	8.08	8.88	9.68	10.49	11.29	12.02	12.57	12.94
0.1	0.199	11.70	12.93	14.21	15.51	16.84	18.20	19.58	20.98
0.5	0.199	8.74	9.79	10.87	12.00	13.15	14.33	15.54	16.77
1.0	0.199	5.44	6.23	7.07	7.94	8.85	9.80	10.78	11.78
0.1	0.401	5.91	6.93	8.03	9.20	10.44	11.74	13.11	14.52
0.5	0.401	3.67	4.42	5.24	6.13	7.09	8.11	9.19	10.34
1.0	0.401	1.76	2.21	2.72	3.29	3.93	4.62	5.38	6.19

***c) Polysulfide solubility determination with impedance spectroscopy***

As explained in Section 4.1, the polysulfides change the electrolyte's properties during battery operation. A technique to characterize the polysulfide solubility in different electrolyte mixtures was consequently needed for better understanding. To test this, impedance spectroscopy was used. Spectra were measured in PEIS mode with the amplitude of 10.0 mV between the frequencies of 1 MHz and 10 mHz. Measurements were done on freshly assembled cells and also on charged cells after 10 cycles of battery use at C/10 rate. The inverse values (for conductance) are plotted in Figure 17.

If we compare the resistive intercepts of fresh battery cells (Figure 17a) to the conductivity measurements of the electrolytes (Figure 16a), we see that the trends are in good agreement. Values cannot be compared directly, since the cell constant was not determined and the coffee bag setup is not advanced enough to exclude the measurement disturbance effect.<sup>106</sup> The small deviations from the conductivity data seen for electrolytes with  $X_{[\text{DEME}][\text{TFSI}]} = 0.2$  is attributed to poor temperature regulation during pouch cell measurements. Differentiation between the resistance of the electrolyte in the separator and the cathode pores was not made.

After 10 cycles of battery use, a change in resistance for electrolytes with lower LiTFSI salt concentrations and high dioxolane content can be observed (Figure 17b). This indicates higher polysulfide solubility. The least difference is shown when 1.0 M electrolyte was used. That is supported by findings in the literature, which show high salt concentrations in electrolytes can suppress polysulfide dissolution.<sup>107,108</sup> Smallest changes are also evident for high ionic liquid contents, which is supported by claims of poor polysulfide solubilities in ionic liquid based electrolytes.<sup>63</sup>

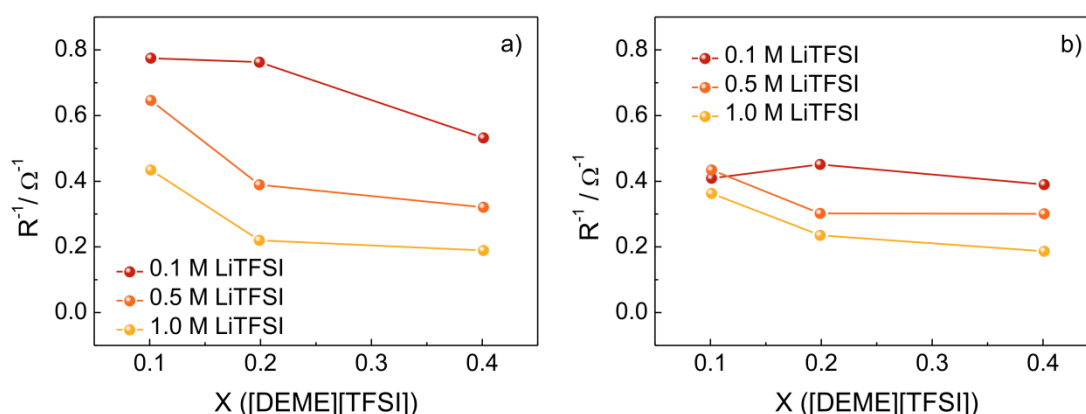


Figure 17: Conductance of the electrolyte mixtures determined from resistive intercept measurements a) freshly assembled battery cells with no polysulfides dissolved, b) after the 10<sup>th</sup> charge. Concentration of the LiTFSI salt varied from 0.1 to 1.0 M and the  $X([\text{DEME}][\text{TFSI}])$  between 0.1, 0.2, and 0.4.

#### d) Connection of physicochemical properties with electrochemical performance

Comparison of the electrochemical performance of the different mixtures of electrolytes was done by comparing the change due to the difference of ionic liquid content at the same salt concentration and the opposite, by evaluating the influence of changing the concentration of LiTFSI in the same  $[\text{DEME}][\text{TFSI}]:\text{DOL}$  mixture. All the batteries in this study were constructed with 20  $\mu\text{L}$  of electrolyte per mg of sulfur in the cathode and Celgard 2400 separator. Cells were cycled at C/10 rate between 1.5 V and 3.0 V vs. Li/Li<sup>+</sup> for 100 cycles. Electrode size was 1.5 cm<sup>2</sup>.

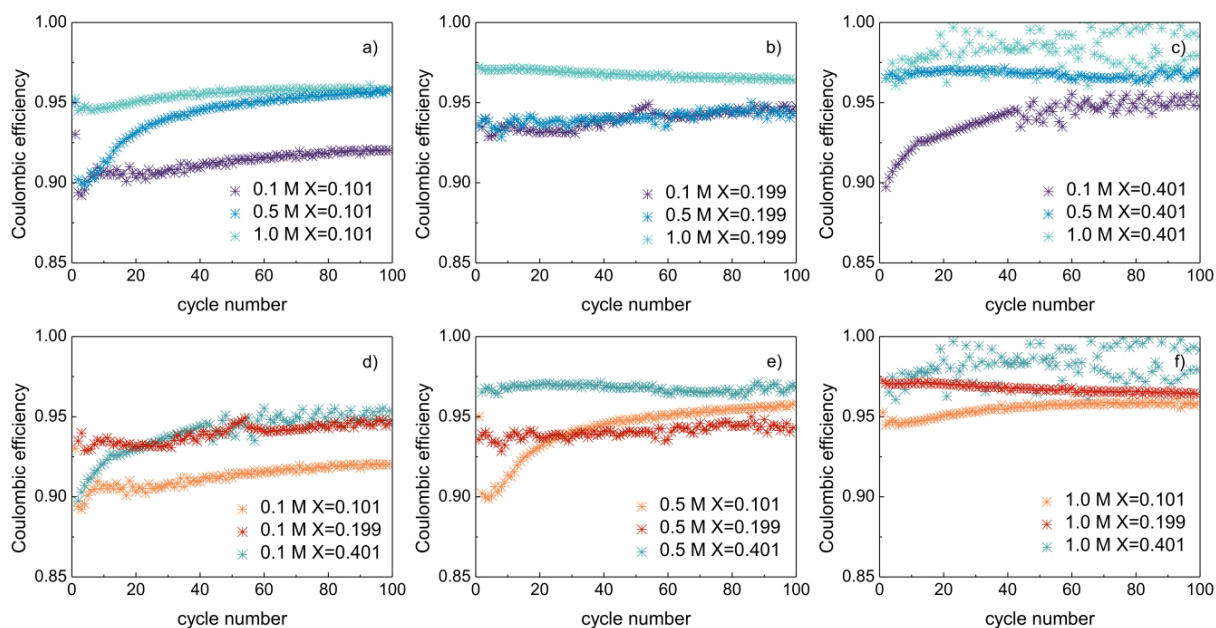


Figure 18: Coulombic efficiencies over 100 cycles. a-c shows a comparison of mixtures with the same ionic liquid molar content and different concentrations of LiTFSI salt with a)  $X=0.101$ , b)  $X=0.199$ , c)  $X=0.401$ . d-f show the comparison of performance of electrolytes with the same LiTFSI concentration with d) 0.1 M LiTFSI, e) 0.5 M LiTFSI, f) 1.0 M LiTFSI. X represents the molar ratio of [DEME][TFSI] in its mixture with DOL.

**Coulombic efficiencies** range from 90% (electrolytes with low LiTFSI concentrations) to almost 100% (1.0 M LiTFSI) (Figure 18a-c). They also differ with changing the ionic liquid-solvent ratios. Higher dioxolane content results in lower efficiencies (Figure 18d-f). These trends can be connected with polysulfide solubility (Figure 17). The electrolytes with poor polysulfide solubility show a smaller polysulfide shuttle extent and better charging efficiencies. We suspect that the difference in passivation of lithium between the mixtures is minimal.

The **overpotential** is usually considered an indicator for the internal impedance of the battery and it consists of the ohmic, concentration and activation polarization.<sup>109</sup> The values we show here were calculated as half the difference in potentials between discharge and charge curves at approximately 50% DOD. They range from 170 mV to 50 mV. The trend is different from the one shown for cycling efficiencies. The smallest overpotentials are exhibited for electrolytes with high lithium salt concentrations (Figure 19a-c) and with low ionic liquid content (Figure 19d-f), which we attribute to viscosity differences.

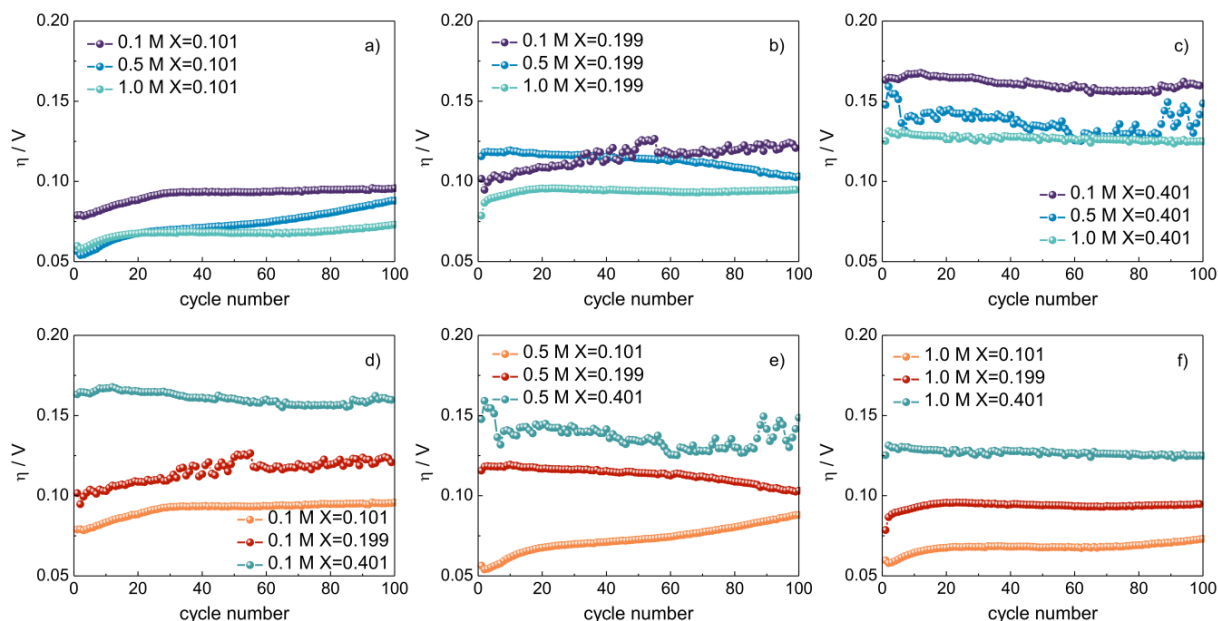


Figure 19: Overpotentials over 100 cycles: a-c show a comparison of mixtures with the same ionic liquid molar content and different concentrations of LiTFSI salt with a)  $X=0.101$ , b)  $X=0.199$ , c)  $X=0.401$ ; d-f show the comparison of performance of electrolytes with the same LiTFSI concentration with d) 0.1 M LiTFSI, e) 0.5 M LiTFSI, f) 1.0 M LiTFSI.  $X$  represents the molar ratio of [DEME][TFSI] in its mixture with DOL.

To better understand the reasons behind these values, a comparison of the impedance spectra after 10 cycles was also made (Figure 20). From that, smaller resistances are seen for lower salt concentrations. This showed that the concentration polarization contribution should be taken into account when assessing overpotentials for electrolytes with low lithium salt concentrations.

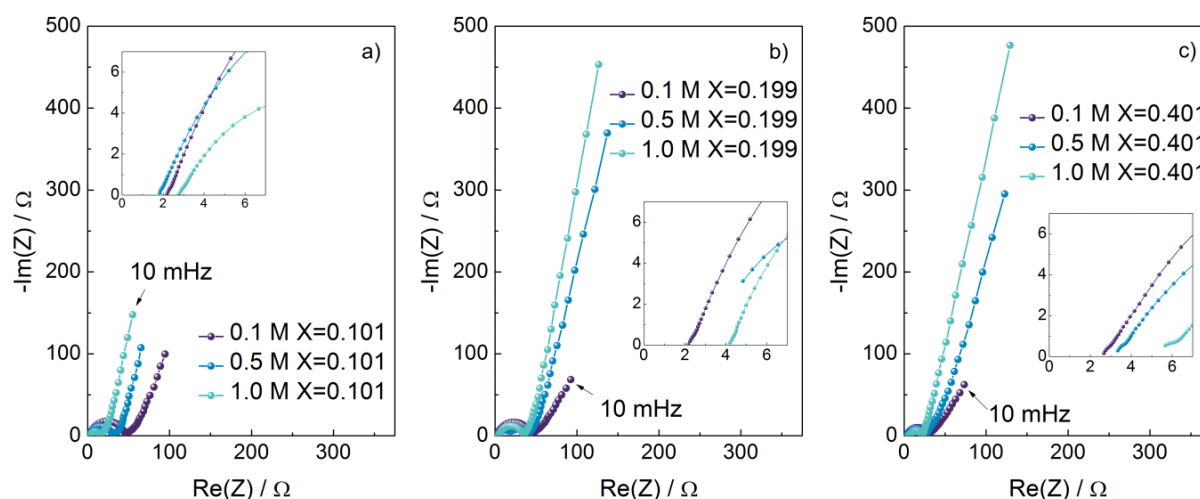
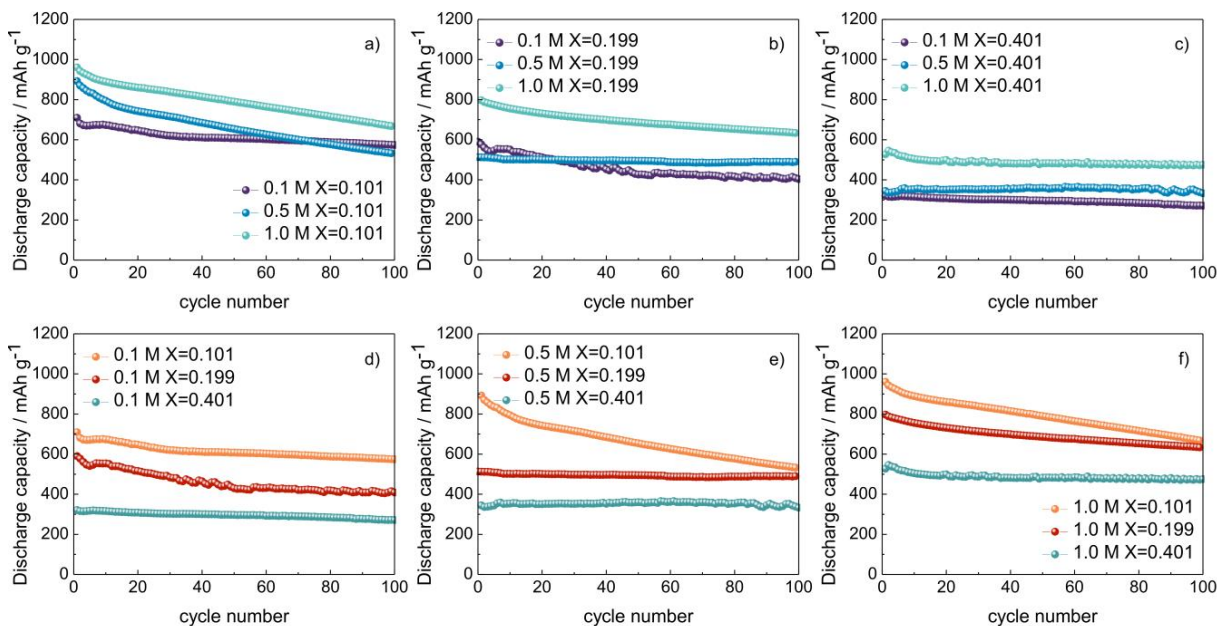


Figure 20: Impedance spectra for charged battery cells after 10 cycles of use, comparison of different lithium salt concentrations in the same compositions of dioxolane and ionic liquid: a)  $X=0.101$ , b)  $X=0.199$ , c)  $X=0.401$  (Insets show the high frequency regions of the spectra).  $X$  represents the molar ratio of [DEME][TFSI] in its mixture with DOL.

Specific capacities trend (Figure 21) follows a reverse trend of that shown for overpotentials (Figure 19).



**Figure 21:** Specific discharge capacities trend over 100 cycles: a-c show a comparison of mixtures with the same ionic liquid molar content and different concentrations of LiTFSI salt with a)  $X=0.101$ , b)  $X=0.199$ , c)  $X=0.401$ ; d-f show the comparison of performance of electrolytes with the same LiTFSI concentration with d) 0.1 M LiTFSI, e) 0.5 M LiTFSI, f) 1.0 M LiTFSI.  $X$  represents the molar ratio of [DEME][TFSI] in its mixture with DOL.

The highest capacities were reached for the 1.0 M LiTFSI in  $X_{[\text{DEME}][\text{TFSI}]} = 0.101$ . Additional capacity fade was expected for electrolytes with higher dioxolane contents, which is to some extent visible in the comparison for electrolytes with the same Li<sup>+</sup> salt concentration (Figure 21d-f). Larger capacity fades are shown for higher dioxolane contents. The trends would most likely result in lower capacities of the currently best performing electrolyte if the cells would be cycled further.

The density and conductivity of the electrolyte do not show a clear connection to any of the battery performance parameters determined in our study. The reason is probably in the fact that an ionic liquid electrolyte was used. In this case many charged species contribute to the determined conductivity with the case being even further complicated by dissolution of polysulfides, while only the Li<sup>+</sup> ion charge is important for battery operation.

If comparing electrolytes with the same Li<sup>+</sup> salt molarities, a connection between viscosities (Figure 16b), overpotentials (Figure 19d-f), ohmic resistance values (Figure 20) and discharge capacities (Figure 21d-f) is visible. This could be interpreted as hampering of the diffusion of polysulfide species, which consequently increases the low frequency segment of the impedance spectra. With electrolytes with different LiTFSI concentrations, the link is more complicated, since the overpotential is influenced by both the ohmic resistance as well as the

concentration polarization.<sup>109</sup> When employing electrolytes with low  $\text{Li}^+$  salt concentrations, the concentration polarization is an important contribution, which affects the specific capacity (Figure 19a-c, Figure 21a-c).

For our electrolyte system, the polysulfide solubility is a function of the amount of ionic species present in the electrolyte (Figure 17). Higher salt concentrations or ionic liquid content slow the dissolution of polysulfide species. In binary solvent electrolyte, this correlation would depend upon the solubility of polysulfides in both chosen components. The polysulfide solubility shows an impact on Coulombic efficiencies (Figure 18) and can be in some cases connected to an increase in capacity fade (Figure 21).

In terms of stability and specific capacity retention, the best performance was shown for 1.0 M LiTFSI in  $X_{[\text{DME}][\text{TFSI}]} = 0.199$  electrolyte. In the first cycles, it did exhibit capacities slightly lower than 1.0 M LiTFSI in  $X_{[\text{DME}][\text{TFSI}]} = 0.101$ , which we ascribe to higher viscosity and high ionic liquid content.

In general, for the best electrolyte performance, enough  $\text{Li}^+$  salt should be dissolved in the electrolyte so there is no concentration polarization issue. In order to achieve good efficiencies and minimum capacity fade, polysulfide solubility should be low. Capacity fade due to loss of contact in the cathode and anode stability was not investigated, although we speculate it can play an important role in the electrolyte performance.

#### 4.1.2 Electrolytes with poor polysulfide solubility

##### *a) Li–S battery performance of TFEE:DOL electrolyte system*

As evident from the study of the influence of electrolyte's physicochemical properties, low polysulfide solubility can be beneficial. It is therefore no surprise that one of the novel ways of reducing polysulfide shuttle issue involves the use of electrolytes which sparingly solute polysulfides<sup>110–114</sup>. With the use of those electrolytes, high-energy Li–S batteries can be constructed with lower electrolyte amounts and higher sulfur loadings.

These type of "sparingly soluble electrolytes" were investigated by determining the performance of TFEE (1,2-(1,1,2,2-tetrafluoroethoxy)ethane) based electrolytes. For the experiment, batteries were constructed with 20  $\mu\text{L}$  of electrolyte per mg of sulfur and Celgard 2400 separator. Electrode size was 1.5  $\text{cm}^2$ . Cycling was done as a rate capability test (settings described in Section 0). If we compare the battery performance of a standard electrolyte mixture of 1 M LiTFSI in TEGDME:DOL 1:1 (v:v) with that of 1 M LiTFSI in TFEE:DOL 1:1 (v:v), we see a small improvement in discharge capacity in the first cycles and a remarkable increase in Coulombic efficiency, which changes from approximately 82% for TEGDME based electrolyte to around 97% for TFEE one (Figure 22a).

A difference between the two electrolytes is also visible in their voltage profiles (Figure 22b). The high-voltage plateau in the fluorinated ether based electrolyte is around 150 mV lower than the voltage plateau in TEGDME one. The low voltage plateau is at a similar potential close to the thermodynamic one in both systems. This shift is attributed to be thermodynamic, not kinetic, since a shift to lower potentials is also visible in the charge profile of the battery.

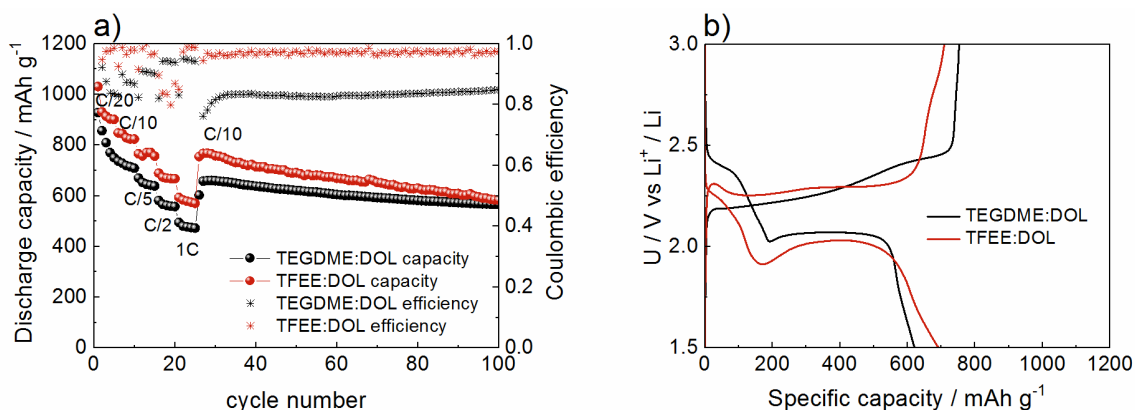


Figure 22: Electrochemical performance of TFEF based electrolyte compared to a conventionally used TEGDME based one a) capacity and coulombic efficiency at different C-rates, b) voltage profile in the 50<sup>th</sup> cycle. Solvent ratio was kept to 1:1 (v:v).

This reasoning was tested with GITT experiment on a high sulfur loading Li–S cell (Figure 23). GITT was performed at C/20 with stopping the current every 60 minutes and waiting until the potential stabilized to  $dE/dt < 15 \text{ mV h}^{-1}$ . For the “traditional” TEGDME based electrolyte, electrolyte volume was increased to 15  $\mu\text{L}$  per mg S and GITT experiment modified to stop every 30 minutes. High voltage plateau OCV for the fluorinated ether electrolyte is indicated to be 2.25 V vs. Li/Li<sup>+</sup> and for the “traditional” electrolyte at 2.40 V vs. Li/Li<sup>+</sup>.

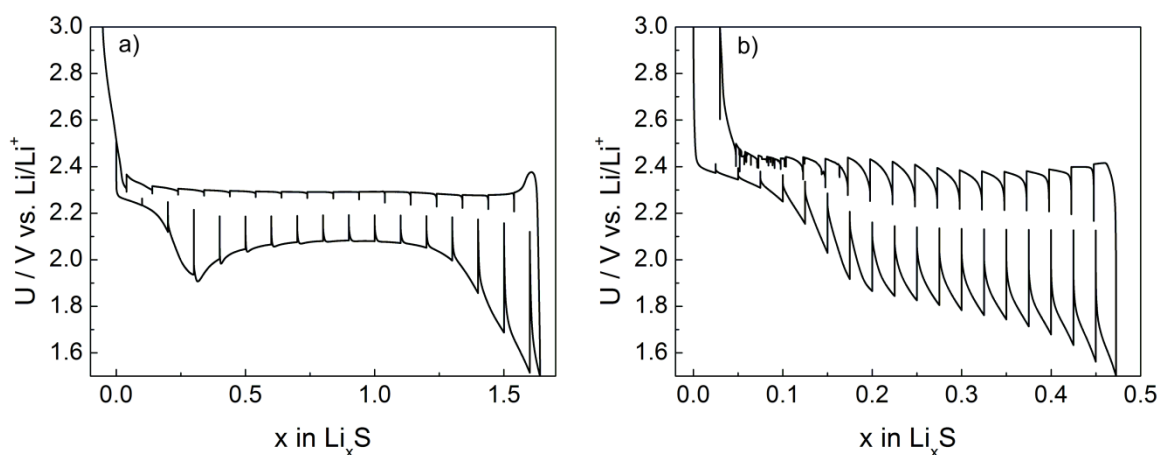
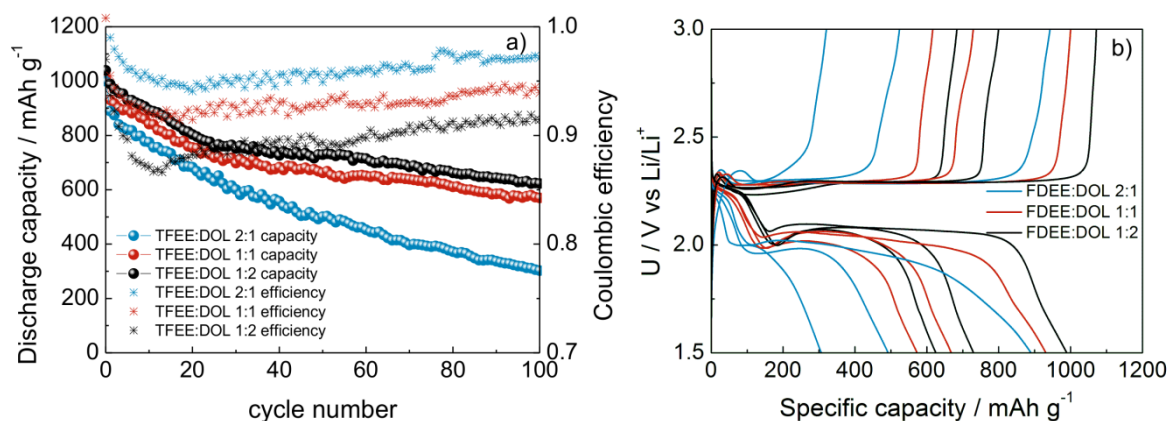


Figure 23: GITT experiment comparison a) Li–S cell with 1 M LiTFSI TFEF:DOL 1:1 (v:v). Electrode loading was 3.8 mg S cm<sup>-2</sup>, 6.5  $\mu\text{L}$  of electrolyte per mg S was used and one layer of Celgard 2400 separator. b) Li–S cell with the “traditional” electrolyte composition 1 M LiTFSI in TEGDME:DOL 1:1 (v:v). Setup was similar as with a) with the exception of electrolyte amount (15  $\mu\text{L}$  of electrolyte per mg S) and GITT setting (current stopped every 30 minutes).

To check the influence of the two electrolyte components (TFEE and DOL), three different mixtures were tested. Mixtures with volume ratios of 1:1, 1:2 and 2:1 were tested with the same battery cell setup by cycling them at  $C/10$  for 100 cycles (Figure 24). The electrolyte mixture with highest DOL content showed best capacities, but as expected exhibited poor cycling efficiencies due to high polysulfide solubility. The trend continued with intermediate cycling efficiencies and specific capacities for 1:1 (v:v) mixture and best Coulombic efficiencies for the TFEE:DOL 2:1 electrolyte.



**Figure 24:** Cycling behavior at for electrolytes prepared from different mixtures of TFEE and DOL –1:2; 1:1; 2:1 (all v:v mixtures with 1 M LiTFSI) a) discharge capacity and coulombic efficiency during 100 cycles of use, b) charge and discharge voltage profiles for 2<sup>nd</sup>, 50<sup>th</sup> and 100<sup>th</sup> cycle of use.

As it is evident from discharge and charge profile of the electrolytes shown on Figure 24b, higher contents of TFEE increase the overpotential. We attribute this to an increase in the viscosity of the electrolyte, which changes with the addition of TFEE from 0.0027 Pa\*s for the 1:2 mixture, 0.0035 Pa\*s for the 1:1 mixture to 0.0045 Pa\*s for the 1 M LiTFSI in TFEE:DOL 2:1 mixture. From this experiment we concluded that the best mixture for high-energy Li-S cell experiment would be the 1 M LiTFSI in TFEE:DOL 1:1 (v:v). The optimized electrolyte mixture was used to construct a high-energy Li-S battery cell.

Higher sulfur loading cathodes with 4 mg of S per cm<sup>2</sup> (Fraunhofer ISIT, 2 cm<sup>2</sup>) were used and 6.5  $\mu$ L of electrolyte per mg of S. With only one layer of Celgard 2400 separator used at  $C/10$  cycling, the battery showed great performance for the first 25 cycles, where it delivered over 1000 mA h g<sup>-1</sup> with efficiencies just under 97% (Figure 25). After 25 cycles, cell dry out caused lithium dendrites and an internal short circuit. The limiting factor for sulfur utilization was tested by increasing the electrolyte amount with performances delivered as depicted on Figure 25. Besides increasing the first discharge capacity (to 80% sulfur utilization), increasing the amount of electrolyte compromises the Coulombic efficiencies, since a higher amount of DOL is present in the cell. The extent of capacity fade is similar in both cases. The cell with higher electrolyte amount could be cycled for longer, supporting the hypothesis that Li metal anode consumes the electrolyte and causes the cell failure.

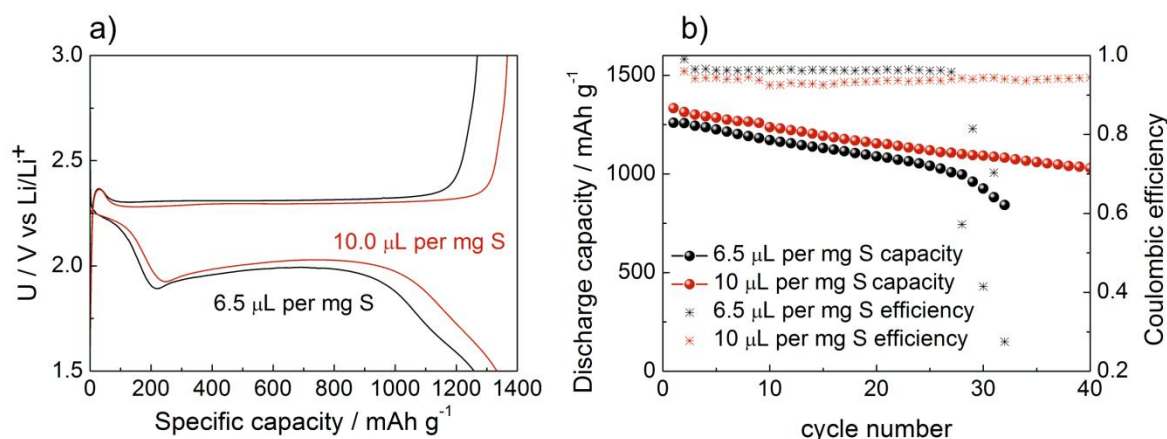


Figure 25: Discharge capacity and Coulombic efficiency for a high energy Li–S cell with 6.5  $\mu\text{L}$  per mg S and 10  $\mu\text{L}$  per mg S of 1 M LiTFSI TFEEDOL 1:1 electrolyte. Sulfur loading was 4 mg cm<sup>-2</sup>.

Lithium metal stability was investigated with disassembly of the high energy cell (Figure 25). Color of the separator remained unchanged and close to white as it can be seen from Figure 26. There are visible dendrites going through the polyolefin separator and the surface of the anode is drastically changed to almost black color, mossy and fragile (Figure 26b).

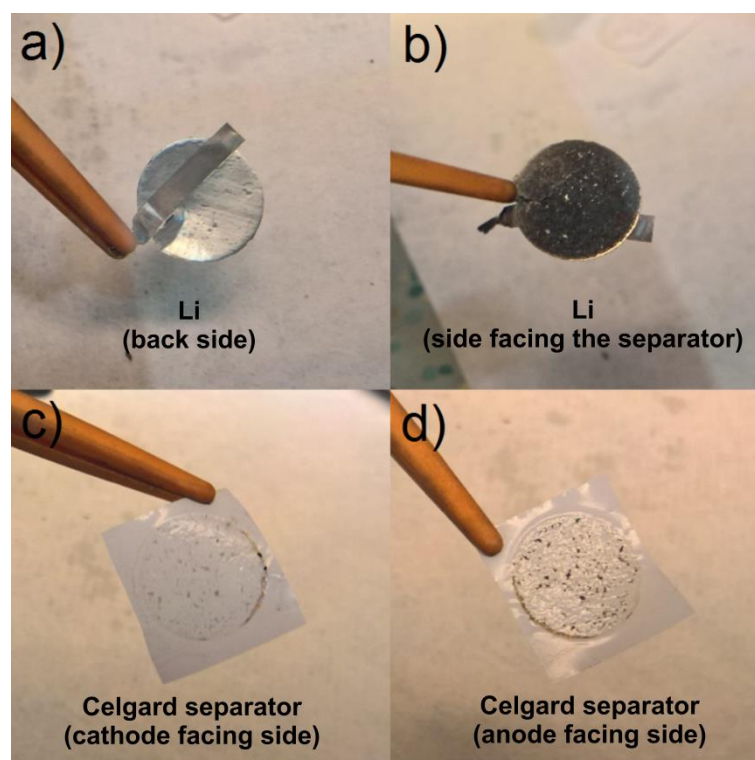


Figure 26: Post mortem analysis on the high energy Li-S battery cell, a) side of the anode which was facing away from the separator, b) Li surface after cycling, c) Celgard 2400 separator with the cathode facing side, d) Celgard 2400 separator with the anode facing side

Another important indicator of poor lithium stability is impedance spectroscopy analysis on symmetrical Li||Li cells at OCV. Two 2 cm<sup>2</sup> Li electrodes were separated with one layer of Celgard 2400 separator and wetted with 20 μL of the chosen electrolyte (1 M LiTFSI TEGDME:DOL 1:1 or 1 M LiTFSI TFEE:DOL 1:1). The spectra were measured over a period of 50 hours from 20 kHz to 10 mHz with an amplitude of 10 mV (rms). On Figure 27, spectra at 1 h, 15 h, 25 h, 35 h and 45 h are shown. For the “traditional” electrolyte, the passive layer on Li seems to be complex with resistances reaching up to 300 Ω (high frequency arc). On the other hand, the resistive intercept, which indicates the electrolyte conductivity, does not drastically change and stays close to its initial value of 5 Ω. With TFEE:DOL electrolyte, the high frequency arc seems to be more stable (values around 60 Ω). What is important to note is that the resistive intercept for the TFEE electrolyte changes from 10 Ω up to 35 Ω. This is accompanied with larger diffusional resistances (seen from the low frequency contribution on the last red spectrum on Figure 27), which indicates that Li reacts with the fluorinated ether based electrolyte’s components, making the solution more viscous and increasing the electrolyte and diffusion resistances. All of this adds an additional proof that Li instability is the reason behind capacity fade, although it is also important to note that the stability of Li in full Li–S cell setup is also influenced by the presence of polysulfide species.

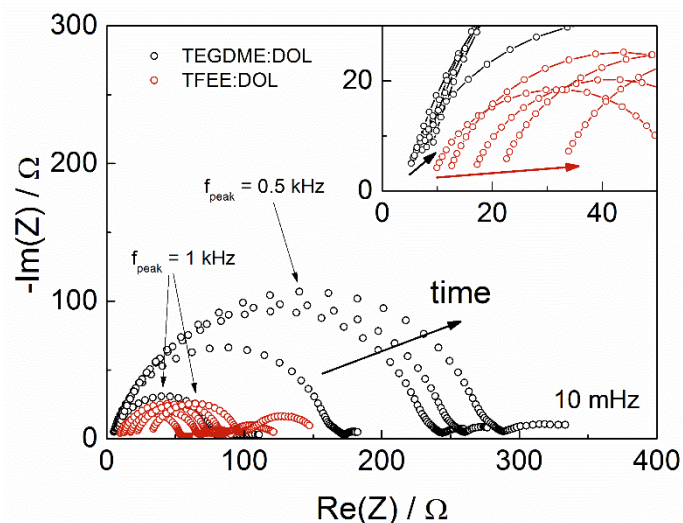
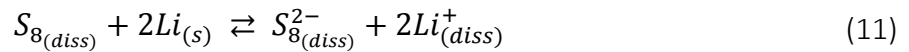


Figure 27: Impedance spectra of Li||Li symmetrical cells (2 cm<sup>2</sup>) measured at OCV over the course of 50 hours. Spectra were measured consecutively in the range of 20 kHz–10 mHz with the amplitude of 10 mV (rms), while measurements at 1 h, 15 h, 25 h, 35 h and 45 h are shown on the figure. Inset shows the high frequency part of the spectra more clearly; all arrows indicate change with time. Cells were constructed with one layer of Celgard 2400 separator and 20 μL of chosen electrolyte.

### b) Mechanism investigation of TFEE:DOL electrolyte

The open questions about the reason for a difference in plateau voltages were explored further with different analytical techniques and modelling.

If the reaction, which governs the high-voltage plateau, is one where  $\text{Li}_2\text{S}_8$  polysulfide is formed from dissolved sulfur, the Nernst equation suggests that the open circuit potential will depend upon the activity of the polysulfide and sulfur species dissolved in the electrolyte (Equations 11-13). If we compare this with experimentally observed relationship between the potentials in the electrolytes tested (13), we can speculate that the reason for the difference in potentials is in the ratio of solubility of polysulfides and sulfur. These statements were further investigated with COSMO-RS modelling done by dr. Steffen Jeschke and dr. Patrik Johansson at Chalmers University of Technology in Gothenburg.<sup>115</sup>



$$E = E^0 - \frac{RT}{zF} \ln \frac{a_{\text{S}_{8(\text{diss})}^{2-}} a_{\text{Li}^{+}}^2}{a_{\text{S}_8}} \quad (12)$$

$$E_{\text{TEGDME}} > E_{\text{FDEE}} \quad (13)$$

Through DFT computation of surface charge density, statistical thermodynamics are used for the calculation of chemical potentials of species in a solution with a method called Conductor-like-Screening Model for Real Solvents (COSMO-RS)<sup>116-119</sup>. The relative difference in solubility of  $\text{Li}_2\text{S}_8$  species was calculated to be 1000x smaller in the TFEE based solvent as compared to the more conventionally used TEGDME based one. This calculation is in good agreement with data obtained experimentally. The solubility of  $\text{Li}_2\text{S}_8$  in 1 M LiTFSI in TEGDME:DOL 1:1 (v:v) is over 1.0 M and in the 1 M LiTFSI in TFEE:DOL 1:1 (v:v) between 2 mM and 5 mM. For  $\text{S}_8$  molecules, the solubility through COSMO-RS could be calculated as an absolute value with the concentration of 1.2 mM in TEGDME electrolyte and 0.4 mM in TFEE one.

The Equation 13 was investigated with calculating the difference in chemical potentials between two solvents (TEGDME of TFEE based ones) for both of the two species of interest ( $\text{S}_8^{2-}$  and  $\text{S}_8$ ). The results confirmed the validity of the experimentally observed relationship. Furthermore, the calculated chemical potential of the  $\text{S}_8^{2-}$  species is more negative in TFEE based electrolyte than in the TEGDME one, suggesting higher preference for the TFEE electrolyte, but the chemical potential of  $\text{Li}^{+}$  is more positive. This means that the reason for the decrease in  $\text{Li}_2\text{S}_8$  solubility in fluorinated solvents is in the poor solvation of  $\text{Li}^{+}$  ions. The chemical potential difference was calculated to be roughly -50 mV, which is qualitatively consistent with the experimentally observed -200 mV.

Solvation of  $\text{Li}^{+}$  ions was investigated with ATR-IR by measuring the spectra of TFEE, DOL and TFEE:DOL 1:1 solvents as well as solutions of LiTFSI in all of them (Figure 28). The

concentration of  $\text{Li}^+$  was chosen so that the molar ratio of LiTFSI in TFEE or in DOL would be the same as in 1 M LiTFSI in TFEE:DOL 1:1 (v:v), which is 1 : 8.7. LiTFSI could not be dissolved in that concentration in TFEE, which is a sign of the poor solvation. For this mixture, the IR spectrum of the saturated solution above the precipitate was measured. Nevertheless, no additional peaks were seen in that spectrum as compared to the one of the pure solvent, corroborating the hypothesis (Figure 28a).

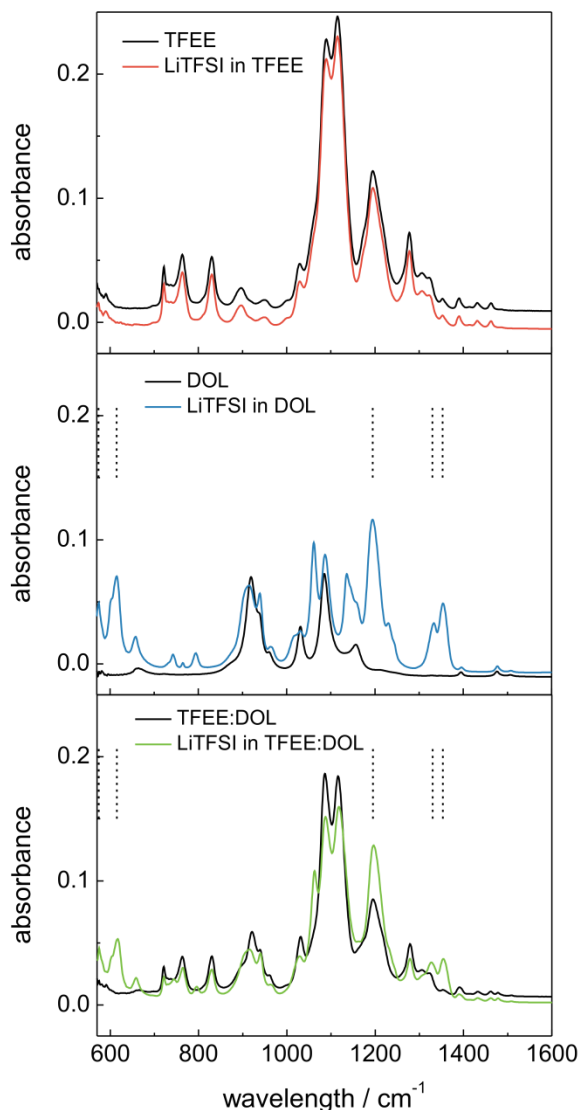


Figure 28: ATR-IR spectra of DOL and TFEE pure solvents, their 1:1 (v:v) mixture and the solutions with LiTFSI salt. Horizontal lines indicate additional bands due to LiTFSI

In the LiTFSI solution in DOL a few additional prominent absorption peaks are visible in the IR spectrum:  $1353\text{ cm}^{-1}$  (TFSI:  $\nu^{jp}$   $\text{SO}_2$ ),  $1330\text{ cm}^{-1}$  (TFSI:  $\nu^{op}$   $\text{SO}_2$ ),  $1195\text{ cm}^{-1}$  (TFSI),  $615\text{ cm}^{-1}$  (TFSI:  $\delta^{op}$   $\text{SO}_2$ ) and  $574\text{ cm}^{-1}$  ( $\delta_a$   $\text{CF}_3$ )<sup>120</sup> (Figure 28b). The same bands are also present in the LiTFSI solution in TFEE:DOL mixture (Figure 28c – dashed lines), supporting the claim that solvation of lithium ions in this electrolyte system is based on DOL.

To determine whether the mechanism of operation really does follow the conventional one through polysulfide dissolution and  $\text{Li}_2\text{S}$  precipitation, the formation of intermediate species was followed with *operando* sulfur K-edge X-ray absorption spectroscopy (XAS) and UV-vis measurements.

*Operando* sulfur K-edge XANES spectra were measured through the first discharge (Figure 29a) of the battery by using the 1 M LiTFSI TFE:EOL 1:1 (v:v) electrolyte. The spectra are shown in Figure 29b. The measurement setup and the cell configuration were the same as presented in publications.<sup>10,13,96</sup> To limit self-absorption effects<sup>13</sup>, electrodes with lower sulfur amount were used. Since self-absorption correction is not reliable due to the composition of the cathode constantly changing during the experiment, no self-absorption correction was applied. Although the calculated solubility of sulfur in TFE electrolyte is 10-times smaller than the determined solubility of  $\text{Li}_2\text{S}_8$ , the relative amount of sulfur and polysulfide species after 100 mAh  $\text{g}^{-1}$  is the same, which is a consequence of the mode of detection in XANES, where both solid phase and dissolved species are detected.

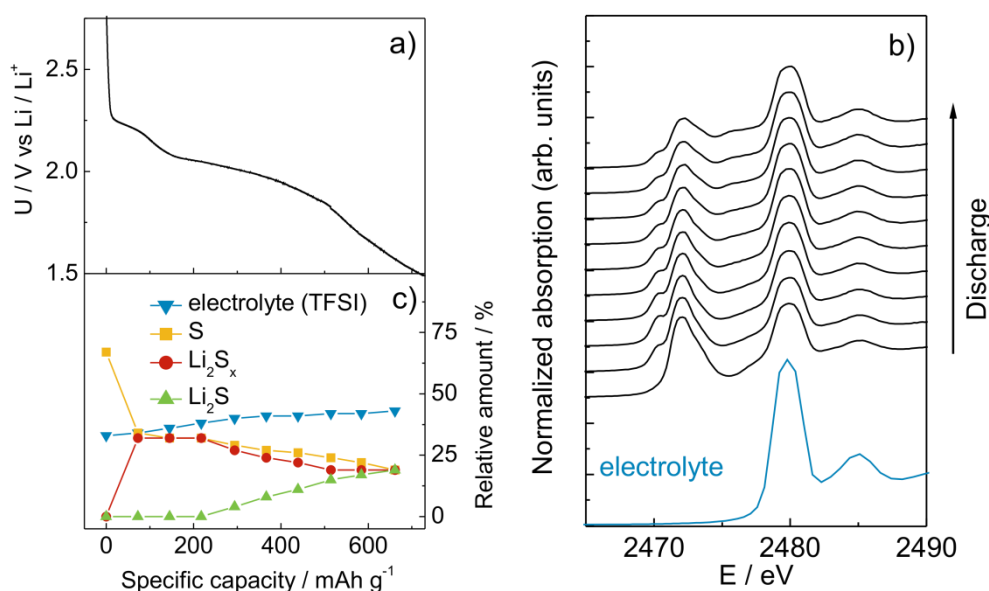


Figure 29: Sulphur K-edge XANES *operando* experiment a) electrochemical discharge profile measured, b) relative amounts of determined compounds, c) *operando* sulfur K-edge XANES spectra of the Li-S battery during the first discharge.

PCA (principle component analysis)<sup>103</sup> on the acquired set of spectra shows a linear combination of the four main components (electrolyte, sulfur, lithium polysulfides –  $\text{Li}_2\text{S}_x$  and lithium sulfide –  $\text{Li}_2\text{S}$ ) to be sufficient to describe each XANES spectrum. The reference spectra for the electrolyte was measured diluted with BN beforehand, while the spectra of the other three components were measured and extracted from a set of *operando* spectra in a similar battery in a different study.<sup>10</sup>

The relative amounts for the four sulfur species present in the battery (three before mentioned ones and the sulfonate group from the LiTFSI salt in the electrolyte) were determined with a linear combination fit (LCF, Figure 30). The main characteristics of the spectra (absorption edges and pre-edge resonances) in the spectra are at different energies, which allows for low uncertainty in the LCF. The fit is performed in the energy region from 245 eV to 2502 eV.

With this measurement, polysulfide presence during battery operation was confirmed.  $\text{Li}_2\text{S}$  was also detected from the beginning of the low discharge plateau on. From this we conclude that the mechanism of operation in TFE based solvent is the same as in traditional electrolytes, nevertheless solubility of polysulfides is much lower.<sup>10</sup>

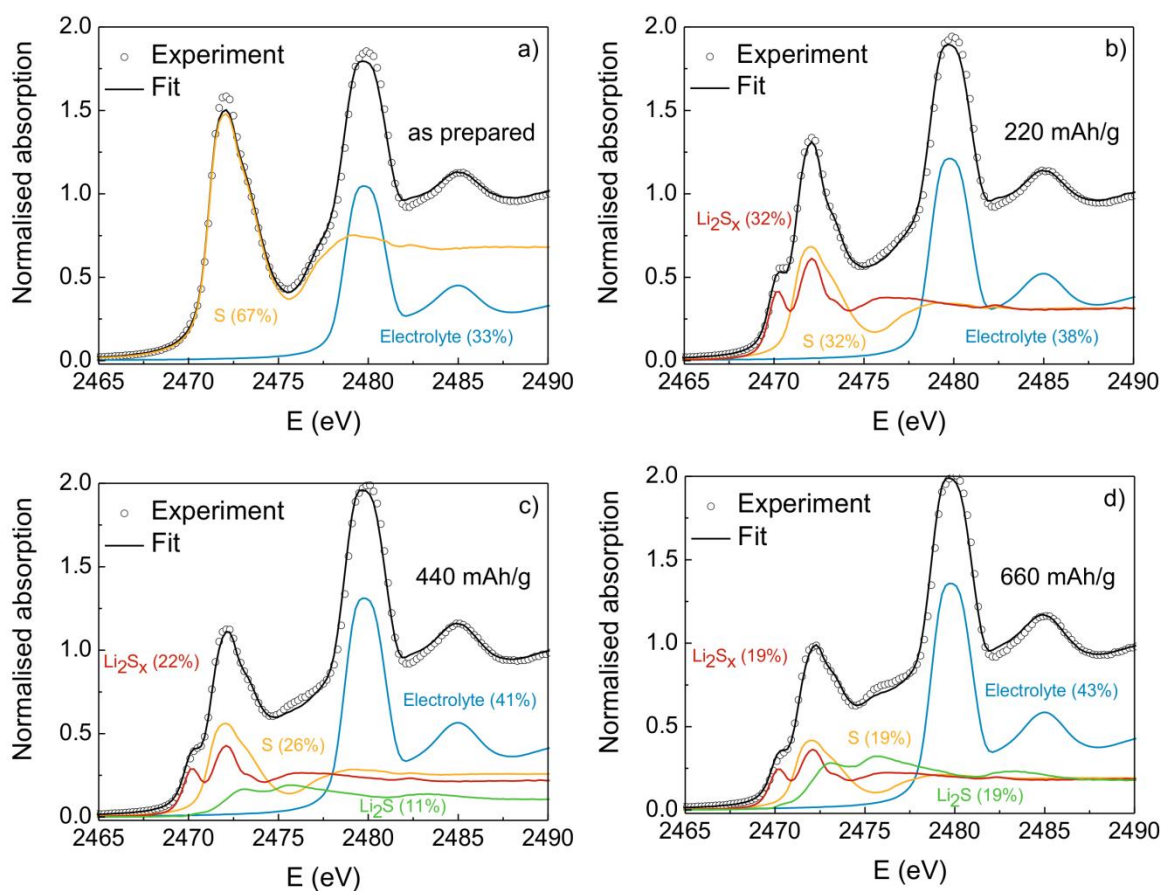


Figure 30: Linear combination fit of the sulfur K-edge XANES spectra in the intermediate states during discharge: (a) as prepared, (b)  $220 \text{ mAh g}^{-1}$ , (c)  $440 \text{ mAh g}^{-1}$ , and (d)  $660 \text{ mAh g}^{-1}$ . Open circles - experiment; black line- fit with linear combination of the four reference XANES profiles plotted below. The uncertainty of each component in the linear combination fit is  $\pm 1\%$  or lower.

For further insight on the length and concentration of polysulfides formed and their diffusion through the separator, *operando* UV-vis spectroscopy was used. The configuration of the cell and the measurement settings used were the same as in previous reports from our research group.<sup>94</sup> A relatively high amount of electrolyte was used for battery operation ( $60 \mu\text{L}$  per mg S).

The wavelengths of absorption peaks depend upon the chain length of the polysulfides, their concentration and the interaction between them and the electrolyte. On Figure 31, the UV-vis spectra during discharge of a battery with 1 M LiTFSI in TFEE:DOL 1:1 (v:v) electrolyte are shown. The battery reached a specific capacity of  $810 \text{ mAh g}^{-1}$  (Figure 31a). The formation of polysulfides was detected from the high-voltage plateau on. The peaks are shifted to shorter wavelengths compared to the conventional electrolyte<sup>94,95</sup> with an absorbance edge around 400 nm. Its intensity changes during battery operation, suggesting variations in concentration (Figure 31b).

For information on speciation, 2 mM standard solutions of  $\text{Li}_2\text{S}_8$ ,  $\text{Li}_2\text{S}_6$  and  $\text{Li}_2\text{S}_4$  polysulfides were prepared in 1 M LiTFSI in TFEE:DOL 1:1 (v:v). The positions of the absorption peaks are shown on Figure 31c. Long-chain polysulfides show absorbance in the region of 400 nm (Figure 31c – blue line). With shortening the chain length, a second absorption band appears in the region of 500 nm (Figure 31c). Since no absorption in that region was detected during battery operation, we conclude that only long-chained polysulfides diffused through the separator to be detected with the *operando* experiment. Semi-quantitative analysis suggests that the concentration of polysulfides is significantly lower than in “traditional” electrolytes.<sup>10</sup>

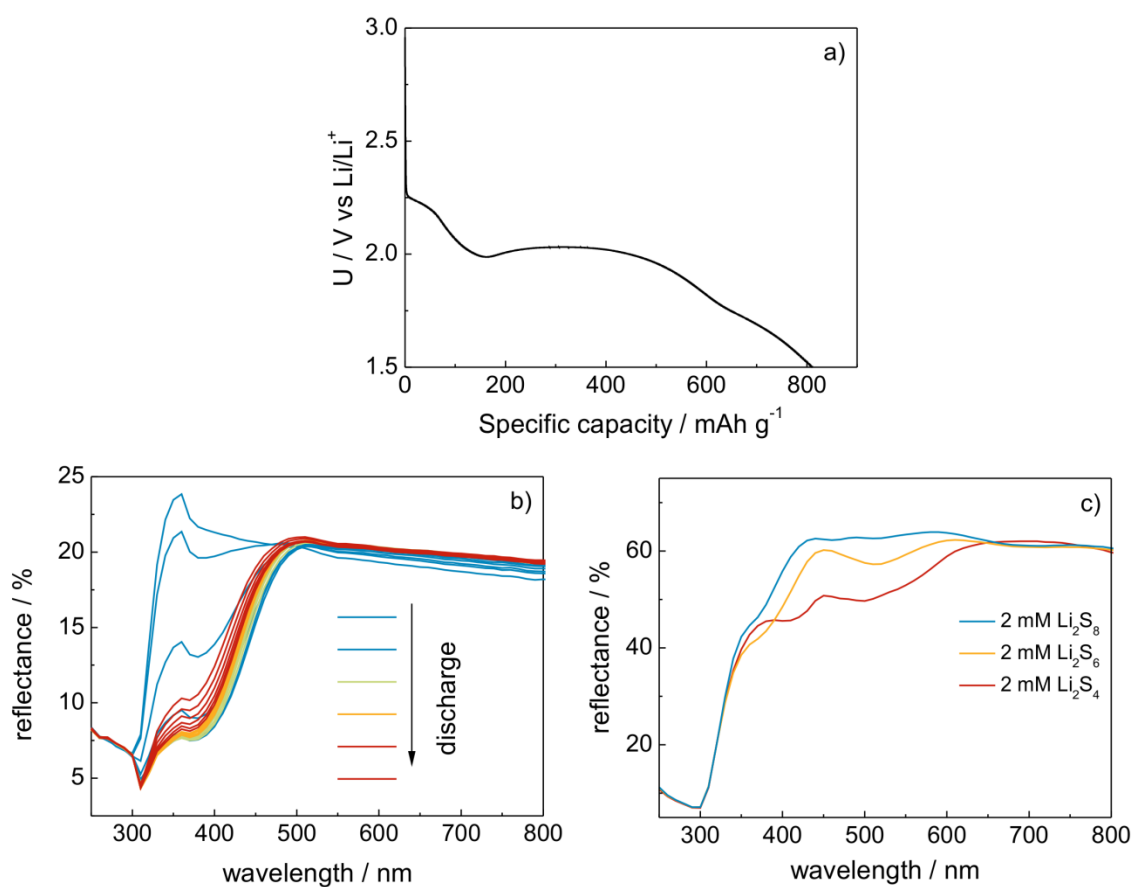


Figure 31: UV-vis spectroscopy experiment for 1 M LiTFSI TFEE:DOL 1:1 electrolyte, a) discharge and charge profile at C/20, b) spectra change during discharge and c) spectra of standard solutions in TFEE electrolyte,

This study enabled us to import insight into the electrolyte's role in the Li–S battery performance. We were also successful in preparing a high energy battery cell with low electrolyte content by employing fluorinated ether solvent based electrolyte, where solubilities of polysulfide species are 1000x smaller than in the “traditionally” used glyme based electrolytes.

As evident from Figure 12, besides the resistive intercept contribution ( $R_{el}$ ), other contributions present in the impedance spectrum significantly contribute to the cells' internal resistance. We were curious as to what are the other contributions or in other words which process most significantly determines the voltage and capacity the cell achieves during operation. In order to answer these questions, a more detailed impedance spectroscopy evaluation of Li–S battery cells at different DOD was conducted in continuation.

## 4.2 Reaction and diffusion contributions in the Li–S impedance spectra

If we move towards lower frequencies in the impedance spectrum of a Li–S battery cell, the contributions originate from the charge transfer reactions on the electrodes and diffusion of electroactive species. The response is further complicated by passivating films and other unwanted side reactions. From the spectra alone it is difficult to extract useful information. For example – without further experiments, one cannot state even if the contribution seen in the spectrum is coming from processes occurring on the anode or on the cathode. With this aim, we employed an approach where symmetrical cells were built.<sup>90,121</sup>

Anode-anode and cathode-cathode cells were assembled to simulate various DOD. Their impedance spectra down to 10 mHz were measured and the arithmetic mean of each frequency point calculated in order to visualise a “composited” spectrum on the basis of the symmetrical cells' measurements. The composited spectrum was then compared to the one measured on an actual battery cell. For a fresh battery, the symmetrical cells were easy to construct out of unused electrodes. To have reliable data for other DOD, two battery cells as identical as possible were constructed, discharged, their battery spectra measured and then disassembled inside the glove box. Out of their parts, two symmetrical cells were made (Figure 32) and the spectra of those were used in the study.

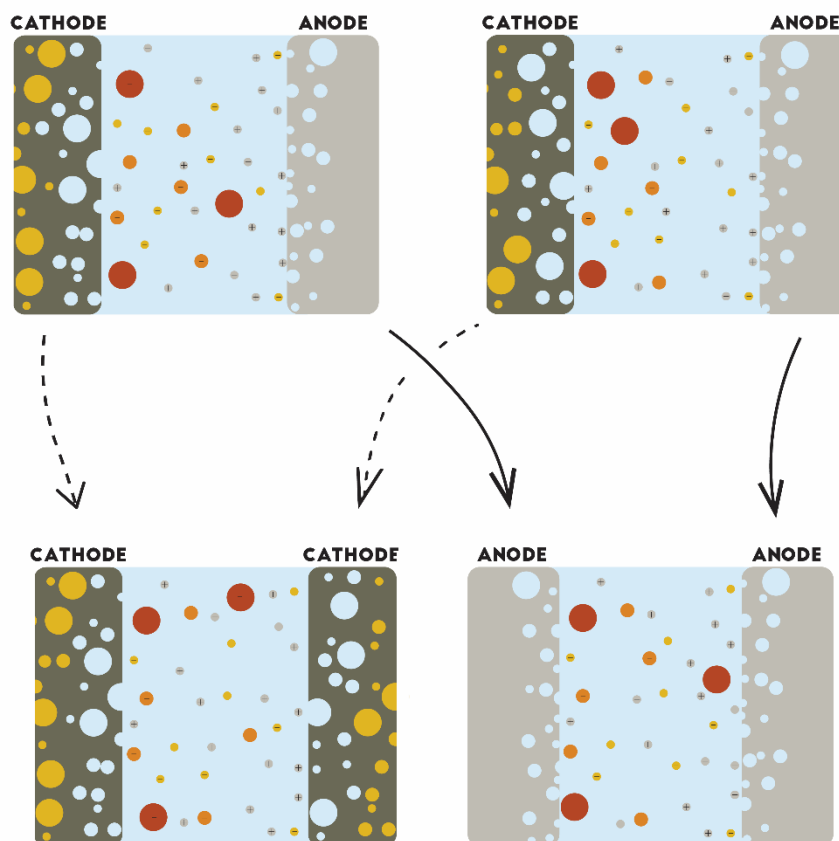
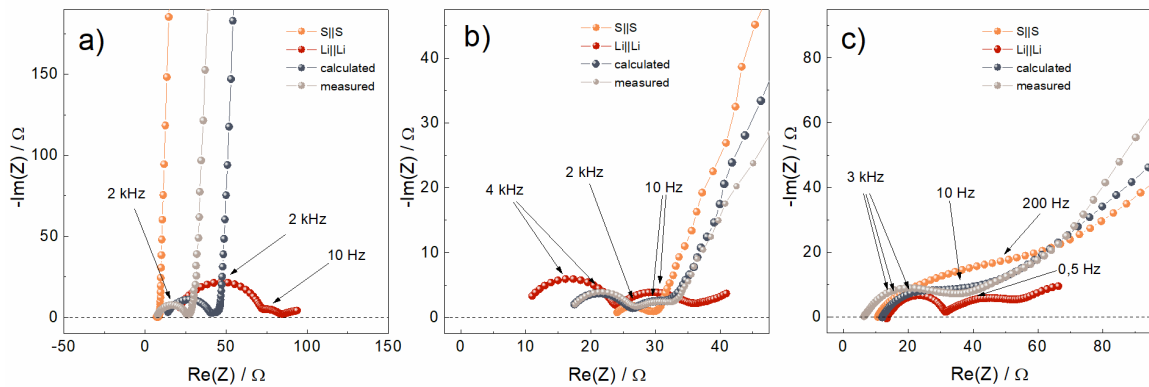


Figure 32: A schematic representation of symmetrical cells approach – two very similar discharged batteries (top) were disassembled and their parts used to construct two symmetrical cells (bottom).

The analysis of those spectra (Figure 33) gave us the information about which part of the battery spectra belongs to the anode contributions and which to the cathode. With fresh cells, the cathode contribution is “blocking” in nature (Figure 33a, orange), since sulfur is a non-conductive substance, none of it is dissolved yet and the resistances for redox reactions are big. Lithium on the other hand has a characteristic spectrum of one larger depressed semicircle and one smaller contribution at lower frequencies (Figure 33a, red).<sup>91,97,122</sup> The average spectrum of the cathode and anode spectra gives one very similar to the measured Li–S battery spectrum (Figure 33a, grey and black spectra). From this, we can conclude that the semicircle contribution in the fresh battery spectrum is from the anode and the blocking character from the cathode part. In general, the measured and calculated spectra matched remarkably well, any detected differences in the high frequency resistive intercept were attributed to unwanted electrolyte evaporation during pouch cell assembly. This difference was disregarded in this study, since we were mostly interested in determining whether a feature in the spectrum comes from the processes on the anode or from the cathode side of the cell.



**Figure 33:** Impedance spectra of symmetrical (orange for cathode-cathode and red for anode-anode cells) and battery cells (measured spectra in grey and calculated spectra in black). a) fresh battery, b) battery at approximately 50% DOD, c) fully discharged battery. Battery cells were constructed with  $1.5 \text{ cm}^2$  size, glassy fibre GF/D separator and  $60 \mu\text{L}$  per mg S of 1 M LiTFSI in TEGDME:DOL 2:1.

With discharging the battery to approximately 50% DOD (Figure 33b), the anode contribution decreases in size to almost a half, while still maintaining its shape. The cathode response gets a less blocking nature with a small semicircle at high frequencies and a large contribution in the low frequency part. The calculated and measured spectra are again in good agreement with the anode dominating the two high frequency semi-circles and cathode the low frequency response (Figure 33b, grey spectra).

Complete discharge (Figure 33c) only minimally changes the anode response, while increasing the cathode contributions in the high frequency region. The positive electrode still dominates the overall response with the low frequency part being the most significant impedance contribution.

### 4.3 Anode's contribution

The high frequency response R1, which we attributed to the anode by the symmetrical cells experiment, was followed through 50 cycles (explained in Section 4) and is depicted on Figure 34. The representation is similar as the one for the resistive intercept, although here, the z-axis (cycle number) is reversed for better clarity.

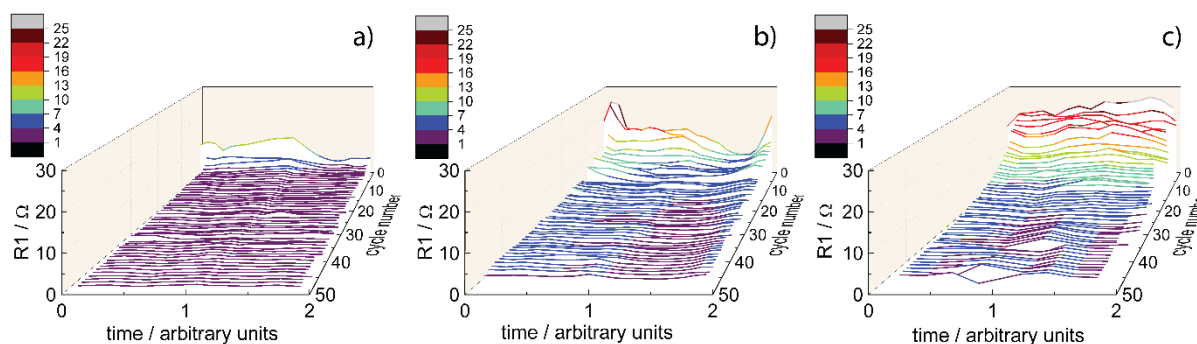


**Figure 34:** R1 (lithium anode contribution) change through 50 cycles at different DOD for three different electrolytes – a) 1 M LiTFSI in sulfolane:DOL 1:1, b) 1 M LiTFSI in TEGDME:DOL 2:1 and c) 1 M LiTFSI in [DEME][TFSI]:DOL 1:2.

The size of the anode resistance through the first discharge is a few 10  $\Omega$  (consistent with half the resistance of a Li | Li cell from Figure 33). Afterwards it decreases in all three electrolytes tested (albeit with different rates) and by the end of the 50<sup>th</sup> cycle measures only a few  $\Omega$ . Explanation of this phenomenon is in high surface area Li deposits (HSAL). Since the surface area of the electrode gradually increases, the resistance gets smaller. That also implies, that the anode resistance is insignificant compared to the cathode contributions after a few cycles. The double layer capacitance for this feature remains relatively constant through different DOD and further cycling and is of approximate value of 1  $\mu\text{F}$ , consistent with literature reports for charge transfer contributions.<sup>123</sup> This degree of size reduction is only the case when excess of electrolyte is present in the cell. If the cell dries out due to side reactions of Li anode with the electrolyte, the decrease in the anode contributions is not that pronounced.

#### 4.3.1 Lithium reaction with polysulfides

##### *a) Influence of polysulfide species on Li anode performance*

The anode response was further studied by incorporating polysulfides into the separator in symmetrical anode cells. We aimed to understand how polysulfides change the Li impedance response. Since the experiment on battery cells was done with an excess of electrolyte, the

polysulfide concentration during battery operation was relatively low. Tests on symmetrical cells were conducted with higher molarities of polysulfides to mimic the conditions of low electrolyte amounts.

Li||Li cells were prepared with  $2\text{ cm}^2$  electrodes with  $10\ \mu\text{L}$  of the conventional electrolyte  $1\ \text{M LiTFSI}$  in TEGDME:DOL 1:1 and with different nominal concentrations of  $\text{Li}_2\text{S}_8$  in that same solution ( $0.01\ \text{M}$ ,  $0.1\ \text{M}$ ,  $1.0\ \text{M}$ ). The impedance spectra of the batteries were measured to  $1\ \text{mHz}$  and followed through several days until the response stabilized (Figure 35a).

As expected, the resistive intercept change grows with the increase in polysulfide concentration and consequent increase in viscosity. In the cells before cycling, the internal resistance ( $R_{\text{el}}$ ) for “stabilized cells” increases from  $3\ \Omega$  (for the pure electrolyte and lowest polysulfide concentration) up to  $4\ \Omega$  for  $0.1\ \text{M Li}_2\text{S}_8$  and  $44\ \Omega$  for  $1.0\ \text{M Li}_2\text{S}_8$  solution.

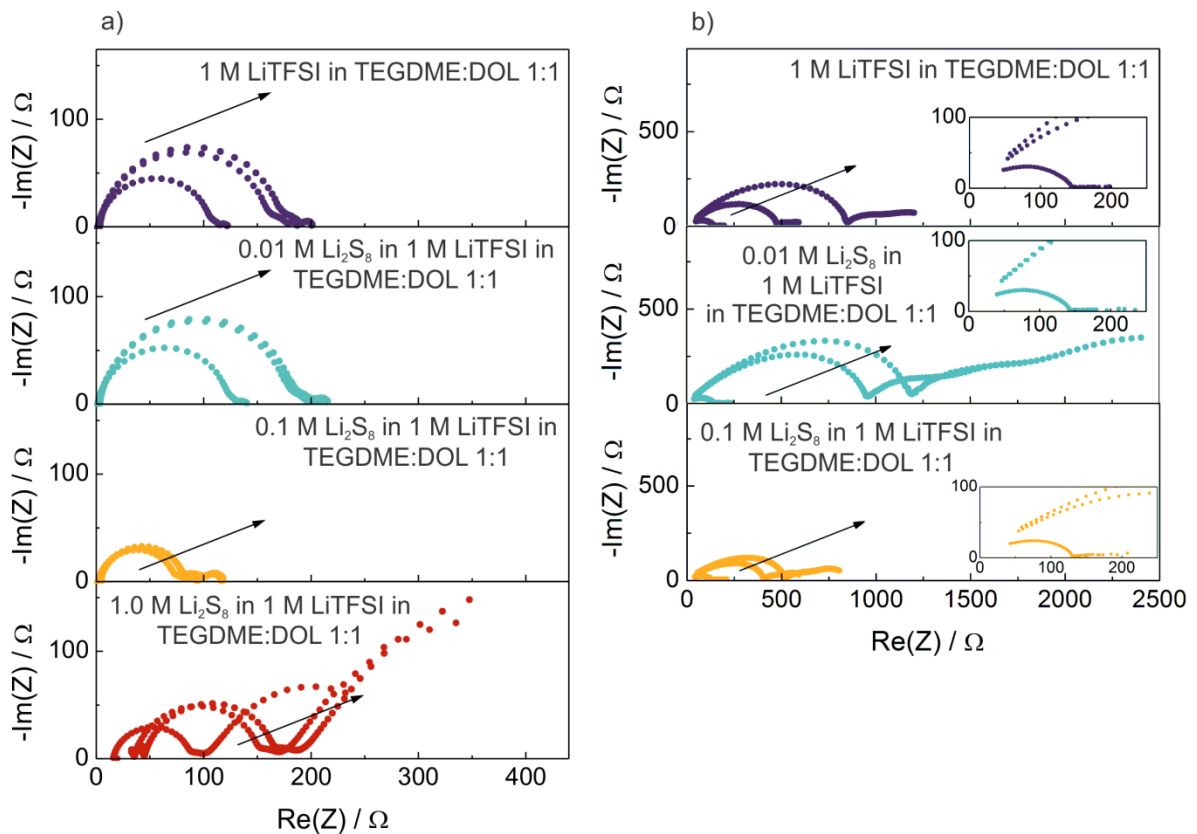


Figure 35: a) EIS spectra from  $1\ \text{MHz}$  to  $1\ \text{mHz}$  of symmetrical Li||Li cells with different catholyte compositions before stripping and deposition. b) EIS spectra for the same cells after 50 cycles of stripping and deposition. In all the figures, 1<sup>st</sup>, 50<sup>th</sup> and 100<sup>th</sup> spectra are shown which corresponds to 1 h, 66 h and 130 h after cell assembly on a) and 1 h, 66 h and 130 h after the end of stripping and deposition experiment on b). The direction of the arrow points to the increase with time. Insets on b) show magnification of the first measured spectrum after stripping and deposition experiment.

The high frequency arc does not change much with low polysulfide concentration. With higher concentrations its initial values are smaller, while the values for “stabilized” cells are

similar. The size evolution is in turn a mixed effect of a decrease due to higher  $\text{Li}^+$  concentration and an increase due to passive layer formation, which likely happens because of reduction and deposition of polysulfide species on the lithium metal surface.

The increased viscosity of the solution with the higher polysulfide concentration also changes the low frequency diffusion part, which increases from  $10 \Omega$ ,  $15 \Omega$  and  $20 \Omega$  (for the pure electrolyte, lowest polysulfide concentration and  $0.1 \text{ M}$  polysulfide concentration, respectively) up to  $250 \Omega$  for  $1.0 \text{ M}$   $\text{Li}_2\text{S}_8$  solution. This increases the overall impedance response from a few  $100 \Omega$  to over  $400 \Omega$  for concentrated polysulfide solutions.

Those same cells were then galvanostatically cycled using the program described in section 3.3.1. As evident from Figure 36, lower polysulfide concentrations ( $0.01 \text{ M}$  and  $0.1 \text{ M}$ ) do not significantly alter the overpotentials and performance of the cells, while high concentrations of polysulfide species increase the potentials up to  $0.8 \text{ V}$  vs.  $\text{Li}/\text{Li}^+$  (Figure 36d). With  $1.0 \text{ M}$  polysulfide solution, the cell showed signs of inner short circuits evident from the sharp decrease of potentials during stripping and deposition experiment ( $t=50\text{-}80 \text{ h}$ ,  $t>180 \text{ h}$ , etc.).

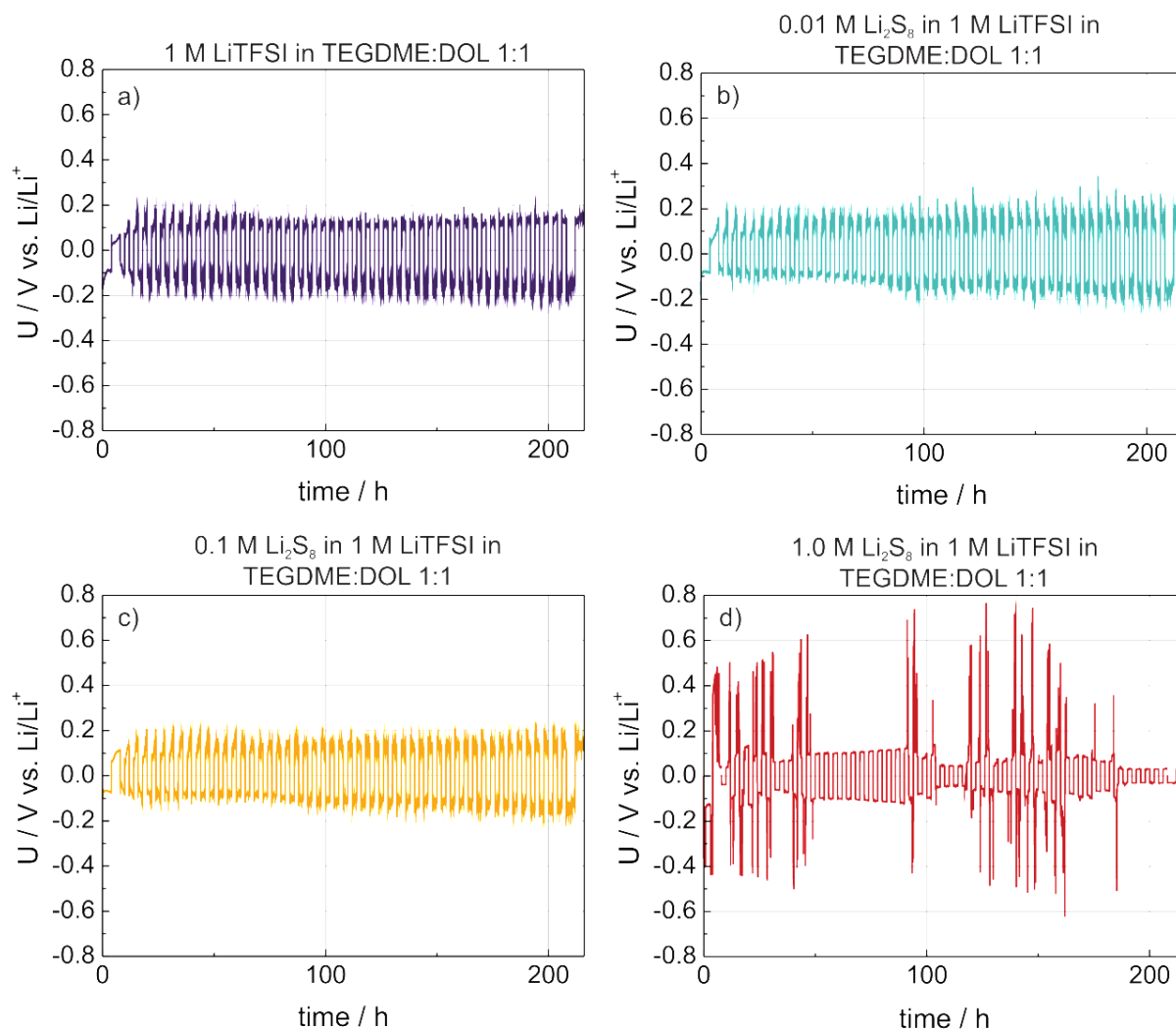


**Figure 36: Galvanostatic stripping and deposition study on Li | Li symmetric cells with various polysulfide concentrations**

After the stripping and deposition study, the impedance spectra of the Li | Li cells were measured again under the same settings (Figure 35b). After the current was stopped, the cell was left to rest for 15 minutes before the impedance measurement was started. The initial resistance was low and comparable to the spectra before cycling (insets on Figure 35b), while with time, the total resistance increased up to a few k $\Omega$  in size. Lower polysulfide concentrations produced results similar to each other, while the 1.0 M Li<sub>2</sub>S<sub>8</sub> concentration, as mentioned, resulted in internal short circuit, so the impedance spectra is not shown. The resistance contributions grew more complex with multiple arcs in the high frequency and low frequency region. The size increased up to a few k $\Omega$ . The electrolyte contribution capacitance increased, which merged the arcs together, suggesting severe electrolyte decomposition when in contact with Li.

From these results it is clear that the polysulfide's influence on Li metal anode performance does not have a large effect up to the concentration of 0.1 M Li<sub>2</sub>S<sub>8</sub>. When the concentration

was increased further (1.0 M  $\text{Li}_2\text{S}_8$  in 1 M LiTFSI TEGDME:DOL 1:1 (v:v)), the diffusion contribution for the fresh cell increased due to viscosity, while the cell performance during stripping and deposition of Li was poor. The overpotentials increased and internal short circuits were evident early during the measurement.

### b) Influence of Li metal on polysulfide species

The reverse case - Li metal influence on the sulfur species as catholyte soaked separator - was studied by measuring the impedance response of Li||Li cells with 0.1 M  $\text{Li}_2\text{S}_4$  solution in TEGDME:DOL (1:1) mixture without the added LiTFSI supporting salt. We suspected Li metal surface reacts with the polysulfides present in its vicinity, although this could not be detected in previously assembled cells with catholyte solutions (Figure 35). The reason lies in the fact that the impedance response is sensitive to the concentration of the  $\text{Li}^+$  ions, which are in excess due to the addition of a supporting salt in the electrolyte. By omitting this additive in the catholyte preparation, the reaction of Li metal with the lithium polysulfide species could be detected since it would also cause depletion of  $\text{Li}^+$  ions from the solution.

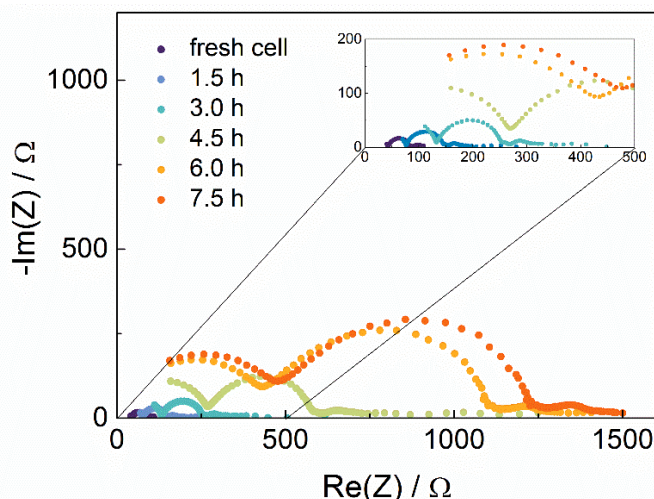


**Figure 37:** Li||Li impedance response evolution when no supporting  $\text{Li}^+$  salt was used for catholyte preparation (Celgard 2400 separator, 10  $\mu\text{L}$  of electrolyte, spectra measured with 10 mV amplitude from 1 MHz to 1 mHz except for the first spectrum where the measurement was done to 10 mHz).

As seen from Figure 37, a rapid increase in the resistive intercept is seen, which confirms the fast reaction of polysulfides with Li metal. Li reduces the polysulfides present to short-chained species, which are poorly soluble. Since they precipitate out of the solution, the concentration of dissolved  $\text{Li}^+$  ions decreases and impoverishes the electrolyte of its charge carriers, increasing its resistance.

The chemical reactivity of polysulfides with Li was evaluated with UV-vis spectroscopy. The electrodes were beforehand treated by electrochemical Li stripping/deposition to ensure a more active and larger surface area and to enhance the reaction with polysulfides. In one of the 2  $\text{cm}^2$  electrodes, an 8 mm hole was made prior to assembly. GF/D glassy fibre separator

was used and 200  $\mu\text{L}$  of 0.01 M  $\text{Li}_2\text{S}_4$  in TEGDME:DOL 1:1 (v:v). The measured UV-vis spectra is shown in Figure 38. The individual spectra were measured every 10 minutes and the total time elapsed from the cell assembly to the last measurement was 6 h.

The spectra show an initial rapid increase in reflectance at around 610 nm, which can be attributed to a rapid decrease of concentration of polysulfides present at the beginning. The change proceeds increasingly slower. The separator is discoloured from an initial green colour (Figure 38b) to almost colourless (Figure 38c), indicating a decrease in the concentration of dissolved polysulfides.

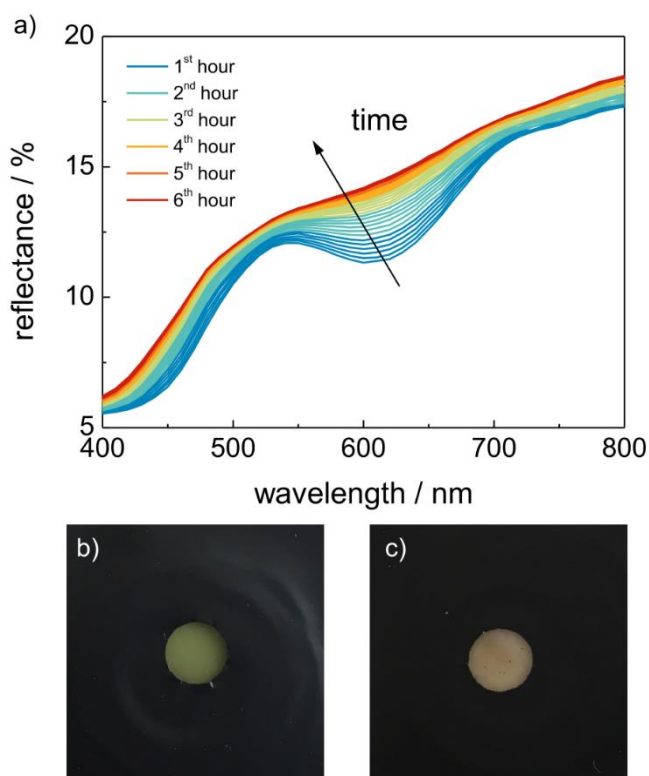
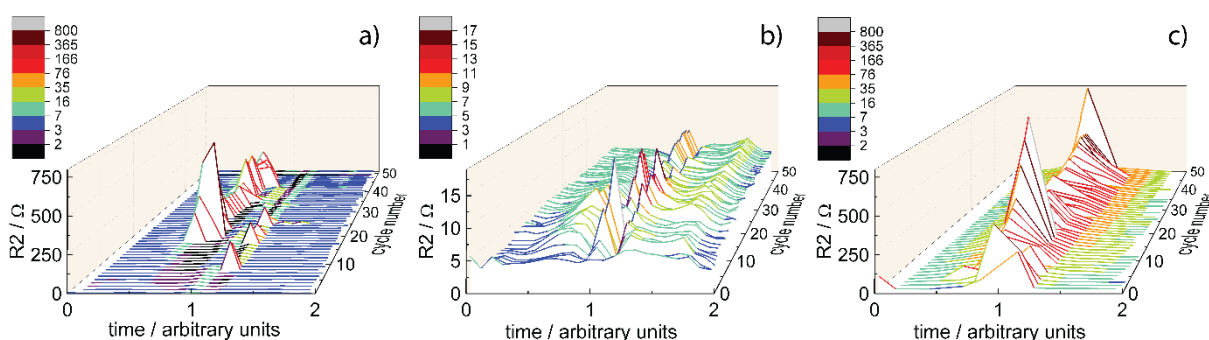


Figure 38: UV-vis spectra measured on Li||Li cell (a) and the corresponding discoloration of the separator from the initial state before measurements (b, green) to the final state (c, almost colourless).

#### 4.4 Cathode's contribution

R1 contribution to the spectra was attributed to the anode side of the battery cell as explained in section 4.2. Since the cathode part clearly dominated the low frequency region, we assigned the R3 part to the positive electrode. Assignment of the middle frequency contribution is a little more complex. From the symmetrical cells experiment through the first discharge it was determined that that signal is mixed with contributions from both sides (Figure 33). Nevertheless, since the anode surface drastically increases with further cycling, we speculate that the majority of the R2 response after the battery was discharged and charged a few times is cathode dominated.

The change of R2 contribution through cycling in different electrolytes is shown in Figure 39. Similar as on other 3D graphs shown before, the X-axis is for time, but the discharge and charge duration was both normalized. This means that with further cycling, although less capacity was reached, the data for discharge is always plotted between 0 and 1 and data for charge between 1 and 2. Y-axis and its scale for resistance is the same in the cases of sulfolane and ionic liquid based electrolytes, and reduced to smaller values for TEGDME. Blue colour significates low resistances and red higher resistances. Cycle number increases with going further into Z-axis. The response is different when changing the solvent. Contribution in TEGDME based electrolyte is maximum 15  $\Omega$  in size, while the resistances in the other two electrolytes reach over 500  $\Omega$ . Its shape through different DOD is also marginally different. With sulfolane and TEGDME electrolyte, it exhibits peaks in the middle of both discharge and charge, while the resistance for the [DEME][TFSI]:DOL electrolyte increases at the end of discharge.



**Figure 39:** R2 (middle frequency cathode resistance) change through 50 cycles at different DOD for three different electrolytes – a) 1 M LiTFSI in sulfolane:DOL 1:1, b) 1 M LiTFSI in TEGDME:DOL 2:1 and c) 1 M LiTFSI in [DEME][TFSI]:DOL 1:2.

The lowest frequency contribution is similar in size in all the electrolytes, reaching over a k $\Omega$  and dominating the internal impedance (Figure 40). With the ionic liquid electrolyte, the

values are incomplete since at the beginning and end of discharge, the spectra showed a more blocking response and the equivalent circuit chosen for the fit was not adequate.

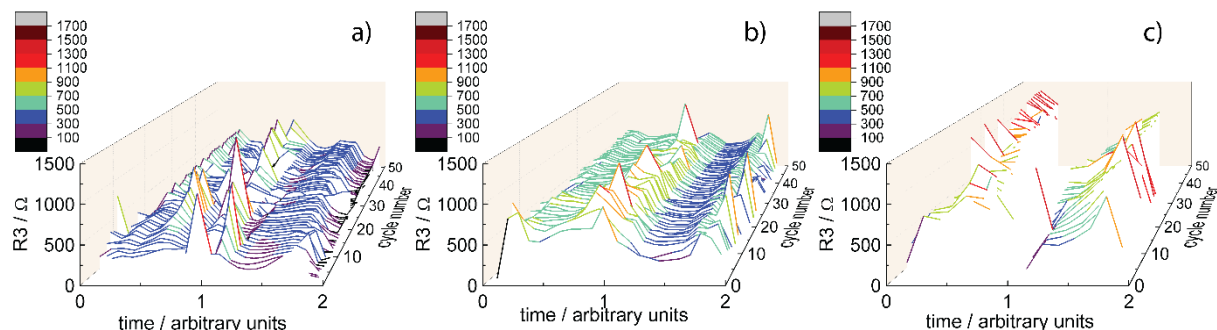


**Figure 40:** R3 (low frequency cathode resistance) change through 50 cycles at different DOD for three different electrolytes – a) 1 M LiTFSI in sulfolane:DOL 1:1, b) 1 M LiTFSI in TEGDME:DOL 2:1 and c) 1 M LiTFSI in [DEME][TFSI]:DOL 1:2.

Determination of the physical background of the analysed contributions cannot be made at this point, since, as stated in the beginning, the chosen equivalent circuit was arbitrary and used only to gather some general information of the evolution of impedance. From this experiment it is evident that the main contribution in the impedance response is of cathodic origin, which is why the main focus of further studies was on electrochemistry of polysulfides on carbon surfaces.

#### 4.4.1 Investigation of polysulfide electrochemistry on carbon surfaces

To understand the fundamental response of the polysulfide system, simpler geometry cells were employed. Instead of the porous carbon electrode, a planar 2 cm<sup>2</sup> glassy carbon disc (GC) was used and the Li metal was omitted. In turn, symmetrical cell with planar electrodes was constructed with the active species added as stoichiometric mixtures of different lengths of polysulfides dissolved in various concentrations in the 1 LiTFSI in TEGDME:DOL 1:1 (v:v) electrolyte. The concentrations ranged from 0.01 M Li<sub>2</sub>S<sub>x</sub> to 0.5 M Li<sub>2</sub>S<sub>x</sub>, while Li<sub>2</sub>S<sub>4</sub>, Li<sub>2</sub>S<sub>6</sub>, Li<sub>2</sub>S<sub>7</sub> and Li<sub>2</sub>S<sub>8</sub> polysulfides have been employed. Since polysulfides are known to disproportionate, the concentrations given should be considered as nominal. The properties of the so assembled GC-GC cells were investigated with impedance spectroscopy.<sup>104</sup>

The EIS response of a symmetrical system with planar electrodes is well known<sup>97</sup>, which could help us with identification of the physicochemical processes taking place in the system. In order to verify that polysulfides on the GC disc electrode follow the same mechanism as with the conventional electrodes, galvanostatic cycling was done on a GC||Li cell. The cell was

constructed with  $2 \text{ cm}^2$  electrodes, Celgard 2400 separator and  $10 \text{ }\mu\text{L}$  of  $0.1 \text{ M Li}_2\text{S}_4$  in  $1 \text{ M LiTFSI}$  in TEGDME:DOL 1:1 electrolyte. On Figure 41, the first three cycles at C/20 current are shown. The potential of the constructed cell was  $2.174 \text{ V}$  which corresponds to a partially discharged Li–S battery. The initial discharge reached  $230 \text{ mAh g}^{-1}$ , while the charge was over  $900 \text{ mAh g}^{-1}$  (Figure 41a). The second discharge reached below  $150 \text{ mAh g}^{-1}$  with slight overcharge. With subsequent cycling the capacity further decreased (Figure 41b).

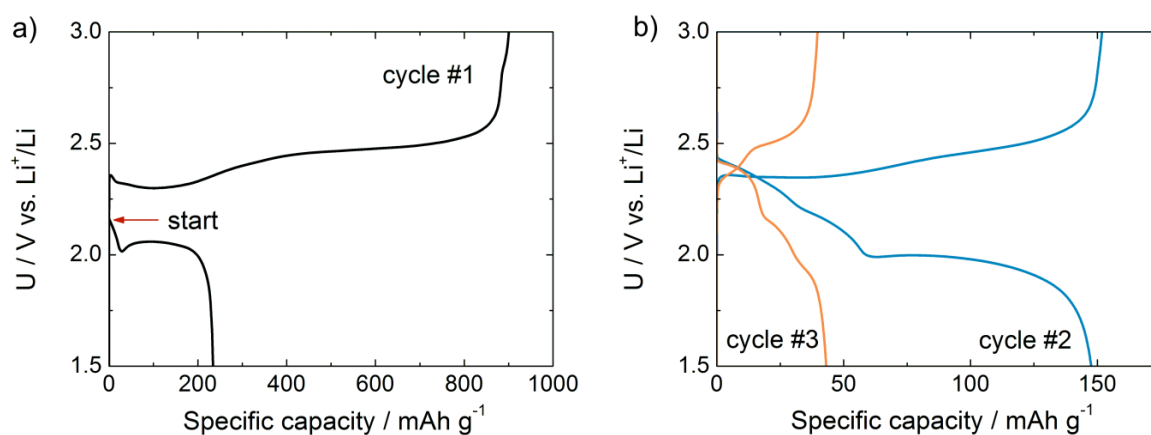


**Figure 41:** Galvanostatic cycling of a GC|Li battery cell at C/20 current.  $0.1 \text{ M Li}_2\text{S}_4$  in  $1 \text{ M LiTFSI}$  in TEGDME:DOL 1:1 (v:v) was employed and the capacity calculated with respect to the amount of sulfur added in the initial catholyte solution.

Although the capacity obtained from this type of cell was low and faded fast, the voltage profile exhibits the same features as typically seen in the conventional Li–S battery cell setup. It also shows the issues Li–S batteries are facing with the sulfur species only partially utilized due to their irreversible loss in the reaction with Li metal (Section 4.3.1). By employing a polysulfide blocking ceramic membrane the degree of that chemical reaction was controlled.<sup>78</sup> Commercially available glass-ceramic  $\text{Li}^+$  ion conductive membrane ( $\text{Li}_{1+x+y}\text{Al}_x\text{Ti}_2\text{-}_x\text{Si}_y\text{P}_{3-y}\text{O}_{12}$ ) was used (OHARA). The setup was similar as in the GC||Li cell described before, with the difference of the catholyte used ( $0.1 \text{ M Li}_2\text{S}_6$  in the base electrolyte).  $100 \text{ }\mu\text{L}$  of catholyte and  $100 \text{ }\mu\text{L}$  of base electrolyte were used to soak two GF/D glassy fibre separators on each side of the membrane. Intermittent galvanostatic discharge and charge measurements at C/50 with 1 h current steps interrupted with 25 min of open-circuit relaxations were done (Figure 42).

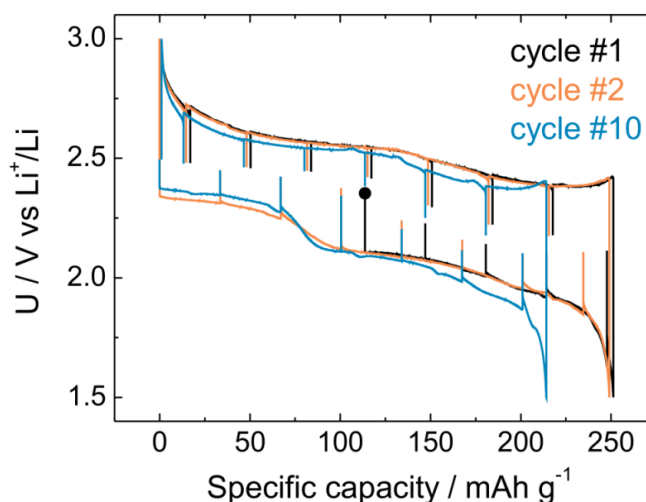


**Figure 42:** C/50 cycles with OCV relaxation periods measured on a GC|catholyte|ceramic membrane|electrolyte|Li cell. The capacity calculated is with respect to the amount of sulfur added with the initial catholyte.

The cycling behaviour obtained with that type of cell setup (Figure 42) was much more stable than the one without the ceramic membrane (Figure 41). The initial voltage was 2.354 V (Figure 42, black dot), slightly higher than before due to longer-chained polysulfides used. The first few cycles overlap with around 250  $\text{mAh g}^{-1}$  capacity reached. The 10<sup>th</sup> cycle shows reasonably good retention of the capacity.

This data showed that the planar glassy carbon electrodes and the cell geometry used can utilize about 15% of active mass present. All the typical features of the Li–S battery were observed and the cycling stability improved with a selective membrane. Based on Figure 41 and Figure 42 we concluded that GC electrodes adequately replace the porous electrodes used conventionally in the Li–S redox system.

#### ***a) GC||GC cell impedance response***

Figure 43 shows an example of a Randles-like system, which was measured for GC||GC symmetrical cell using a catholyte solution where  $\text{S}_8^{2-}$  and  $\text{S}_7^{2-}$  were dissolved (both in 0.05 M concentration). Other concentrations and polysulfides yielded similar results, although sometimes the contributions were merged and the magnitude of the arcs varied significantly. Here, the spectrum was measured in a wide frequency range from 1 MHz to 0.1 mHz. For fitting, the equivalent circuit as shown in Figure 43a was used. The double layer capacitance from the Randles circuit was exchanged for a constant phase element CPE. The fit is very good for the range used, although some of the lowest frequency points were excluded due to stability. Two Warburg features could be expected since two species were present, but only

one was detected (for the species with the higher value of  $R_w$ ). From the measurements presented, a speculation on which of the species that is, could not be made.

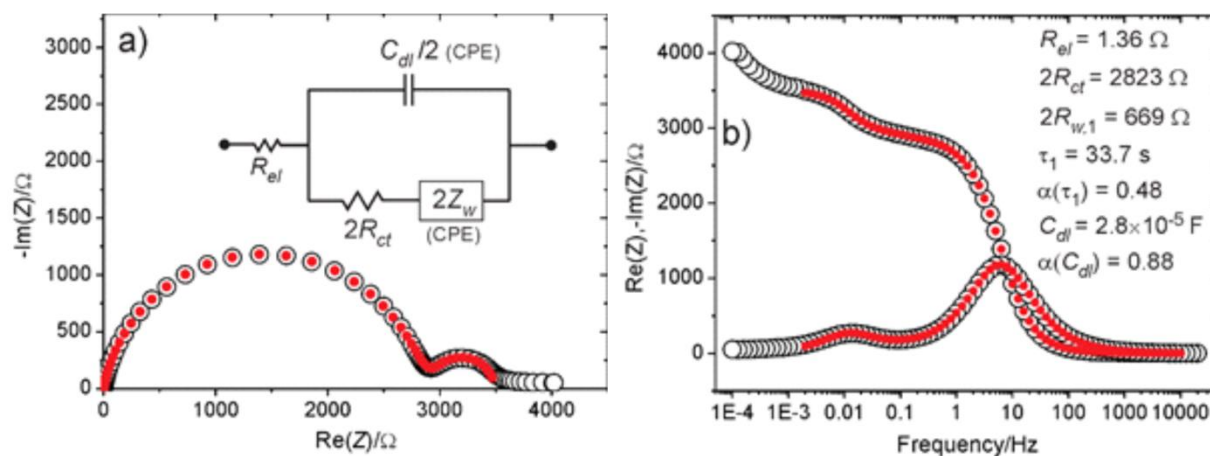


Figure 43: Nyquist (a) and Bode plots (b) of impedance response of a  $S_8^{2-}/S_7^{2-}$  redox pair (both in concentration of 0.05 M, Celgard 2400 separator was used and 10  $\mu\text{L}$  of electrolyte) in the frequency range of 1 MHz to 0.1 mHz in GC||GC cell (white circles). Fit using the equivalent circuit is shown in red. Adapted with permission from reference<sup>104</sup>. Copyright 2017 American Chemical Society.

On Figure 44,  $R_{ct}$  and  $i^0$  values for different solutions of polysulfides all of 0.1 molarity are plotted. The error bars correspond to the highest and lowest values measured for each system. In the whole polysulfide range tested, the values are in the similar order of magnitude, which suggests that the kinetics for the various steps during polysulfide reduction and oxidation are comparable and there is no strict rate-determining step.

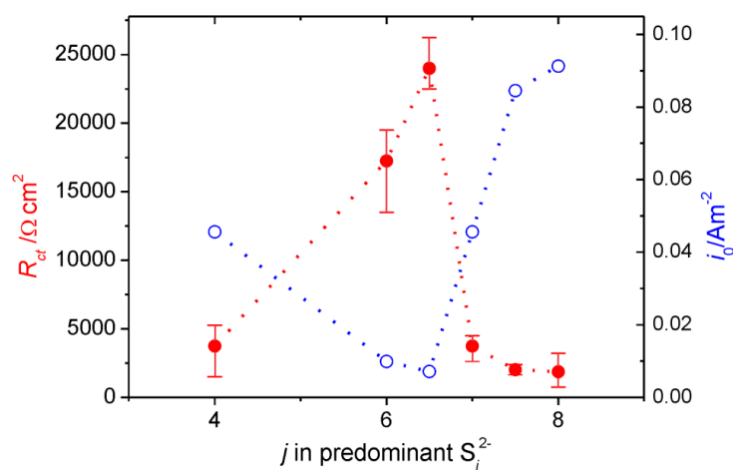


Figure 44:  $R_{ct}$  and  $i^0$  dependence upon the predominant polysulfide in the system. Each point is an average of at least 10 measurements. Reprinted with permission from reference<sup>104</sup>. Copyright 2017 American Chemical Society.

### b) Disproportionation of polysulfides

When doing successive measurements on the same cells, a variation in the magnitude of the charge transfer resistances could be seen, sometimes for even a factor of 2. Li polysulfides tend to be unstable in solutions and are involved in series of coupled equilibria<sup>124,125</sup>, so we attributed this drift to disproportionation of polysulfides to different chain lengths. The hypothesis was tested with *operando* UV-vis experiment (Figure 45), which could in principle give information about the stoichiometry of polysulfides soaking the separator.<sup>95</sup>

Pt|Pt cell was assembled with a circular hole in one of the electrodes. This hole was also the reason for exchanging the glassy carbon electrodes for platinum ones. The platinum electrodes impedance response was tested to be similar to glassy carbon. Thin glassy fibre separator (GF/A) was used and 100  $\mu\text{L}$  of 0.01 M  $\text{Li}_2\text{S}_4$  in TEGDME:DOL 1:1 (v:v) catholyte. The cell was placed in the UV-vis spectrophotometer, where a spectrum was measured every 80 minutes. In the same time interval, an impedance spectrum from 1 MHz to 1 mHz (10 mV amplitude) was measured *operando*. The experiment lasted approximately 95 hours.

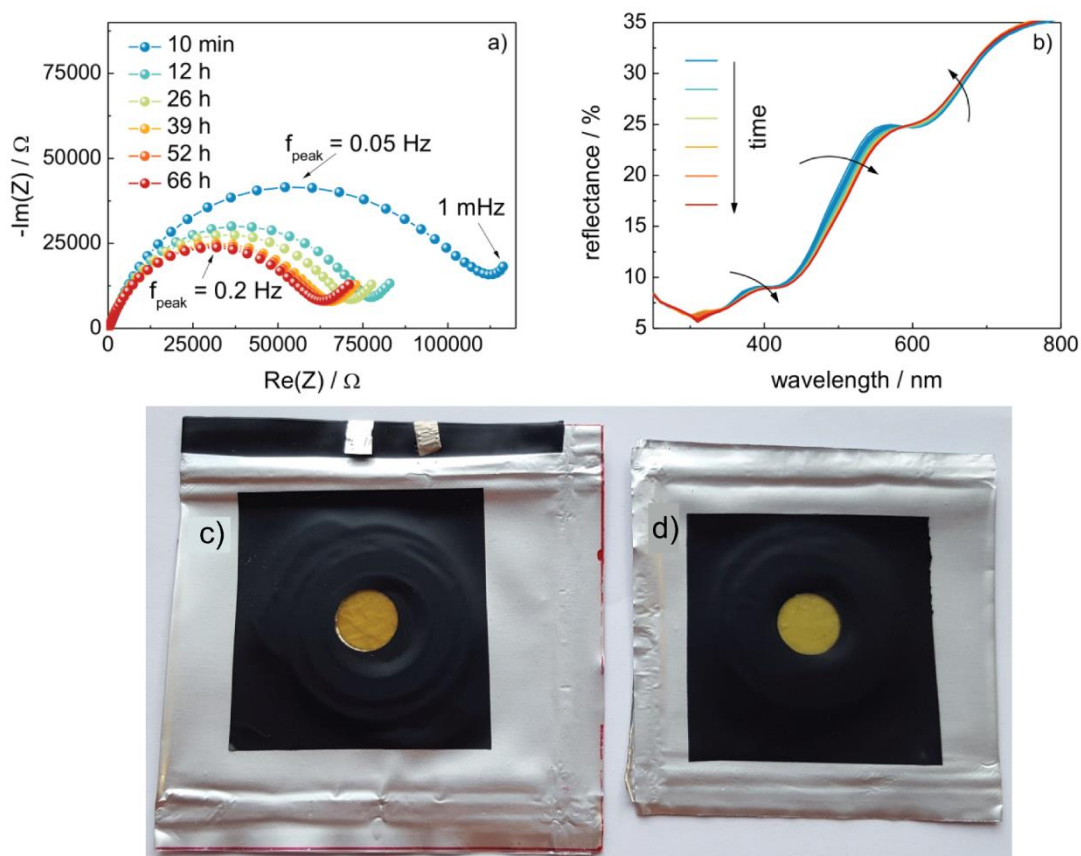


Figure 45: a) Drift of EIS spectra of a Pt|Pt cell containing 0.01 M  $\text{Li}_2\text{S}_4$  in TEGDME:DOL 1:1 (v:v) measured from 1 MHz to 1 mHz b) drift in UV-vis spectra measured every 80 minutes reflecting a change of concentration of species, c) colour of the separator 95 h after cell assembly, d) a freshly prepared cell with the same electrolyte composition.

No global net change of the oxidation state was done during the measurement, so the same manner of spectra analysis as on operating batteries could not be employed. We observed an increase in reflectance above 600 nm and a decrease at shorter wavelengths (Figure 45b, arrows). This was attributed to a difference in the length of polysulfide chain, since a change only in concentration would manifest as a decrease (or increase) in the whole wavelength range.<sup>94</sup>

The colour of the soaked separator changed from green (Figure 45d) to orange (Figure 45c), which stands for elongation of chain length. Since the net oxidation state remained the same, shorter polysulfides must also have been formed, although they have not been detected. Shortening the chain length also leads to decreased solubility, so it is possible they precipitated out of the solution. One could argue that this phenomenon could be detected through an increase in resistance, but it is also possible that the material precipitated inside the separator, where greater surface area is available compared to the planar glassy carbon electrode (2 cm<sup>2</sup>).

The variation in the  $R_{ct}$  as seen on Figure 45a was sometimes to smaller resistances and sometimes to greater ones and in a few cases also oscillated (Figure 46a). An example of spectra where the resistance first increased and then decreased is shown on Figure 46b. Interestingly, the drift not only depended upon the type of polysulfides, but also on their concentration. That can be seen from the comparison of data for 0.1 M  $\text{Li}_2\text{S}_4$  (Figure 46a - red) and 0.01 M  $\text{Li}_2\text{S}_4$  (Figure 45a).

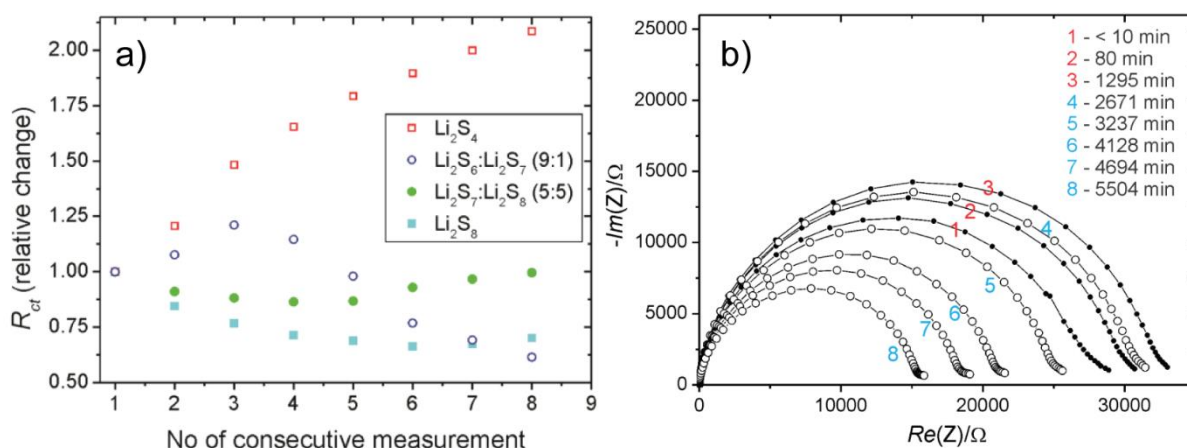


Figure 46: a) Relative change of the charge transfer resistance for selected polysulfides and polysulfide pairs (total nominal concentration of 0.1 M) during EIS measurements on GC|GC cells, b) time evolution of the impedance spectra of the 0.09 M  $\text{Li}_2\text{S}_6$  / 0.01 M  $\text{Li}_2\text{S}_7$  pair in 1 M LiTFSI in TEGDME:DOL 1:1 (v:v).

An investigation into disproportionation was made by preparing catholyte solutions of three different molar ratios of  $\text{S}_7^{2-}$  and  $\text{S}_8^{2-}$  (10:90, 50:50, 90:10) in the supporting electrolyte and measuring the impedance spectra of GC|GC cells using 10  $\mu\text{L}$  of the solution and Celgard

2400 separator. The  $R_{ct}$  value was smallest for the case with the 50:50 ratio. This is explained by Equation 14, which states, that the  $i^0$  depends upon the product of concentrations of both the “Red” and “Ox” species. If the two exponents,  $p$  and  $q$ , in the equation are equal and the transfer coefficient is 0.5, the minimum is exactly at 50:50 ratio, while changing them introduces asymmetry in the curve of dependence of  $R_{ct}$  on the molar ratio (Figure 47a). For the tested mixtures the factors  $p$  and  $q$  are 3.5 and 4, respectively (Equation 15), although the measured points do not fall on the curve calculated for those values (Figure 47a – red curve).

$$I_0 = zFAk^0[(c_{Ox}^0)^p]^{1-\alpha}[(c_{Red}^0)^q]^\alpha \quad (14)$$

The discrepancies were attributed to disproportionation. If completely new species were formed following Equation 16 and the conversion of  $S_7^{2-}$  to  $S_6^{2-}$  was 100%, the redox reaction which needs to be taken into account is a sum of the two reactions (Equation 17). That changes the stoichiometric factors and the curve dependence of  $R_{ct}$  (Figure 47a – blue curve). If comparing the two curves, one could naturally guess that the measured points are a compromise between the limiting cases proposed. Several different disproportionation degrees were investigated and are shown on Figure 47b.



Although this scheme is an approximation, since several different disproportionation reactions could take place, it can still be used to evaluate the unusual behaviour seen as oscillating resistances (Figure 46). At various initial concentrations of the species (as percentage of oxidize species in the mixture), the change with progressive disproportionation was calculated (Figure 47c).

A way of determination of the prevailing polysulfide reaction in a given system was sought for by an approach similar to one proposed for a general system of chemical and electrochemical reactions.<sup>126</sup> Cells which contained  $Li_2S_4$  in the supporting electrolyte in a range of concentrations from 0.1 M to 0.001 M were prepared. If the  $S_4^{2-}$  species disproportionated to  $S_2^{2-}$  and  $S_6^{2-}$ , two electrochemical reactions were assumed based on the species produced (Equations 18 and 19).



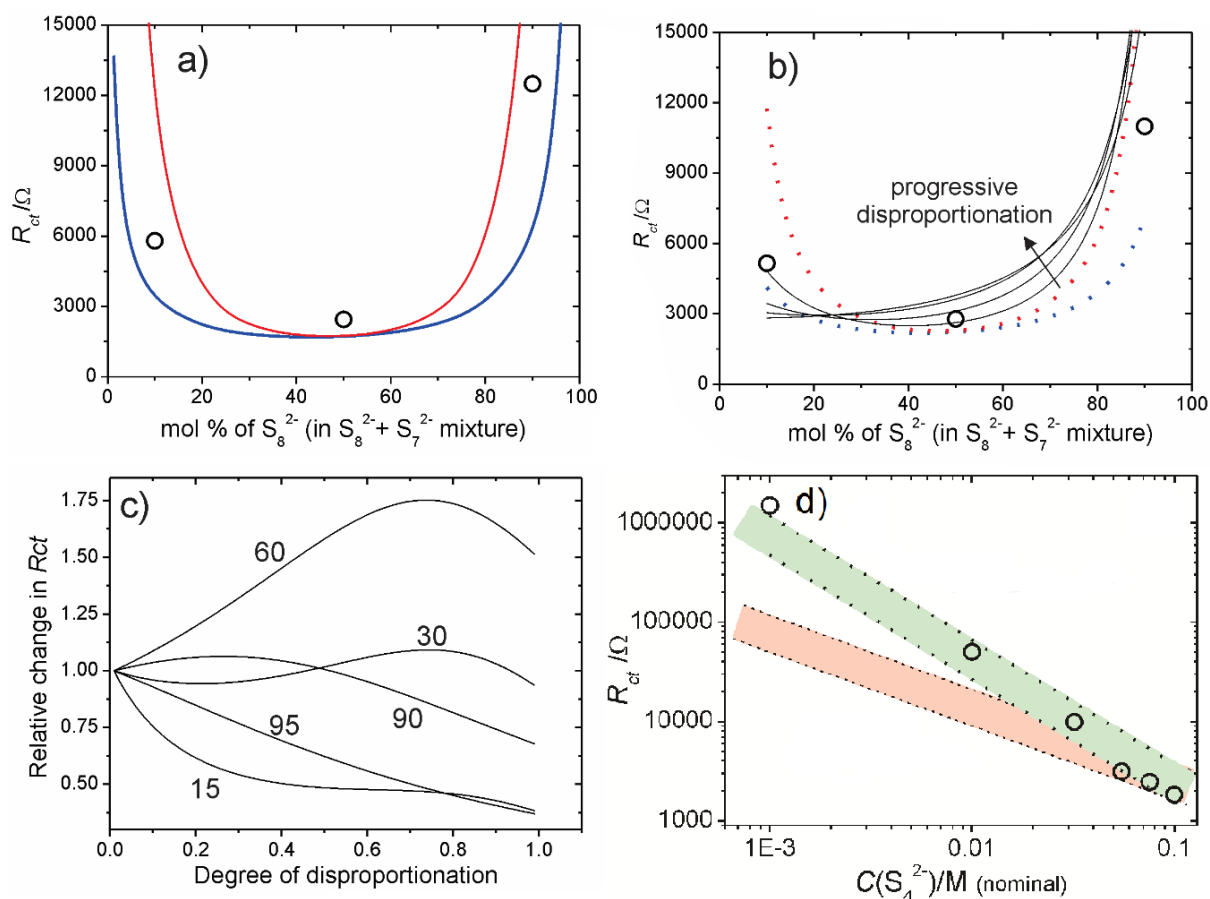


Figure 47: a) Experimental values of  $R_{ct}$  (points) at different molar ratios of  $S_7^{2-}$  and  $S_8^{2-}$ . Simulated curves for the reaction given by Equation 15 (red) and Equation 18 (blue). b) Different degrees of disproportionation of  $S_7^{2-}$  (20% to 80% in steps of 20%). c)  $R_{ct}$  variation with degree of disproportionation. The numbers refer to the percentage of the oxidized form in the initial mixture. d)  $R_{ct}$  dependence on the initial concentration of the polysulfide ( $S_4^{2-}$ , circles). Fitting with two curves as explained in the text. Adapted with permission from reference<sup>104</sup>. Copyright 2017 American Chemical Society.

The two reactions would result in two different trends of  $R_{ct}$  dependence upon the concentration, which is due to different stoichiometry and  $p$  and  $q$  values. The measured values of  $R_{ct}$  are shown as circles on Figure 47d. Although the concentration decreases by two orders of magnitude, the value for  $R_{ct}$  increases three times. The average value of  $p$  and  $q$  determines the slope, while the degree of disproportionation shifts the curves vertically (disproportionation between 10% and 90% is shown as shaded areas). Low  $p$  and  $q$  values (Equation 18) correspond to a low slope (Figure 47d – pink) and higher values in Equation 19 to a steeper one (Figure 47d – green). The measured points fall close to the predicted slope using Equation 18. Although this is not considered proof that this is a prevailing mechanism, it certainly shows that the reaction pathway does not follow the one in Equation 18.

### c) Polysulfide diffusion contribution

Impedance spectra shape for the  $S_4^{2-}$  species proved useful for diffusion contribution determination, since the low frequency arc was not superimposed with the charge transfer contribution and because it was at high enough frequencies, where spectra could be measured fast enough to exclude the change due to disproportionation. The arc was extracted, fitted and the  $R_w$  value obtained at different concentration of species. The results are shown on Figure 48. Although scattering of the data is significant, the values roughly follow the model prediction. Problems we were facing in this case, besides the drift of the system, are also errors due to the use of concentrations instead of activities and because the  $R_{ct}$  contribution prevailed over the  $R_w$  at low concentrations and the values could not be extracted.

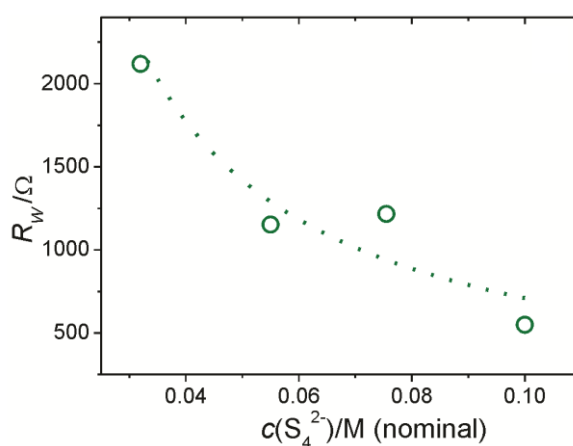


Figure 48: Diffusion resistance dependence on the concentration of polysulfides ( $S_4^{2-}$ ). Concentrations to 0.032 M are displayed, since determination became unreliable due to the contribution of  $R_{ct}$  prevailing. Adapted with permission from reference <sup>104</sup>. Copyright 2017 American Chemical Society.

For other species, an attempt to extract the same data was made, but failed in multiple cases, either due to the diffusion arc being too small, too scattered or because it appeared at frequencies lower than 0.1 mHz, which was the limit of our measurements. An example of those measurements is shown on Figure 49. An important reason for the scattering of the low frequency points is due to the change in the high frequency charge transfer contribution and the length of the measurements.

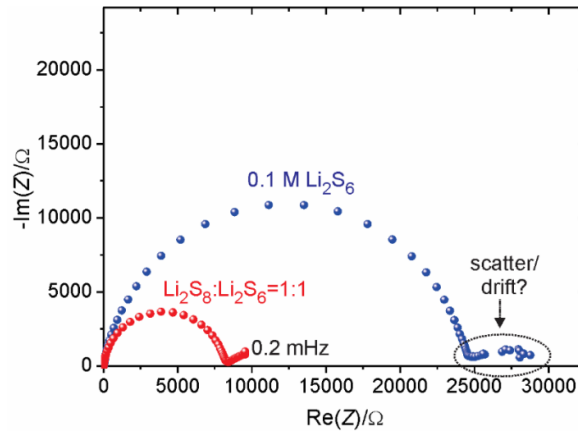


Figure 49: Limitations and instability issues in measuring the diffusional arc.

Since a typical relaxation time for diffusion of polysulfide species is long, the measurements had to be done to low frequencies. This condition in itself proves a challenge due to the drift of any origin, which includes a systematical error in the measurement. For accurate measurements, temperature had to be regulated and in some cases the number of measured frequencies reduced to shorten the measurement time.

The pore volume, geometry and connectivity should also be taken into consideration when determining the diffusion coefficients for our system, since the porosity and tortuosity have a strong impact on it (a rough estimate in Equation 20,  $\varepsilon$  – porosity,  $\tau$  – tortuosity<sup>127</sup>). The values for porosity and tortuosity for Celgard 2400 separator are 0.32–0.37 and 6.0–7.3, respectively, which means, that the effective diffusion coefficient when employing it would be between 16 to 23 times smaller than without it.

$$D_{eff} = \frac{\varepsilon}{\tau} D \quad (20)$$

This effect was investigated by replacing the Celgard 2400 separator with a thick glassy fibre separator or by removing the separator completely and employing a custom made Swagelok cell with a Teflon spacer between the electrodes. For that case, smaller glassy carbon discs ( $\varnothing$  12 mm), that could fit into a commonly used Swagelok cell were employed. In that order the distance between the electrodes also increased from 25  $\mu\text{m}$  for the Celgard separator, 670  $\mu\text{m}$  for the glassy fibre one and 1 mm for no separator. Values for the diffusion coefficient and the diffusion length are collected in Table 7. The values increase when going from the Celgard separator to none at all. The case without a separator is probably close to the maximum diffusion layer thickness possible, since there is no porous restriction. Since applications in batteries would always include some type of porous separator, those values are a reference point for the limit cases. The diffusion coefficient values were calculated as explained in reference<sup>104</sup> according to the fit parameters obtained with fitting of impedance spectra with the Randles circuit in Zview program.

**Table 7: Diffusion parameters for GC || GC cells with different types of separator. 0.05 M  $\text{Li}_2\text{S}_6$  0.05 M  $\text{Li}_2\text{S}_8$  in 1 M LiTFSI in TEGDME:DOL 1:1 (v:v) was used. Reprinted with permission from reference<sup>104</sup>. Copyright 2017 American Chemical Society.**

parameter	Celgard 2400 separator	glassy fibre separator	no separator
$D_i$ ( $\text{m}^2 \text{s}^{-1}$ )	$2.6 \cdot 10^{-13}$	$1.7 \cdot 10^{-12}$	$(1.30-1.84) \cdot 10^{-11}$
L (m)	$2.9 \cdot 10^{-6}$	$42 \cdot 10^{-6}$	$(189-220) \cdot 10^{-6}$

This study enabled us to gain a thorough understanding of the charge transfer reaction process of polysulfide species on carbon electrode surfaces. This meant that we could predict how this reaction takes place on more conventional porous carbon electrodes. Furthermore, the extent and importance of the polysulfide disproportionation reaction was elucidated and this knowledge employed in understanding of other processes taking place during discharge of the Li–S battery.

#### 4.4.2 Porous carbon cathode impedance

Since the  $R_{CT}$  contribution is linearly dependent upon the available electrode surface area, the contribution significantly reduces when exchanging planar glassy carbon electrodes with high-surface area porous electrodes. To elucidate this phenomenon, impedance response of symmetrical cells built using porous carbon cathodes (ENSACO 350G), carbon felt electrodes (H14), and glassy carbon electrodes (GC) were compared (Figure 48).

These cathodes showed a large difference in the available surface area (Figure 48c-e), which ranged from  $1 \text{ cm}^2$  to  $15 \text{ cm}^2$  and  $1000 \text{ cm}^2$  for GC, H14 and ENSACO 350G, respectively. With the increase in the electrode surface area, the charge transfer resistance, as expected, significantly decreased (Figure 48a,b). The determination of the origin of this contribution is further supported by the values for  $C_{CT}$  (double layer capacity) and constant peak frequency (Figure 48f). These results strongly confirm that when it comes to the charge transfer reaction impedance contribution of polysulfides on porous carbon surfaces, the feature consists of a small high frequency arc with a peak frequency around 10 Hz.

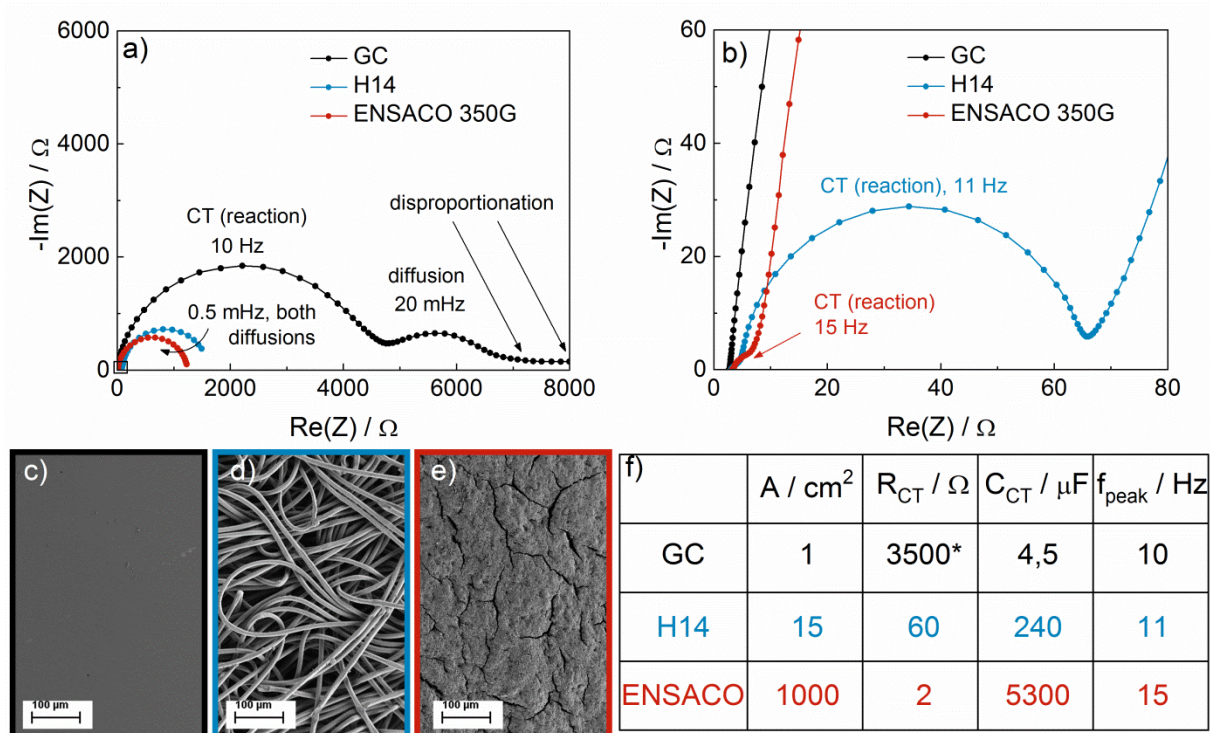


Figure 50: a) Impedance spectra of symmetrical carbon cells with 0.1 M Li<sub>2</sub>S<sub>4</sub> in 1 M LiTFSI TEGDME:DOL 1:1 (v:v) at OCV between 1 MHz and 0.1 mHz. b) magnification of the high frequency part of the spectra, c) SEM image of the GC electrode, d) SEM image of the H14 carbon felt electrode, e) SEM image of the ENSACO 350G porous electrode, f) values for the electrode specific surface areas and reaction contribution parameters. \*value for R<sub>CT</sub> for GC electrode is an average due to large disproportionation change.

The fact that the values of R<sub>CT</sub> for large surface area porous cathodes are very small is paramount for understanding the response of practical Li–S battery cells. The R<sub>CT</sub> contribution is practically negligible in comparison to the low frequency arc originating in the complex diffusion of polysulfides inside both the carbon electrode and separator pores. The total impedance of porous cathode cells is therefore almost completely determined by diffusional processes, with the charge transfer reaction contribution contributing only a very small fraction of the total impedance value (<1 %).

The question that remains is how this changes with discharging the Li–S battery and the formation of an insulating Li<sub>2</sub>S film on the surface of the carbon cathode. Based on the experiments conducted so far, one can assume that even if a large percent of the surface is covered and unavailable for further reaction (for example 95%), the charge transfer impedance would still be smaller than the diffusional impedance. This is further exacerbated by the fact that the charge transfer contribution is governed by the Butler-Volmer relationship and is further reduced when the cell is operational and far from OCV conditions. For conventional cells, their operation will therefore be controlled by mass transfer complications rather than by the redox reaction.

Further experiments were employed by varying the degree of discharge and following the change in the impedance contributions. Most of the work was again done on simplified

geometry cells. The reason why simplification of the cell geometry is needed is again in the size comparison shown on Figure 48. The small value of  $R_{CT}$  makes the study of the insulating film deposition on the porous electrode surface very problematic. It is very difficult if not impossible to extract such small values ( $2 \Omega$ ) from the much larger impedance features of full cells in the same frequency range.

#### 4.4.3 Cathode impedance change with SOC and the origin of Li–S capacity limitation

Conventional cell's impedance change during discharge (Figure 52, experiment explained in section 4) was compared to the change seen in simpler geometry electrodes (glassy carbon electrode and carbon felt electrode). The cells were discharged at a rate of C/50 (GC || Li) or C/20 (H14 || Li).

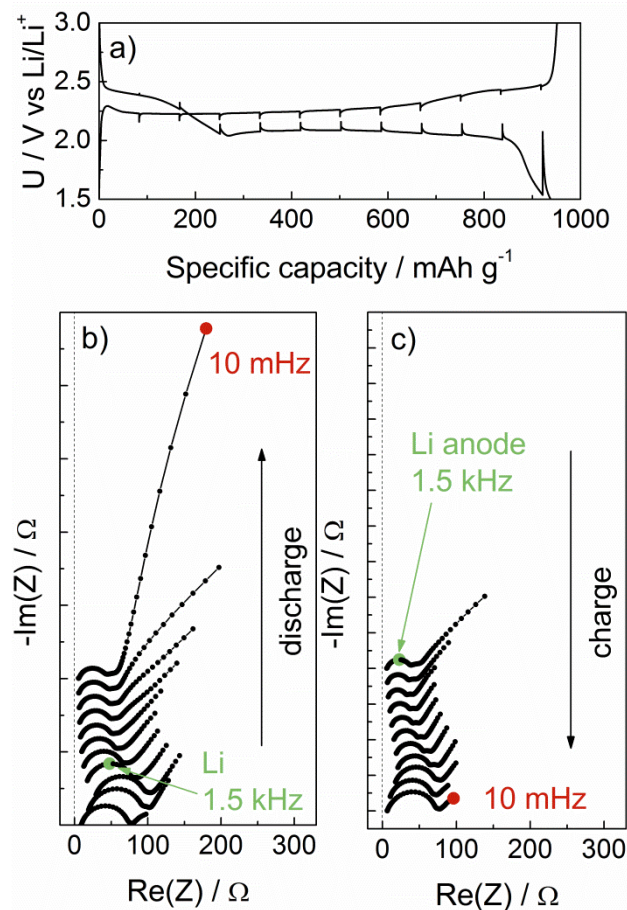


Figure 51: a) discharge and charge voltage profile during impedance spectra measurements on a conventional cell assembled with 1 M LITFSI in TEGDME:DOL 2:1 electrolyte (60  $\mu\text{L}/\text{mg S}$ ) and glassy fibre separator; b) impedance spectra change during the first discharge and c) charge. The electrode size was  $1.5 \text{ cm}^2$ .

The results (Figure 52) show that the charge transfer contribution increases with DOD, regardless of the electrode type employed. With GC electrode, the increase of  $R_{CT}$  was about

15-fold, while for the carbon felt 130-fold. The generally accepted origin of this increase is the passivation of the available surface area of the electrode<sup>75,82,84,128–140</sup>. However, the  $R_{CT}$  increase cannot be attributed solely to the surface area decrease, since the carbon felt surface area is 15-times larger, while the corresponding capacity increase was only by a factor of 2. There must therefore be another significant contribution to the increase of  $R_{CT}$ . An obvious source is the depletion of the remaining polysulfide species due to solid phase formation. The change in the peak frequency of the arc is also consistent with these predictions.

Another interesting detail gathered from this experiment is that the total impedance value (i.e. impedance modulus), is larger than the impedance contributions measured in the chosen frequency range. This suggests that diffusional contributions are significant not only in the porous cathode setup but in the simplified geometry as well. The Li anode contribution can be seen as a small arc at high frequencies and is shown in insets of Figure 52b and d.

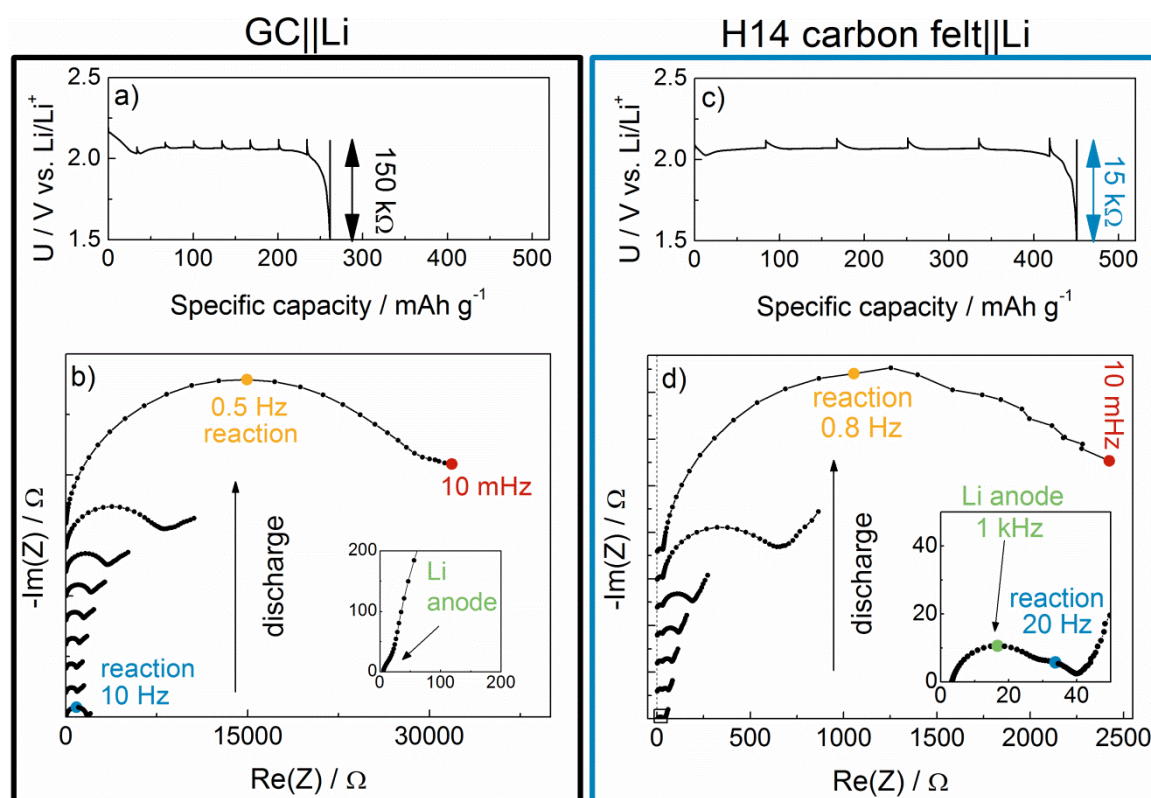
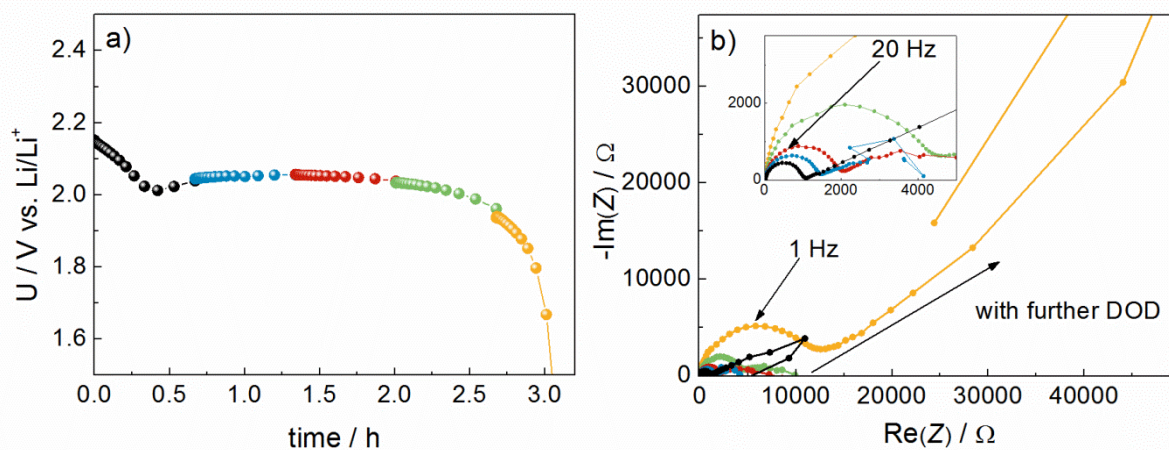


Figure 52: a) and c): Discharge voltage profiles of GC||Li and H14||Li cells assembled with a Celgard separator and  $10\ \mu L$  or  $40\ \mu L$  of  $0.1\ M\ Li_2S_4$  in  $1\ M\ LiTFSI$  in TEGDME:DOL 1:1 (v:v), respectively. b) and d): Impedance spectra at various DOD after 15 minutes of relaxation. Inset show the Li anode contribution.

Verification of these OCV-based impedance measurements was done through a dynamic impedance experiment (Figure 53). A GC||Li cell with an identical setup was discharged at  $C/20$  current, whose signal was superimposed with an alternating current of  $C/200$  amplitude.

The impedance spectra showed an arc in the range of a few k $\Omega$  to over 10 k $\Omega$ , supporting the results based on OCV impedance measurement. Unfortunately, due to the severe drift of the system under the conditions of cell operation, low frequency measurements were not stable enough to gather any reliable information from them.



**Figure 53:** a) Voltage vs. time dependence during dynamic impedance measurement on a GC||Li cell with 10  $\mu\text{L}$  of 0.1 M  $\text{Li}_2\text{S}_4$  in 1 M LiTFSI in TEGDME:DOL 1:1 (v:v). Current was C/20, alternating current amplitude C/200, frequency range between 1 MHz to 2 mHz. b) Corresponding impedance spectra during discharge.

Another technique which gives insight into impedance evolution is alternating current voltammetry (ACV), which allowed closer monitoring of the change in resistance size through discharge of the battery cell. Figure 54 shows the change in the excitation potential signal and the current response of the system used during discharging a GC||Li cell in ACV mode. Alternating current voltammetry measurement was conducted in the voltage window between 2.3 V and 1.5 V vs.  $\text{Li}/\text{Li}^+$  at a scan rate of 0.05 mV/s and frequency of 5 mHz. Amplitude of oscillation in the current signal was extracted from the ACV measurement and is plotted in Figure 54b. The magnitude is reversely proportional to the system resistance and decreases by a factor of 40 from the beginning to the end of the measurement. This seems in good agreement with the differences observed in impedance and galvanostatic measurements. Moreover, this measurement detects the variation of the reaction resistances of various lengths of polysulfide species detected earlier and shown in Figure 44, showing as a “sinusoidal” wave at potentials between ca. 2.31 and 2.02 V vs.  $\text{Li}/\text{Li}^+$ .

Of special interest, however, is the part of the curve directly afterwards, where a sudden increase in the  $I_{ac}$  magnitude is detected, followed by a steep decrease until the end of discharge. This variation is attributed to the oversaturation of the catholyte solution and subsequent nucleation and onset of film deposition. As a whole, the use of ACV allows precise detection of film formation and, also a quantitative evaluation of the resistance changes during the potential sweep of interest.

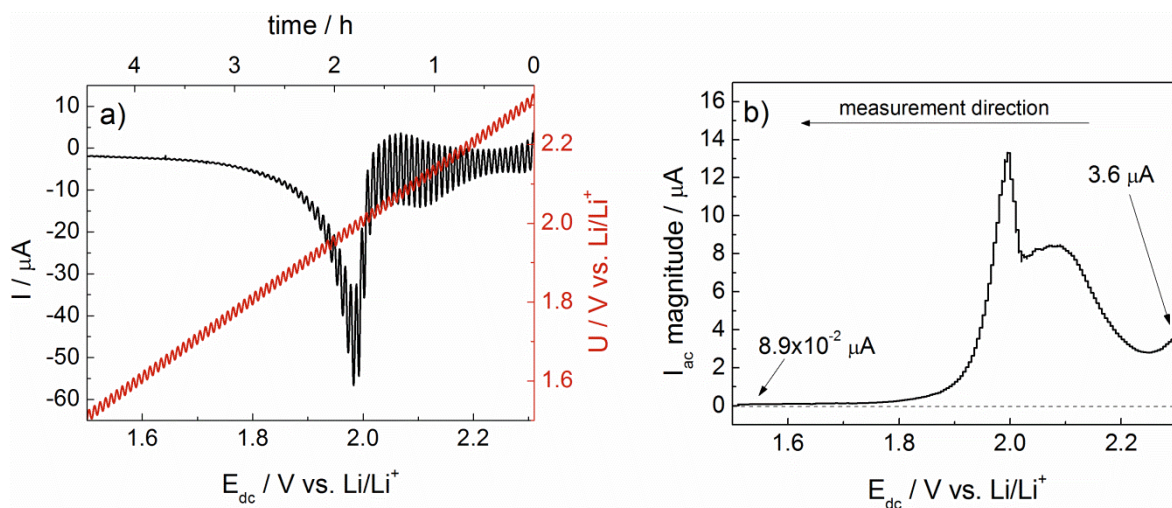


Figure 54: a) Total current transient for the ACV measurement and the excitation potential signal as a function of time and  $E_{\text{dc}}$  component b) magnitude of the ac component of the current. The dc part of the potential was scanned with  $0.05 \text{ mV/s}$  to  $1.5 \text{ V}$  versus  $\text{Li/Li}^+$  starting at the OCV potential of  $2.31 \text{ V}$  vs.  $\text{Li/Li}^+$ , the amplitude of the superimposed voltage sinusoidal signal was  $10 \text{ mV}$  (rms) and frequency  $5 \text{ mHz}$ .

In the measurements presented, the formation of poorly soluble species during discharge affects the impedance of the cathode, although determination to which extent this is due to surface passivation or due to reduction of polysulfide species concentration was not possible. Under the studied conditions, the film seems to cover parts of the available surface, while the uncovered surface remains unchanged. This is clear from the fact that impedance spectra shape remains the same in all studied conditions, while the value of  $R_{\text{CT}}$  changes due to surface blockage.

In order to study the surface film creation, several cells were discharged under “harsh” conditions with the intent to form a thick layer of the deposit. This was done by discharging cells  $\text{GC}||\text{Li}$  cells with a Celgard separator and  $10 \mu\text{L}$  of  $0.5 \text{ M Li}_2\text{S}_4$  in the supporting electrolyte at  $C/200$  to  $2.0 \text{ V}$  vs.  $\text{Li/Li}^+$ . This potential was then held for 24 hours. (Figure 55a)

The thickness of the  $\text{Li}_2\text{S}$  deposit was confirmed by FIB-SEM measurement (Figure 55b,c) to be in the order of  $1 \mu\text{m}$ . This measured thickness, however, does not coincide with the 2D layer deposition mechanism<sup>75,128,129,138</sup>, since this theory predicts uniform growth until the maximum thickness still enabling electron tunnelling is reached (estimated to be  $10 \text{ nm}$ ). We propose that  $\text{Li}_2\text{S}$  deposition proceeds by a complex growth mechanism, where nucleuses are formed by direct electrochemical reduction of soluble polysulfides, while consequent growth is determined by disproportionation reaction of soluble polysulfide species<sup>104,141</sup>, which act as redox mediators and produce a 3D film growth.

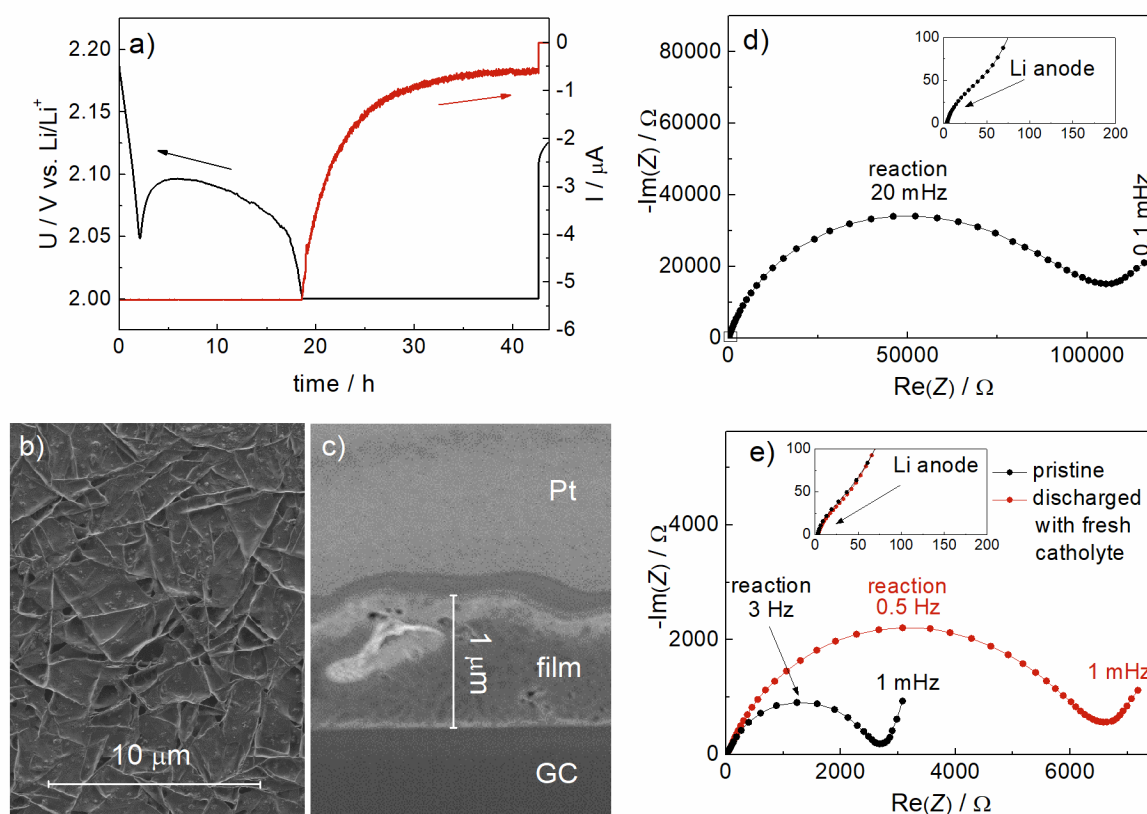


Figure 55: Discharge of a GC | Li cell with 10  $\mu\text{L}$  of 0.5 M  $\text{Li}_2\text{S}_4$  catholyte solution in the supporting electrolyte. a) Potential and current transient during deposition of  $\text{Li}_2\text{S}$ . b) SEM image of the film deposit on the GC electrode formed by the procedure in a). c) cross-section of the deposit on the GC electrode showing a porous and thick film in the size order of 1  $\mu\text{m}$ . d) Impedance spectrum of a GC | Li cell after film deposition e) Comparison of GC | Li cell impedance before film deposition (fresh) and after film deposition, when fresh catholyte solution (additional 10  $\mu\text{L}$  of 0.5 M  $\text{Li}_2\text{S}_4$  catholyte solution) was added.

Since the formed deposit is very thick, one could assume it would block any of the remaining polysulfide's redox reactions. Unfortunately, by forming the thick layer of film, we also depleted the polysulfide concentration in the electrolyte, which means that this assumption is hard to check in the same battery cell. In order to check whether the surface passivation or the polysulfide species depletion was the cause for the increase in the impedance reaction contribution (Figure 55d), we opened a cell, where a thick film was deposited, and added fresh catholyte solution. Impedance spectra measurement of this cell revealed a significant decrease in the  $R_{CT}$  contribution's size (Figure 55e). These results strongly support the conclusion that the effect of surface passivation is much smaller than the consequences of polysulfide depletion.

Unfortunately, from this experiment alone and with the knowledge of the change in impedance spectra due to disproportionation reactions (Figure 46, Figure 47), one cannot speculate on the extent of the film coverage on the glassy carbon electrode. A similar experiment was repeated on a carbon felt electrode, where an increase corresponding to 85% surface coverage was detected with the difference between the fresh electrode

impedance and the impedance of the cell with deposited film and the addition of the fresh catholyte solution.

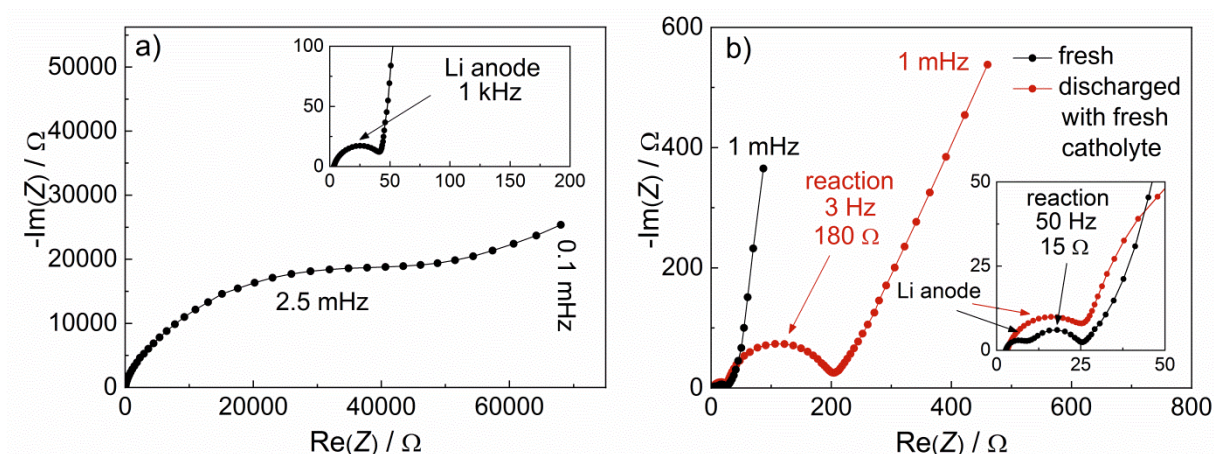


Figure 56: Impedance spectra of fresh and discharged H14 | Li cell assembled with 40  $\mu\text{L}$  of 0.1 M  $\text{Li}_2\text{S}_4$  catholyte solution in the supporting electrolyte. a) Impedance spectra of a H14(film) | Li cell after electrochemical film deposition similar to Figure 55a, b) impedance spectra of fresh H14 | Li cell and a discharged H14 | Li cell with a film deposit, where fresh catholyte has been added. Note the size difference of the  $R_{CT}$  between the fresh cell and the discharged cell with fresh catholyte added.

One important argument to take into consideration in the mentioned study is again the disproportionation of polysulfides, which could aid in the film dissolution after their addition. This was tested through FIB-SEM study of a GC(film) | fresh catholyte | Li cell. We wanted to prove that the film is still present on the electrode surface, which was ultimately supported by the microscopy findings (Figure 57). The entire electrode was covered with a film on the order of 100 nm with some cases of thicker deposits. There were also some spots with <math><10\text{ nm}</math> coverage, where we propose further reaction could take place (Figure 57c,g,i - asterisks). A similar study was also done on carbon felt electrode cell, where again different thicknesses and porosities of the deposits were detected (Figure 58).

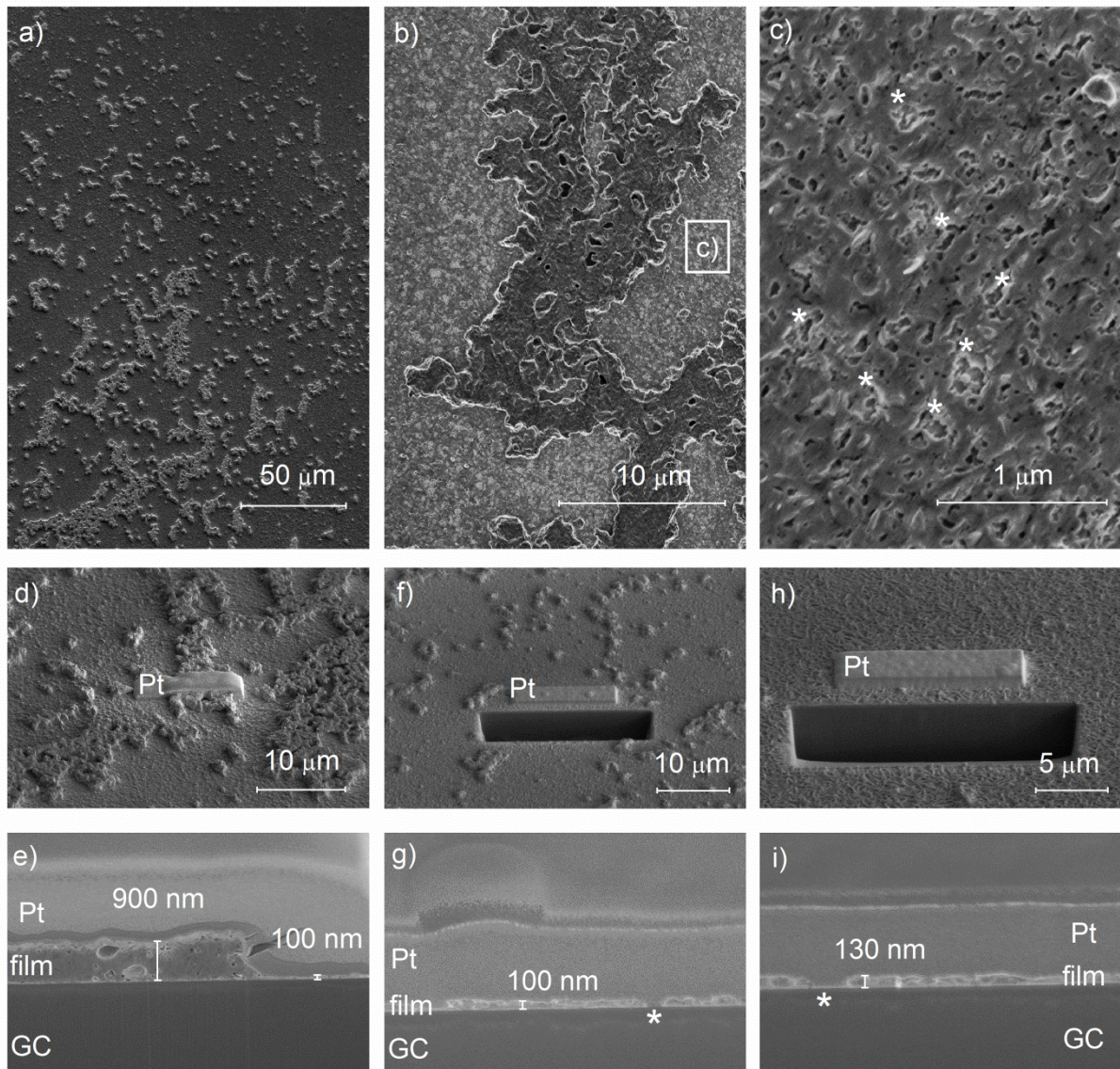
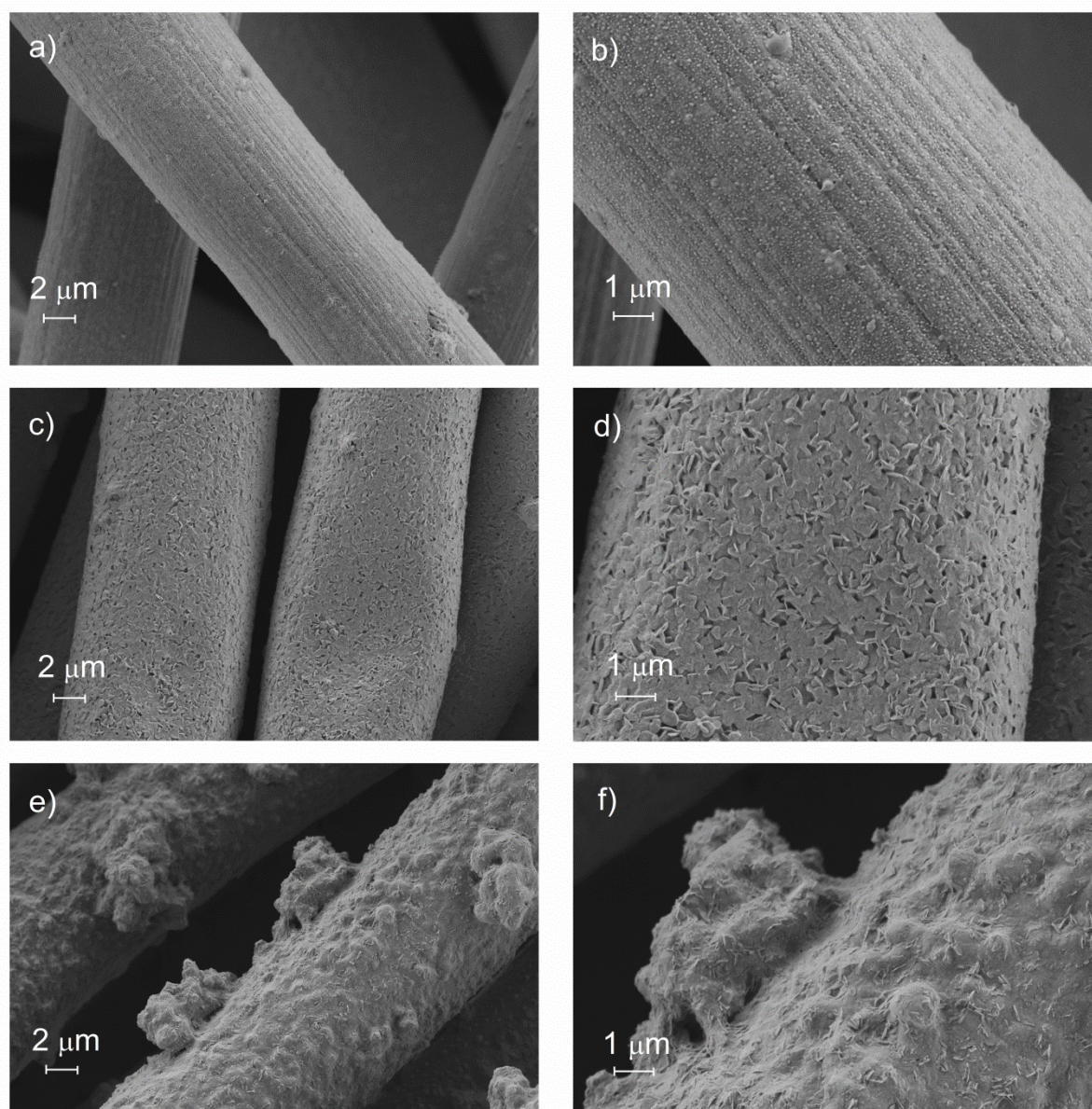


Figure 57: SEM images of the film deposit on a glassy carbon electrode, where fresh catholyte solution has been added – a) and b) different magnifications of top down view indicating islands of thicker deposit; c) magnification of the area indicated in b) with asterisks marking bright spots, where the film deposit was very thin. According to this analysis we estimated the amount of accessible surface area of the electrode to between 5 and 15%; d) and e) top down view and the corresponding cross section of a part where a thicker “island” deposit of approx. 900 nm thickness can be seen, note the porous structure of the film; f), g), h) and i) top down view and the cross section view of two different spots where thinner (100 nm) film is evident. The asterisks mark the spots where the film is likely below 10 nm thickness and reaction can take place (in correspondence with asterisks from c)).



**Figure 58:** SEM images of the film deposit on a carbon felt electrode, where fresh catholyte solution has been added (Figure 56) – a) and b) different magnifications of thin film deposit; c) and d) porous structure of a thicker deposit; e and f) large particle-like deposit.

To further support these claims, lithium insertion material was added to the carbon/sulfur electrode.  $\text{Li}_4\text{Ti}_5\text{O}_{12}$  (LTO) was chosen, since its plateau is flat and at a potential lower than the low voltage plateau of sulfur reduction reactions. The cells were prepared by mixing ENSACO/S (1/2 mass ratio) composite, LTO, Printex conductivity additive and PVdF in 4:4:1:1 ratio and casting the slurry in NMP on brushed nickel foil. Loading of sulfur in the cathodes prepared in such a way was app.  $0.65 \text{ mg/cm}^2$ , while the loading of LTO was app.  $1.0 \text{ mg/cm}^2$ . The cell was discharged with a C/10 current in regards to the sulfur loading until the voltage cut off of 1.3 V vs.  $\text{Li/Li}^+$  was reached. The current calculated in regards to the LTO loading was therefore C/1.75. The discharge begins with the plateaus corresponding to the reduction of

sulfur species, reaching 890 mAh/g<sub>S</sub> (Figure 59a). If the electrode would at this point be passivated due to the formation of a nonconductive Li<sub>2</sub>S film (and this would be the reason for less than theoretical capacity obtained from the cell), then we expected the cell's potential to drop directly afterwards. This experiment, however, shows that after the sulfur conversion reactions are depleted, lithiation of LTO starts and reaches around 150 mAh/g<sub>LTO</sub>. This again shows that the electrode is not passivated due to Li<sub>2</sub>S film formation. The electrode was also studied by SEM, revealing a similar coverage of different size crystals forming a porous deposit (Figure 59b-d). These experiments therefore support that a thick and complex insulating film is deposited on the cathode during discharge, but that film has a porous structure and does not passivate the electrode surface, meaning that passivation is not the cause of capacity limitations.

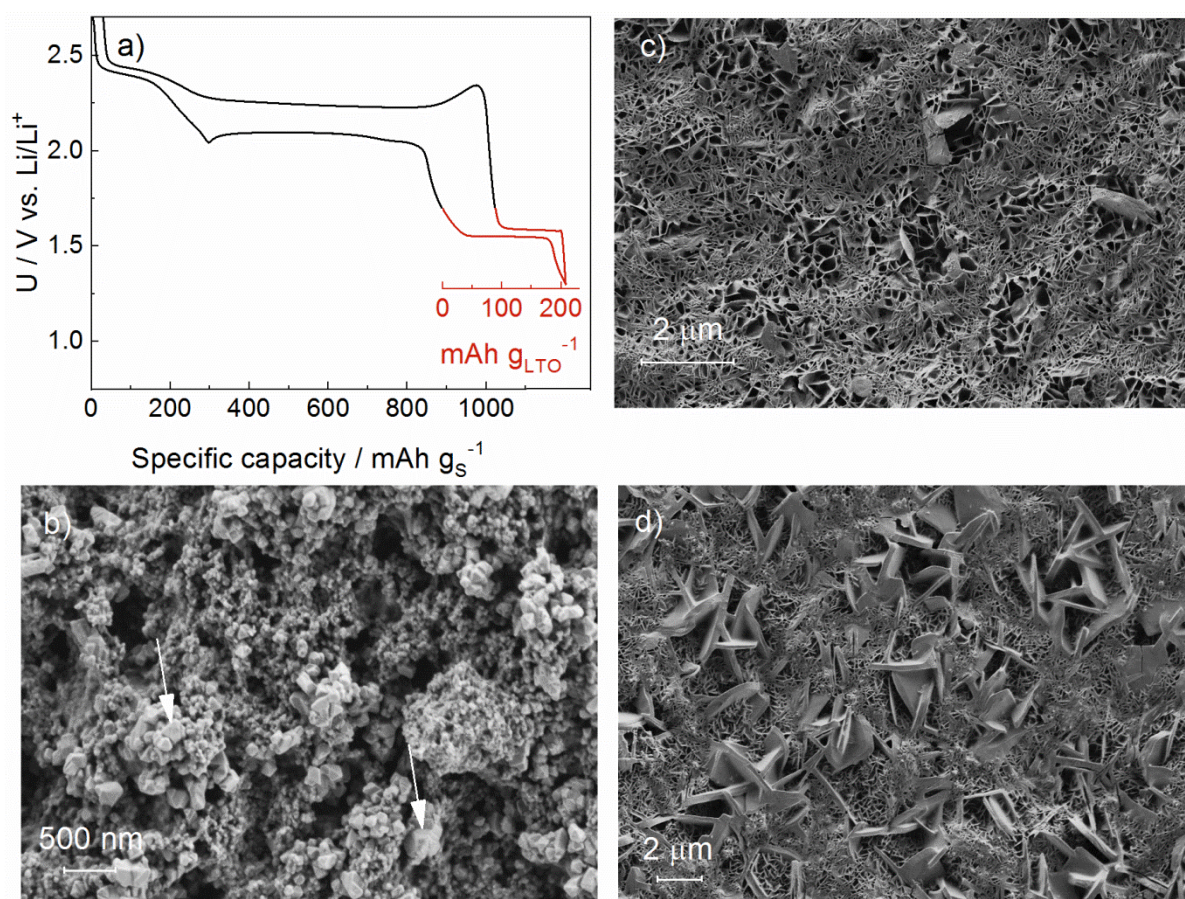


**Figure 59:** LTO addition to the Li-S battery cell. a) electrochemical discharge and charge with electrochemical response of both redox active materials in the composite electrode, b) fresh electrode with arrows pointing to the LTO particles, c) and d) discharged electrode showing large deposits of Li<sub>2</sub>S.

An important question that remains is how the deposition of this film happens inside the porous carbon cathode structure and how it is dependent upon the current used during discharge. For this experiment, we discharged a cell with various current densities (C/3, C/10, C/100, Figure 60a) and analyzed the film morphology with FIB-SEM. The LiTFSI salt in the

electrolyte was exchanged with LiTfDl. The reason for the change is in the effort to stop the sulfur atoms inside the salt anion interfering with the EDS analysis in Z-contrast investigations.

The analysis showed various sized  $\text{Li}_2\text{S}$  deposits on the surface of the electrodes (Figure 60b-d) as well as inside the pore structure. In the larger pores, crystals in the size order of  $1\ \mu\text{m}$  can be seen regardless of the current used during discharge (Figure 60e-g). As expected, larger magnifications revealed porous film structure (Figure 60e), supporting the hypothesis of a non-passivated electrode.

To better visualize the distribution of the film deposit inside the porous carbon matrix, sequential cross-sections were captured by cutting further into the discharged electrode (C/100). A 3D structure of the film (in red) as seen on Figure 60h and i was obtained. Unfortunately, the resolution was not good enough to capture the porous structure of the film deposit. Nevertheless, we could still visualize the large crystals inside the pores and the spots on the surface, which are thin enough to enable redox reactions (blue spots on the surface of Figure 60i, where the carbon phase is detected).

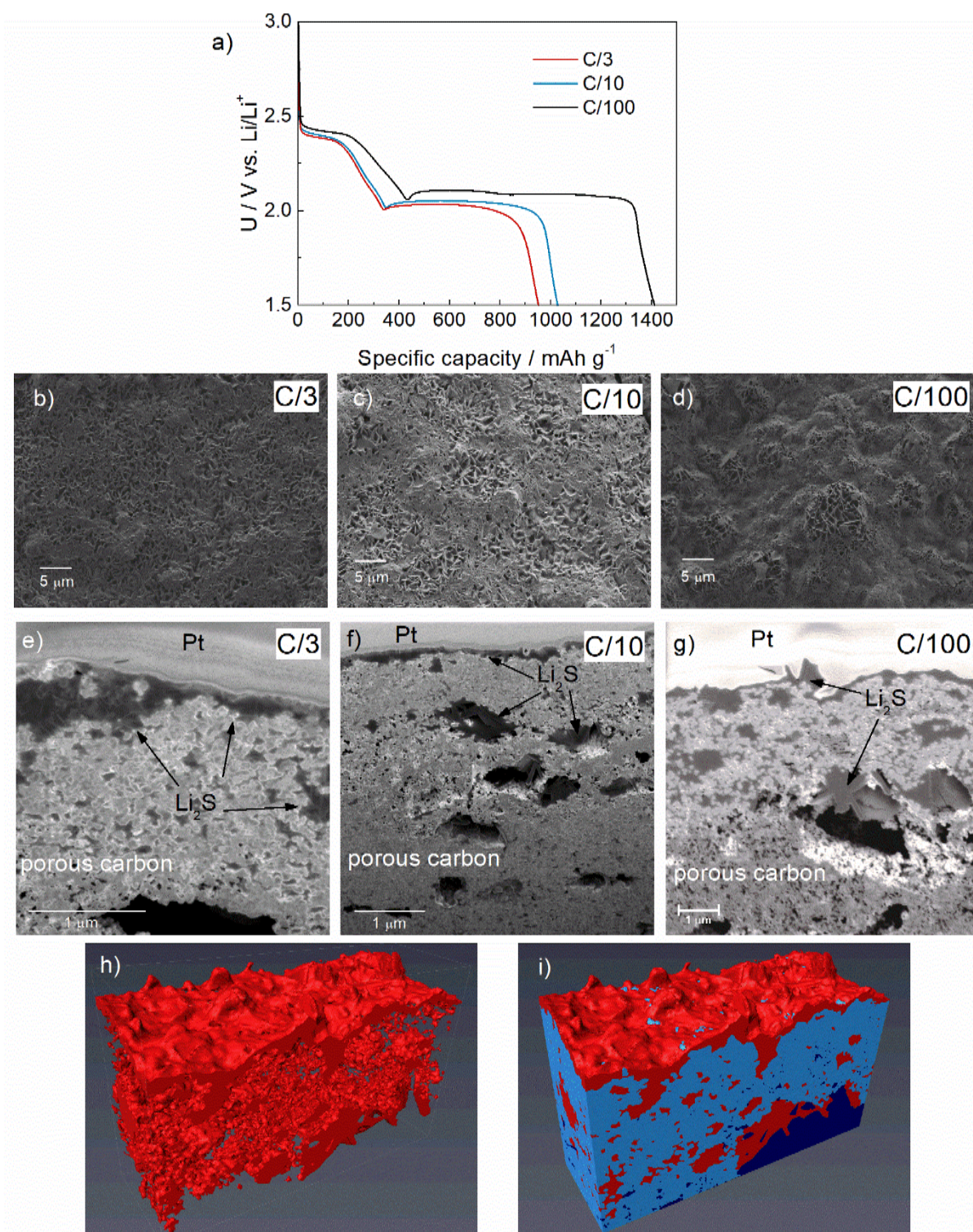


Figure 60: a) Electrochemical discharge with different current densities, b)-d) top down view of different size deposits, e-g) cross sections of ENSACO porous electrodes discharged at C/3, C/10 and C/100 current, respectively, h) and i) 3D reconstructed image of the cathode discharged at C/100.  $\text{Li}_2\text{S}$  film in red, porous carbon in light blue and open pore structure in dark blue. Blue spots on the surface show parts of the carbon electrodes not covered with the film.

To summarise, this study enabled us important insight into the role of the  $\text{Li}_2\text{S}$  precipitation during Li–S battery discharge. It turned out that although nonconductive, the  $\text{Li}_2\text{S}$  film forms

porous structures through the aid of disproportionation reactions of soluble polysulfide species and does not passivate the electrode. Its formation does, however, crucially influence the battery discharge limitations, since polysulfide species are depleted from the electrolyte solution during the process. In the end, the mass transport of the remaining polysulfide species is the bottle neck, which ends the discharge process early. This also made it clear that any side reactions with Li metal surface are highly detrimental to achieving higher discharge capacities (closer to the theoretical one) from the Li–S battery cells and more effort should be aimed at minimizing their effect.

## 5 Conclusions

The studied Li–S battery discharge mechanism and the discovered corresponding impedance change are shown in the bottom scheme.

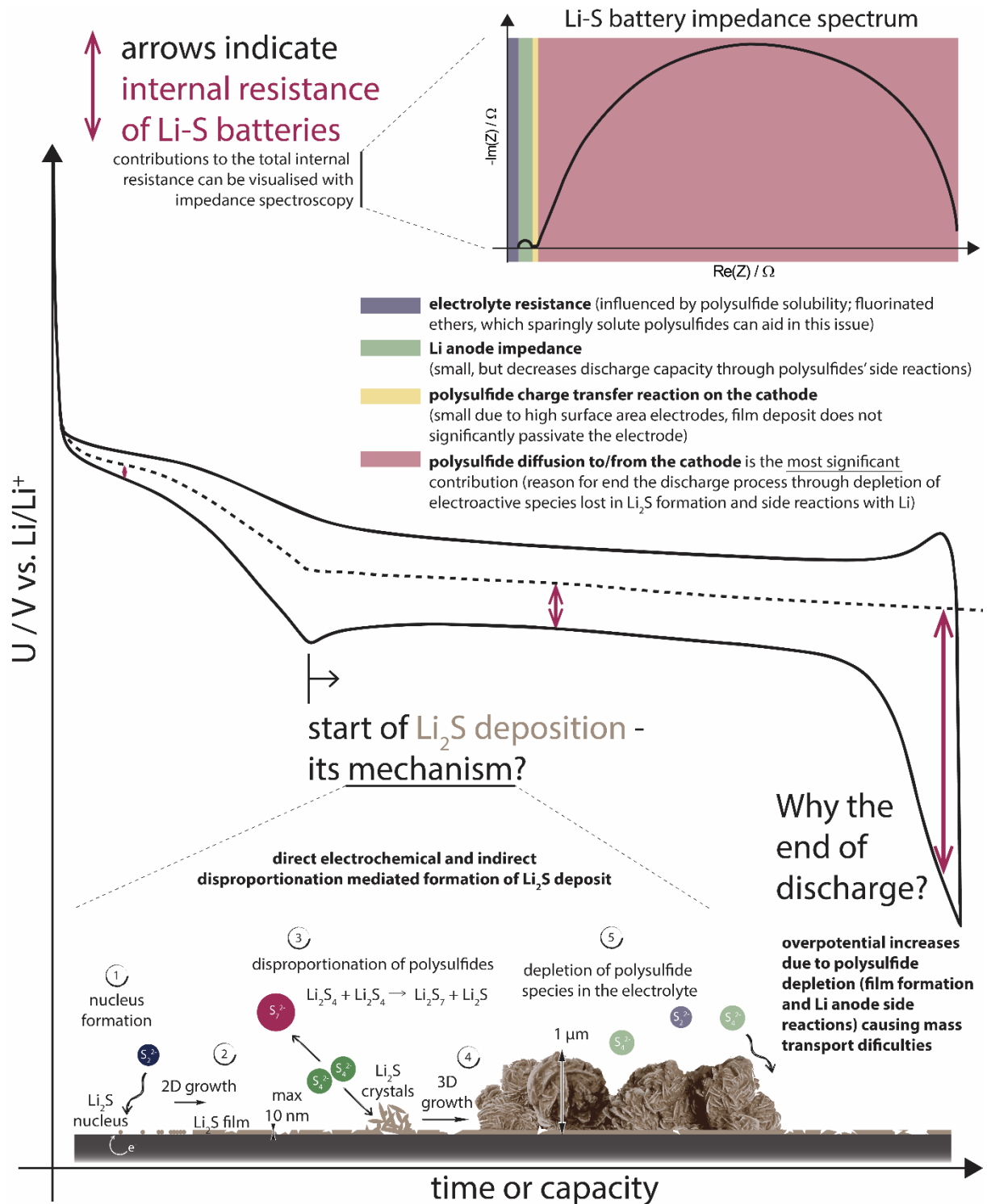


Figure 61: Simplified schematic representation of major conclusions from this doctoral thesis work.

With this research work we have made it clear what influences the electrolyte resistance and how the electrolyte's physicochemical properties should be tailored to achieve the best battery cell performance. We have also distinguished between the anode and the cathode contributions and closely followed their change during battery discharge. The physical meaning behind the internal resistance contributions was elucidated and the polysulfide diffusion determined as the bottle neck of the discharge process. The mechanism of  $\text{Li}_2\text{S}$  deposition through disproportionation-aided porous film formation was explained and the depletion of polysulfide species determined as the cause behind Li–S capacity limitations.

The hypotheses formed at the beginning of the research work for consequently evaluated and confirmed or disproven:

Internal resistance of a lithium–sulfur battery cell could be characterized with the use of impedance spectroscopy.

The hypothesis was confirmed. Standard potentiostatic measurements of impedance spectroscopy at the open circuit potential at different charge levels enabled us the determination different contributions. The resistance of the electrolyte was studied in detail by preparing electrolytes with different physico-chemical properties. By symmetrical cell assembly, we also determined which of the features belong to the processes occurring on the anode and which belong to the reaction and diffusion of species on the cathode. Since the latter showed larger contributions, we focused on the cathode impedance. By simplification of the cell design, we could undoubtedly assign the contributions to their physical meaning and determine which process most significantly influences the performance of Li–S cells.

The use and advantages of dynamic impedance spectroscopy and alternating current voltammetry measurements were also demonstrated. We can conclude that the impedance spectroscopy enables the determination of the size of the selected contributions to the internal resistance of the Li–S battery system after simplified system setup is employed to assign physical meaning to the spectra features.

Physicochemical properties of the electrolyte (viscosity, density, conductivity, solubility of polysulfide species) influence the performance of lithium–sulfur batteries.

This hypothesis was examined through a study of cell operation in an electrolyte system consisting of an ionic liquid [DEME][TFSI], a 1,3-dioxolane solvent and a LiTFSI salt. We found that the most important features are low viscosity, poor solubility of polysulphide species and sufficient concentration of  $\text{Li}^+$  ions, which are then reflected in better Coulombic efficiency, higher achieved capacities, lower overvoltages during operation and lower capacity fade. On the selected system, a significant influence of density and conductivity was not observed. Nevertheless, it is important to emphasise that in the electrolytes based on ionic liquids the transport of its other ions also contributes to the overall specific conductivity.

The influence of the solubility of the polysulphide species was additionally tested with the preparation of an electrolyte based on the fluorinated ether TFEE (a solvent, which sparingly solutes polysulfides), with which we succeeded in producing battery cells with lower electrolyte content, a higher amount of active mass in the cathode and a higher energy. The changes in the cell operation when employing such electrolytes was determined to be a consequence of poor polysulfide solubility, which stems from poor  $\text{Li}^+$  solvation.

Metallic lithium anodes' contribution to the internal resistance will be negligible due to dendritic growth and surface area increase.

The contribution of the metal lithium anode to the internal resistance of a Li–S battery consists of the resistance of the charge transfer reaction, diffusion of the  $\text{Li}^+$  ions to the electrode and back and the complex passive layer on the surface of the electrode permeable to the  $\text{Li}^+$  ions (SEI). During discharge of the battery, lithium dissolves in electrolyte in the form of  $\text{Li}^+$  ions and is deposited back on the metallic surface in the form of tiny needles (dendrites) during charging. This significantly increases the anode surface over time (formation of high surface area lithium HSAL), which leads to the conclusion that anode resistance will decrease with the increase in the number of charge and discharge cycles. We have found this hypothesis to be true only in the case of a sufficient amount of electrolyte present in the cell and the use of low current density. When the dendrites are formed, more and more of the electrolyte is consumed for the passivation of the newly formed metal lithium layer, while the lower current density is associated with a lower proportion of dendritic growth. Significant performance issues were found with the use of low electrolyte amount and fluorinated ether solvents, where stability of the passive layer was poor.

Other important effects of Li anodes, which alter other contributions to the internal resistance of the Li–S battery system, were also found during research. As mentioned above, due to the passivation of lithium, significant electrolyte loss can occur, which results in an increase of its resistance. Furthermore, the polysulfides are reduced in contact with lithium, which of course influences the impedance response of the positive electrode. Ultimately we attribute this loss in active mass as the main cause for less than theoretical capacity obtained from Li–S battery cells.

In summary, although the  $\text{Li}/\text{Li}^+$  reaction and diffusion impedance contributions are smaller than the impedances of the cathode's processes, they can significantly alter the impedance response of the positive electrode and their effect cannot be labelled as negligible. This hypothesis was therefore disproven.

Porous cathode build out of carbon-sulfur composite has the most significant contribution to the internal resistance of the lithium–sulfur battery cell. A contributing factor is among others the deposition of an insulating layer of  $\text{Li}_2\text{S}$  across its surface.

We have been able to distinguish between the charge transfer reaction and diffusion contributions in different cell designs. We also followed their evolution during discharge. In all the cell setups employed, the diffusional contribution of polysulfide transport through the separator pores was the largest of the features, suggesting that Li–S battery operation is mass transport limited.

We have also confirmed that  $\text{Li}_2\text{S}$  deposition during cell discharge greatly influences the cell's performance and impedance. However, the conducted experiments show that this effect is not due to electrode surface passivation, but rather a consequence of polysulfide species depletion from the electrolyte. A new mechanism for  $\text{Li}_2\text{S}$  deposition was also presented, which follows a two-step process. Nucleus formation through direct electrochemical reduction and subsequent three-dimensional deposit formation aided with disproportionation reactions between soluble polysulfide species, which act as redox mediators.

In summary, this means that Li–S battery discharge is stopped at less than theoretical capacity due to polysulfide species depletion, which are used up in the process of  $\text{Li}_2\text{S}$  film precipitation. Since the concentration of polysulfides in the electrolyte is low, the diffusion towards the electrode is increasingly harder and the overpotential increases above the voltage cut-off limit. An important process also influencing the obtained capacity is the side reaction of any polysulfide species that come in contact with the anode and are lost for further reactions.

## 6 Razširjen povzetek v slovenskem jeziku

### 6.1 Litij–žveplovski akumulatorji

Večina prenosnih elektronskih naprav, ki so danes na tržišču, kot vir električne energije uporablja Li-ionski akumulatorje. Le ti so bili v zadnjih desetletjih široko raziskani in komercializirani, vendar nizka energijska gostota ( $300 \text{ Wh kg}^{-1}$ ) omejuje njihov nadaljnji razvoj. Uporaba katodnih materialov na osnovi niklja in kobalta k omejitvam dodatno prispeva z visoko ceno in pomanjkanjem surovin.<sup>7</sup>

Novejša alternativa sistemu so litij–žveplovski (Li–S) akumulatorji, v katerih se uporabljajo lažji, cenejši in širše dostopni materiali. Ti hkrati obljublajo nekajkratno izboljšavo energijske gostote (teoretično  $2500 \text{ Wh kg}^{-1}$ , praktično  $600 \text{ Wh kg}^{-1}$ ).<sup>7,8</sup>

#### 6.1.1 Mehanizem delovanja

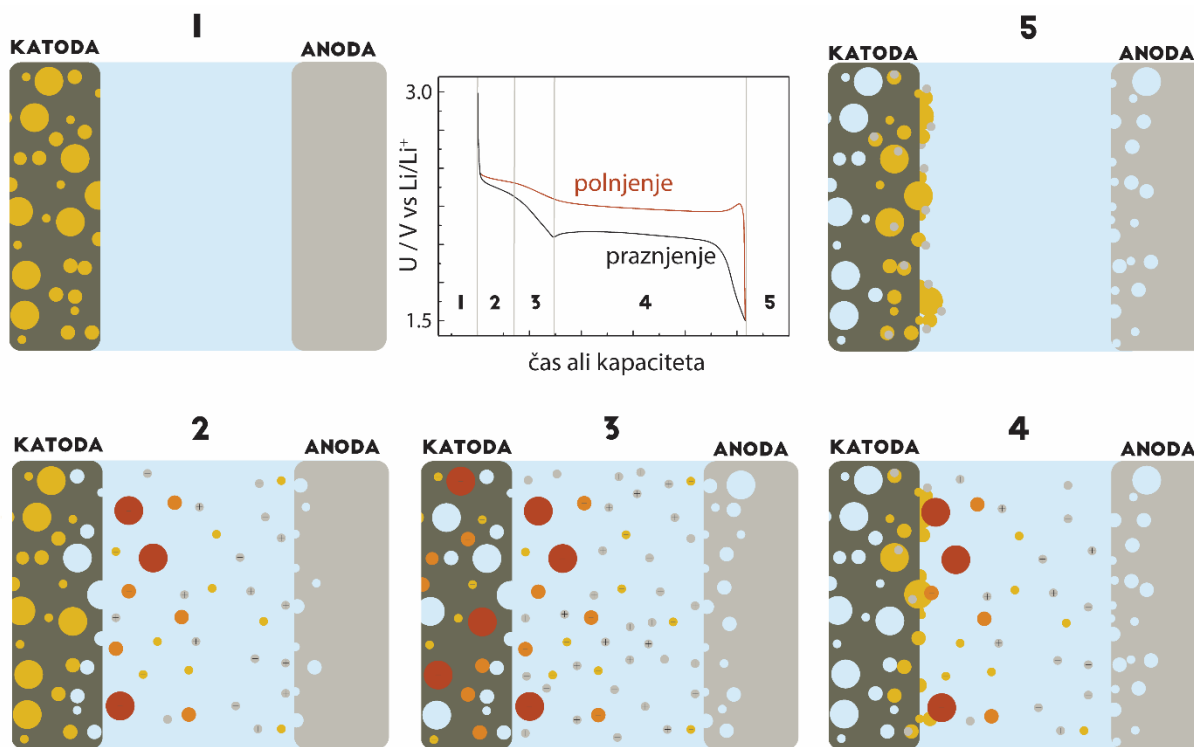
Li–S akumulatorji delujejo na osnovi redukcije žvepla do litijevih polisulfidov ( $\text{Li}_2\text{S}_n$ ) ter  $\text{Li}_2\text{S}$ .<sup>9</sup> Akumulatorska celica je običajno sestavljena iz ogljikove kompozitne katode z različno stopnjo poroznosti in žveplom v porah, kovinske litijeve anode in separatorja omočenega z elektrolitom.<sup>11</sup>

Slika 1 prikazuje tipični galvanostatski odziv Li–S akumulatorja. Spodnji del krivulje pripada praznjenju in zgornji del polnjenju celice. V območju višjega napetostnega platoja (2,3–2,4 V) se trdno žveplo pretvori v topne polisulfide, pri čemer ostaja napetost konstantna dokler je še prisoten neraztopljen trden material.<sup>12</sup> Ko je celotna aktivna masa reducirana do topnih polisulfidov, napetost pade. V spodnjem platoju (2,1–2,0 V) se ti polisulfidi reducirajo do netopnega litijevega sulfida, ki se obori na površini katode.<sup>10</sup> Pri tem se litijeva anoda oksidira in raztaplja v obliki  $\text{Li}^+$  ionov.<sup>8</sup> V polnjenju se dogaja obraten proces, pri čemer je od sestave celice odvisno, če sta raztapljanje  $\text{Li}_2\text{S}$  in obarjanje žvepla časovno ločena procesa, kar včasih privede do samo enega napetostnega platoja v polnjenju.<sup>14</sup> Težava pri polnjenju je med drugim tudi elektrodepozicija Li, pri čemer se tvorijo dendriti, ki lahko povzročijo kratek stik v celici.<sup>19</sup>

#### 6.1.2 Težave in izzivi

Komercializacijo Li–S akumulatorjev omejuje več težav. Prva je neprevodna narava žvepla in litijevega sulfida, kar zahteva dodatke za prevodnost, ki zvišajo maso neaktivnih komponent v celici. Razen tega lahko neprevodnost litijevega sulfida ob njegovem odlaganju med praznjenjem akumulatorja povzroči zmanjšanje aktivne površine katode ali zamašitev njenih por, kar privede do povečanja energije potrebne za nadaljevanje elektrokemijskih reakcij.<sup>16</sup>

Ob praznjenju Li–S akumulatorja se pojavi težava zaradi razlike v gostoti začetnega elementarnega žvepla in končnega produkta,  $\text{Li}_2\text{S}$ , ki nanese 80% volumsko širitev. Taka razlika lahko podre porozno ogljikovo strukturo katode in povzroči slabšo elektronsko povezavo in nižje dosežene kapacitete celice.<sup>17</sup>



Slika 1: Stopnje delovanja Li–S akumulatorja

Zaradi topnosti litijevih polisulfidov v elektrolitu imajo Li–S akumulatorji slabo Coulombsko učinkovitost polnjenja. Pojav se imenuje redoks prenos naboja polisulfidnih zvrsti. Med polnjenjem lahko nastali polisulfidi daljših verig migrirajo čez separator do anode, kjer se ob stiku z litijem reducirajo. Krajši polisulfidi, ki na ta način nastanejo, potujejo nazaj do katode, kjer se oksidirajo v daljše polisulfidne verige, s čimer se cikel nadaljuje. V praksi ta pojav pomeni izgubo aktivne mase, težavo pri doseganju popolnega napolnjenja ter visoko stopnjo samoizpraznitve.<sup>18</sup>

### 6.1.3 Pogosto uporabljeni materiali

Prva objava na področju Li–S akumulatorjev sega v leto 1962<sup>20</sup>, sistem pa je postal še posebej popularen po letu 2010. Tako je bilo samo v letu 2016 objavljenih 669 publikacij na to temo.<sup>33</sup> Ob taki količini raziskav je težko popolnoma povzeti njihove izsledke, v naslednjih odstavkih pa bo zapisan kratek pregled najpogosteje uporabljenih elektrodnih materialov, elektrolitov ter separatorjev.

Priprava katod za Li–S akumulatorje je zapleten proces z velikim številom parametrov. Najpogosteje se celice sestavlja v polnem stanju, torej je v katodi žveplo, nekaj raziskav pa je bilo narejenih tudi na katodnem materialu iz  $\text{Li}_2\text{S}$ <sup>34–37</sup> ali topnih polisulfidnih zvrsti, ki so še posebej zanimive za pretočne akumulatorje<sup>38–40</sup>. Ker je žveplo neprevodno se ga pred pripravo katod zmeša z dodatki za prevodnost. Načini inkorporacije žveplovih delcev v ogljikove pore so različni: od taljenja<sup>41</sup>, infiltracije iz tekočine<sup>43</sup>, mehanske intruzije<sup>44</sup> do odlaganja preko kemijske reakcije<sup>45</sup>. Pomembna je tudi izbira specifične površine, velikosti por ter njihove porazdelitev v ogljikovi matrici<sup>8</sup>, saj bi naj enkapsulacija žvepla pripomogla k zmanjšanju pojava redoks prenosa naboja polisulfidnih zvrsti. Pogosto uporabljeni materiali so saje<sup>46</sup>, ogljikove nanocevke<sup>18,47</sup>, nanovlakna<sup>48</sup>, reduciran grafen oksid<sup>49</sup> in grafen<sup>50</sup>, nekaj raziskav pa je bilo opravljeni tudi na uporabi matrice iz kovinskih oksidov.<sup>44,51,52</sup> Na koncu delovanje celice ni odvisno samo od strukture katode, temveč tudi od količine žvepla v njej<sup>53</sup>, njene debeline<sup>54</sup>, veziv ter topil uporabljanih med njeno izdelavo<sup>55</sup>.

Površina kovinske litijeve anode se v Li–S akumulatorju nenehno spreminja zaradi reakcije z elektrolitom in polisulfidnimi zvrstmi, ki difundirajo čez separator. Zaradi tega na površini nastaja pasivni sloj elektrolita na medfazni meji (solid electrolyte interphase, SEI), ki se zaradi dendritske rasti nenehno spreminja.<sup>56</sup> Zaščita litija se ponavadi izvaja na enega izmed treh različnih načinov: preko spremembe elektrolita, separatorja ali direktne modifikacije površine, kjer so bile uporabljene *ex situ*<sup>57,58</sup> in *in situ*<sup>59,60</sup> formacije stabilnega pasivnega sloja ali uporaba litijevih zlitin.<sup>19,61</sup>

Elektroliti namenjeni za uporabo v akumulatorskih sistemih morajo v splošnem omogočati enostaven ionski transport, biti elektronsko neprevodni, termično, elektrokemijsko in mehansko stabilni ter netoksični za ljudi in okolje. Izbrano topilo mora raztopiti zadostno količino soli (imeti visoko dielektrično konstanto), vendar imeti nizko viskoznost. Zaradi vseh zahtev, ki so včasih kontradiktorne, se ponavadi uporabljajo binarne mešanice elektrolitov in topil, ki omogočajo zahtevane lastnosti.<sup>62</sup> Razen teh osnovnih vodil vloga fizikalno-kemijskih lastnosti elektrolitov v Li–S akumulatorjih ni dobro poznana. Prve objave na področju elektrokemije polisulfidov so uporabljale elektrolite na osnovi tetrahidrofurana (THF)<sup>25</sup>, danes pa je področje raznoliko, pri čemer so elektroliti največkrat sestavljeni iz linearnih ali cikličnih etrskih topil z litijevim bis(trifluorometansulfonil) imidom (LiTFSI) kot soljo.<sup>16</sup> Zanimivo področje je tudi uporaba elektrolitov na osnovi ionskih tekočin<sup>63</sup>, polimernih<sup>29,68–71</sup> ter trdnih elektrolitov<sup>67</sup>, ki lahko pripomorejo k zmanjšanemu pojavu redoks prenosa naboja polisulfidnih zvrsti.<sup>63</sup> Sprememba elektrolita je enostaven način dodajanja koristnih aditivov. V Li–S akumulatorjih je najbolj znan dodatek  $\text{LiNO}_3$ <sup>72</sup>, ki zaščiti litij in preko tega omogoči stabilnejše delovanje<sup>73</sup>. Razen nitratov se je kot dodatke testiralo že več različnih organskih in anorganskih spojin, pri čemer nekateri služijo kot stabilizacija litija<sup>59,74</sup> in nekateri kot redoks mediatorji na katodni strani<sup>36,75</sup>. Z namenom proizvodnje čim lažjih baterij se v Li–S akumulatorskem sistemu podrobno kontrolira količina dodanega elektrolita<sup>76</sup>, pri čemer so bile delujoče celice pripravljene s količinami že od 3  $\mu\text{L}$  elektrolita na mg žvepla naprej<sup>77</sup>.

Pogosto uporabljeni separatorji so poliolefinski ali na osnovi steklenih vlaken, preko funkcionalizacije separatorja<sup>78</sup> ali dodajanja različnih aktivnih plasti pa lahko poskušamo omiliti difuzijo polisulfidov ter zaščititi kovinsko litijevo anodo<sup>79</sup>.

#### 6.1.4 Notranja upornost Li–S akumulatorja

Ena izmed osnovnih lastnosti akumulatorskih celic je njihova totalna notranja upornost, ki določa napetosti in kapaciteto akumulatorja med njegovo uporabo. Preko tega totalna notranja upornost vpliva tudi na moč in energijo, ki jo akumulator lahko dovede. Za njeno analizo se ponavadi uporablja tehnika impedančne spektroskopije. V primeru Li–S akumulatorjev se je v ta namen tehnika že uspešno uporabila za določitev notranje ohmske upornosti<sup>142</sup>, formacije in raztapljanja trdnih reakcijskih produktov<sup>80,84</sup> ter fenomena padanja kapacitete<sup>83,85,87</sup>.

V splošnem je impedančni odziv sistema odvisen od upornosti elektrolita in kontaktnih upornosti (ohmske izgube) ter impedance obeh elektrod, kjer so prispevki odvisni od reakcij prenosa naboja in difuzije redoks aktivnih zvrsti. Odziv dodatno komplicira še formacija pasivnih filmov ali odlaganje materiala na elektrode.<sup>90</sup>

## 6.2 Hipoteze

Notranjo upornost litij–žveplovega akumulatorja lahko okarakteriziramo s tehniko impedančne spektroskopije.

V veliko sistemih se lahko notranjo upornost akumulatorja razišče preko meritve impedančnega spektra v umirjenem stanju, če je potencial dovolj konstanten, pa je meritev možno opraviti tudi dinamično (ko teče tok čez sistem). Li–S redoks sistem je zaradi topnosti polisulfidov v elektrolitu ter njihovega prenosa naboja precej kompleksen in se zaradi tega stanje v baterijski celici hitro spreminja, kar predstavlja poseben izziv pri izvajanju eksperimentov. Predpostavljamo, da je možno zasnovati eksperiment, s katerim lahko primerno raziščemo prispevke k notranji upornosti litij–žveplovega sistema.

Fizikalno–kemijske lastnosti elektrolita (viskoznost, gostota, specifična prevodnost, topnost polisulfidnih zvrsti) znatno vplivajo na delovanje litij–žveplovih akumulatorjev.

Prispevek pri najvišjih frekvencah impedančnega spektra predstavlja upornost elektrolita, ki je seveda povezana z njegovo specifično prevodnostjo. Zaradi topnosti polisulfidov se ta tekom uporabe akumulatorja spreminja. Hkrati sklepamo, da na delovanje akumulatorja vplivajo tudi druge lastnosti elektrolitov. Viskoznost elektrolita najverjetneje vpliva na difuzijo polisulfidnih zvrsti do elektrodne površine. Koncentracija raztopljenih soli vpliva na prevodnost ter topnost polisulfidnih zvrsti, podoben vpliv pa ima tudi uporaba različnih topil, v katerih je topnost polisulfidov drugačna. Vse to se odraža tudi na spremembi notranje upornosti akumulatorja.

Kovinska litijeva anoda zaradi dendritske rasti ter posledično večanja njene površine ne prispeva bistveno k notranji upornosti Li–S akumulatorja.

Dendritska rast Li je dokaj znan pojav<sup>56,91–93</sup>. Sklepamo, da se bo prispevek anode k upornosti baterijske celice zaradi večanja njene površine manjšal in bo postal zanemarljiv.

Porozna katoda iz kompozita ogljik–žveplo najznatneje prispeva k notranji upornosti baterijske celice. Razlog je med drugim tudi v procesu odlaganja neprevodnega Li<sub>2</sub>S na površino.

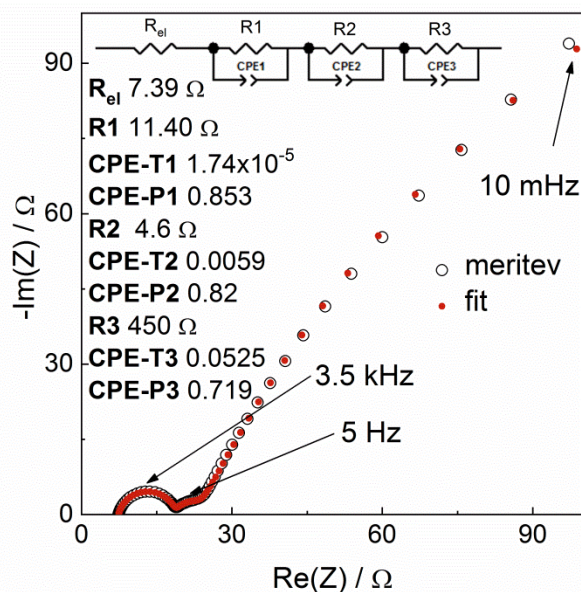
Zadnja stopnja praznjenja Li–S akumulatorja je nastanek litijevega sulfida, ki se v elektrolitih slabo topi, hkrati pa je neprevoden. Ta se torej nalaga na katodno površino, tako zapira njene pore ter povečuje prispevek k notranji upornosti.

### 6.3 Rezultati in diskusija

Za analizo notranje upornosti Li–S akumulatorjev so bile uporabljene celice pripravljene z različnimi elektroliti (1 M LiTFSI v [DEME][TFSI]:dioksolan (DOL) 1:2, sulfolan:DOL 1:1 in TEGDME:DOL 2:1), ki so bili izbrani tako, da imajo podobne viskoznosti. Uporabljen je bil presežek elektrolita (60  $\mu\text{L}$  na mg S), ENSACO 350G ogljikove katode z 1 mg S na  $\text{cm}^2$  in separator iz steklene volne GF/D. Impedančni spektri celic so bili pomerjeni v območju 1 MHz–10 mHz z amplitudo 10 mV (rms) na svežih celicah. Akumulatorji so bili potem praznjeni s tokom C/20 eno uro, preden se je tok čez celico ustavil za obdobje 15 minut, nato pa se je ponovno pomeril impedančni spekter v izbranem območju. Postopek se je ponavljal, dokler ni celica dosegla 1.5 V vs. Li/Li<sup>+</sup>, nato pa še čez polnjenje do 3.0 V vs. Li/Li<sup>+</sup> in naslednjih 50 ciklov praznjenja in polnjenja.

Na tako pomerjenih impedančnih spektrih (Slika 2) so bili v programu ZView opravljeni fiti z arbitrarnim električnim vezjem. Vrednost vsote vseh štirih prispevkov skupaj se giblje okoli 1–2 k $\Omega$ , kar se dobro ujema z oceno notranje upornosti iz razlike napetosti platojev v galvanostatskem delu eksperimenta. Spektri vseh pomerjenih celic so bili podobni glede števila prispevkov in njihovih velikosti.

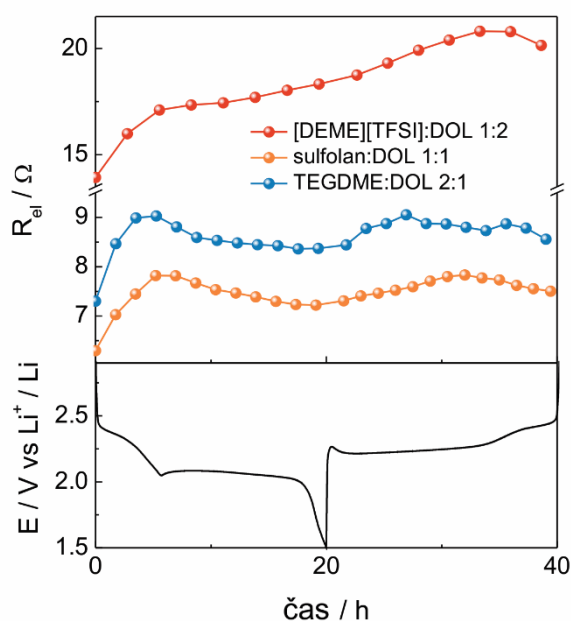
Prispevek  $R_{el}$  (Slika 2) predstavlja upornost elektrolita in kontaktov ter je edini, ki smo mu lahko nedvoumno pripisali izvor. Ostale prispevke smo kasneje raziskali s simetričnimi celicami Li|Li in katoda|katoda. Izbrano vezje za fit takih spektrov nima direktne povezave s fizikalnimi pojavi v celici, ampak smo ga uporabili kot najenostavnejše vezje, ki dovolj dobro opiše znane prispevke. Preko tega smo lahko spremljali njihov razvoj čez več ciklov uporabe celice.



Slika 2: Tipični impedančni spekter Li–S akumulatorja pri 50% izpraznjenosti (elektrolit na osnovi sulfolana). Rdeči krogi predstavljajo fit s prikazanim ekvivalentnim električnim vezjem.

### 6.3.1 Visokofrekvenčni odsek na realni osi

Visokofrekvenčni odsek na realni osi (Slika 2,  $R_{el}$ ) predstavlja upornost elektrolita in upornost vseh kontaktov celice. Na slednjega zaradi optimizirane oblike celice nimamo veliko vpliva, medtem ko se upornost elektrolita čez praznjenje in polnjenje Li–S akumulatorja značilno spreminja (Slika 3).<sup>12,90</sup> Razlog v taki spremembi upornosti je v topnosti polisulfidnih zvrsti v elektrolitu. Visokofrekvenčni odsek se tako povečuje zaradi večanja viskoznosti elektrolita, pred začetkom nižjega napetostnega platoja pa se vrednosti zmanjšajo zaradi obarjanja polisulfidov v obliki  $\text{Li}_2\text{S}$ . Podoben pojav se zgodi tudi v polnjenju akumulatorja. Vrednost upornosti se ne spusti več na začetno vrednost, kar nakazuje, da polisulfidi ostanejo ujeti v separatorju. Na prevodnost elektrolita lahko vpliva še reakcija z Li anodo, ki pa tukaj ni bila raziskana.



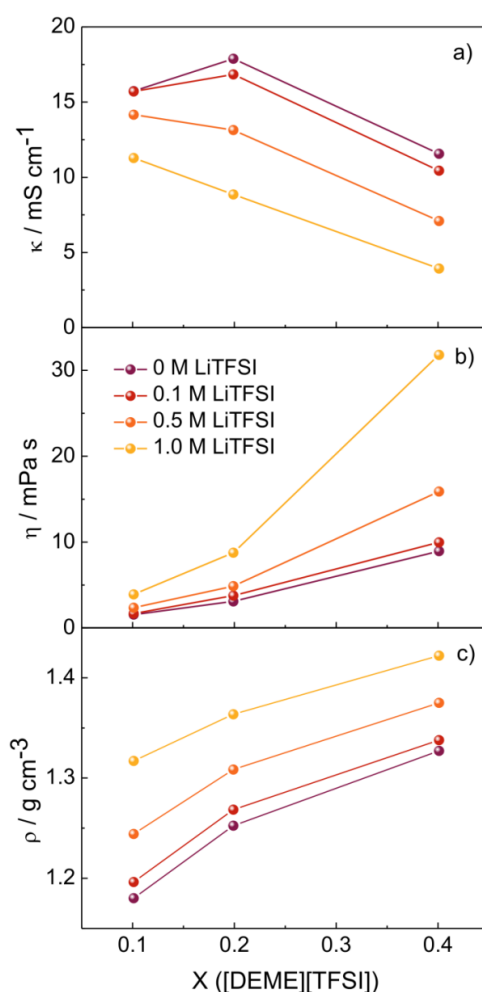
Slika 3: Sprememba upornosti elektrolita čez prvi cikel praznjenja in polnjenja Li–S akumulatorja v treh različnih uporabljenih elektrolitih.

#### a) Vpliv fizikalno-kemijskih lastnosti elektrolitov na delovanje Li–S akumulatorjev

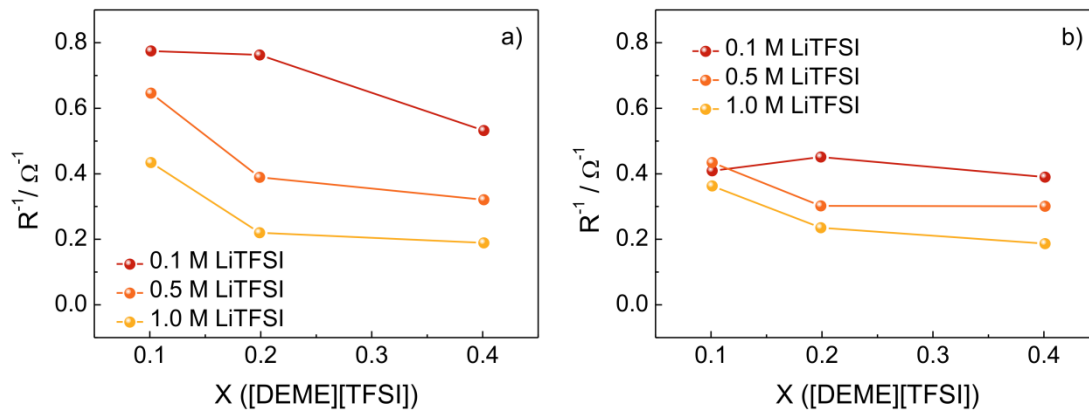
Da bi bolje razumeli vpliv in delovanje elektrolita v Li–S akumulatorju smo na izbranem elektrolitskem sistemu (ionska tekočina [DEME][TFSI], topilo DOL in sol  $\text{LiTFSI}$ ) opravili določitev fizikalno-kemijskih lastnosti ter njihovega vpliva na delovanje akumulatorskih celic. Določene so bile prevodnost, viskoznost, gostota ter topnost polisulfidov, delovanje akumulatorjev pa je bilo okarakterizirano z določitvijo dosežene specifične kapacitete,

padanja kapacitete čez 100 ciklov praznjenja in polnjenja, Coulombske učinkovitosti ter prenapetosti med delovanjem.<sup>105</sup>

Izbranih je bilo devet elektrolitov s tremi različnimi deleži ionske tekočine v mešanici z DOL ( $X_{[\text{DEME}][\text{TFSI}]} = 0.101, 0.199, 0.401$ ) in tremi različnimi koncentracijami soli LiTFSI (0.1 M, 0.5 M, 1.0 M). Določene fizikalno-kemijske lastnosti so prikazane na spodnji sliki (Slika 4). Prevodnost elektrolitov v odvisnosti od deleža ionske tekočine ima pri različnih koncentracijah različen trend. Pri nizkih koncentracijah LiTFSI ima krivulja maksimum pri srednji vrednosti, med tem ko pri večjih koncentracijah soli prevodnost z večanjem deleža ionske tekočine pada. Razlog je v mešanem vplivu koncentracije prenašalcev naboja (povečanje izboljša prevodnost) in večanja viskoznosti, ki prevodnost manjša. Pri tem je ob uporabljenem sistemu potrebno opozoriti, da tako izmerjena prevodnost pripada tako migraciji anionov kot kationov, med tem ko je za delovanje izbranega akumulatorja pomembna samo prevodnost zaradi migracije  $\text{Li}^+$  ionov. Viskoznost ter gostota se večata z višjim deležem ionske tekočine in večjo koncentracijo LiTFSI.



Slika 4: Fizikalno-kemijske lastnosti elektrolitskega sistema [DEME][TFSI]:DOL:LiTFSI pri 298.15 K a) specifična prevodnost, b) dinamična viskoznost, c) gostota

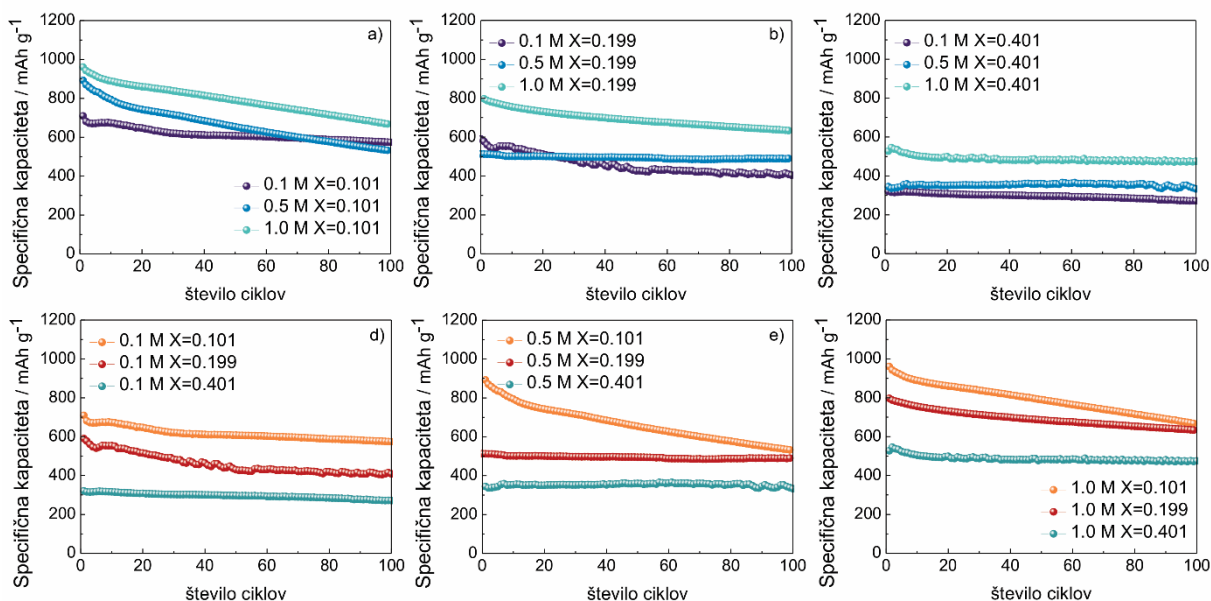


Slika 5: Prevodnost elektrolita v akumulatorski celici podana kot inverzna vrednost visokofrekvenčnega odseka in impedančnem spektru a) sveže celice pred uporabo, b) polne celice po desetih ciklih praznjenja in polnjenja.

Topnost polisulfidov je bila določena s primerjavo spremembe visokofrekvenčnega odseka med svežo celico in celico po desetih ciklih uporabe s tokom C/10. Impedančni spekter se je pomeril z amplitudo 10 mV (rms) v območju frekvenc 1 MHz do 10 mHz. Izkaže se, da se največja sprememba zgodi pri elektrolitih z najnižjim deležem ionske tekočine in najmanjšo koncentracijo LiTFSI soli (Slika 5). Take izsledke podpirajo tudi literaturni podatki, ki kažejo, da lahko visoka koncentracija soli v elektrolitu prepreči raztapljanje polisulfidnih zvrsti.

Za izbran elektrolitski sistem gostota in prevodnost ne kažejo direktne povezave z elektrokemijskim delovanjem. Coulombska učinkovitost je povezana s topnostjo polisulfidov, primerjava prenapetosti pa je pokazala odvisnost od viskoznosti, če jo primerjamo za elektrolite z enako koncentracijo LiTFSI soli. Pri nižjih koncentracijah raztopljene soli je potrebno upoštevati še efekt koncentracijske polarizacije. Najvišje kapacitete so bile dosežene z 1.0 M LiTFSI v X=0.101, padanje kapacitete z večjim številom ciklov pa je povezano v večjim deležem DOL, oziroma boljšo topnostjo polisulfidov (Slika 6).

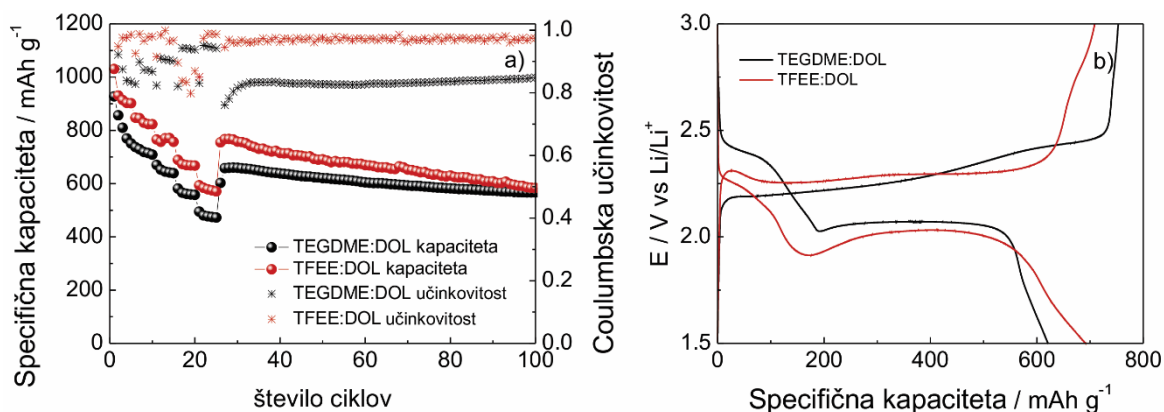
V splošnem mora torej elektrolit za optimalno delovanje v Li–S akumulatorskem sistemu imeti raztopljeno dovoljšno koncentracijo Li<sup>+</sup> soli, da se izognemo efektom koncentracijske polarizacije, za doseganje dobrih učinkovitosti polnjenja in zmanjšanje padanja kapacitete pa je potrebna nižja topnost polisulfidnih zvrsti.



Slika 6: Specifične kapacitete med praznjenjem: a-c prikazujejo mešanice z enakim deležem ionske tekočine in drugačnimi koncentracijami LiTFSI, pri čemer je na a)  $X=0.101$ , b)  $X=0.199$  in c)  $X=0.401$ ; d-f prikazujejo primerjavo delovanja elektrolitov z enako koncentracijo LiTFSI z d) 0.1 M LiTFSI, e) 0.5 M LiTFSI in f) 1.0 M LiTFSI.

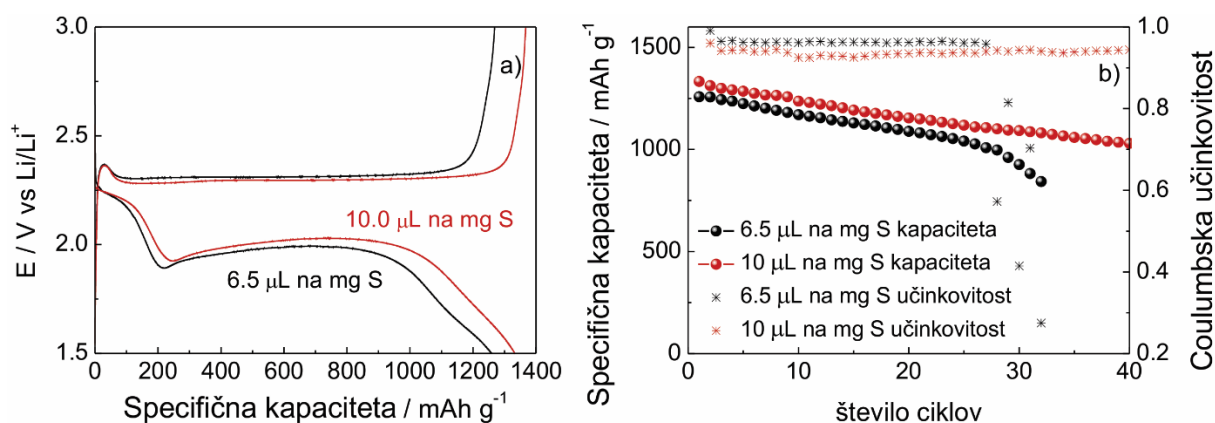
### b) Elektroliti s slabo topnostjo polisulfidnih zvrsti

Iz določanja vpliva fizikalno-kemijskih lastnosti elektrolitov na Li–S akumulatorje se je izkazalo, da lahko zmanjšana topnost polisulfidnih zvrsti izboljša njihovo delovanje. Tak elektrolitski sistem je bili raziskan z določitvijo delovanja elektrolita na osnovi fluoriranega etra TFEE (1,2-(1,1,2,2-tetrafluoroetoksi)etan). Primerjava delovanja »tradicionalnega« elektrolita in elektrolita na osnovi TFEE z uporabo 20  $\mu\text{L}$  elektrolita na mg S in Celgard 2400 separatorja je prikazana na spodnji sliki (Slika 7). Z uporabo fluoriranih etrov se dosežena kapaciteta malo poveča, opazna pa je velika izboljšava pri Coulombski učinkovitosti, ki se iz 82% pri TEGDME elektrolitu poveča na 97% za TFEE elektrolit. Razlika med elektrolitoma je vidna tudi v napetosti galvanostatskih platojev, saj je višji napetostni plato pri TFEE za 150 mV nižje, kot pri elektrolitu na osnovi TEGDME, med tem ko je spodnji napetostni plato pri podobnih vrednostih. Ker je sprememba v isti smeri opazna tudi pri polnjenju akumulatorjev, sledi, da je ta sprememba termodinamske in ne kinetične narave.



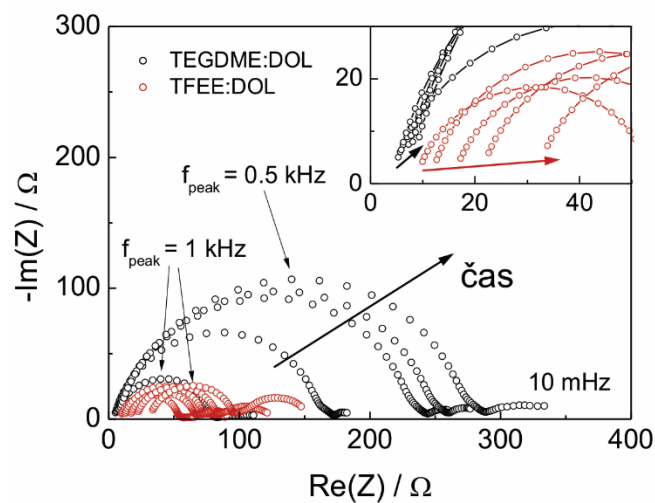
Slika 7: Primerjava delovanja “tradicionalnega” elektrolita na osnovi TEGDME in TFEE elektrolita: a) kapaciteta ter Coulombska učinkovitost pri različnih tokovnih gostotah (C/20-C/10-C/5-C/2-1C-C/10), b) galvanostatski profil praznjenja in polnjenja v 50. ciklu. Razmerje topil TFEE/TEGDME in DOL je bilo 1:1 (v:v)

Spreminjanje razmerja TFEE:DOL v pripravljenem elektrolitu (mešanice 2:1, 1:1 in 1:2) je pokazalo, da se z večanjem deleža TFEE izboljša učinkovitost, vendar zmanjša kapaciteto, kar med drugim pripisujemo spremembi viskoznosti. Kompromis je tako predstavljal že uporabljena mešanica v volumskem razmerju 1:1, s katero je bila sestavljena visokoenergijska Li–S akumulatorska celica (Slika 8). V ta namen so bile uporabljene katode z višjim nanosom aktivnega materiala (4 mg S na cm<sup>2</sup>) in manjša količina elektrolita (6.5 μL na mg S). S samo enim slojem Celgard separatorja je celica dosegla izjemno delovanje v prvih 25 ciklih uporabe s kapaciteto preko 1000 mAh g<sup>-1</sup> in učinkovitostjo okoli 97%. Po 25 ciklih so visoki tokovi v celici povzročili litijeve dendrite in notranje kratke stike. Povečanje količine elektrolita je delno izboljšalo začetno kapaciteto, vendar je bilo padanje kapacitet s številom ciklov podobno, učinkovitost polnjenja pa se je zmanjšala. Celica z večjo količino elektrolita je delovala dlje, kar potrjuje hipotezo, da je nestabilnost Li anode razlog za prenehanje delovanja celice.



Slika 8: Kapaciteta in učinkovitost polnjenja za visokoenergijsko Li–S akumulatorsko celico z 6.5 μL na mg S in 10 μL na mg S 1 M LiTFSI v TFEE:DOL 1:1 (v:v). Količina žvepla v katodi je bila 4 mg na cm<sup>2</sup>, na a) je prikazan prvi cikel, na b) sprememba kapacitete čez več ciklov delovanja.

Stabilnost litija je bila testirana z impedančno spektroskopijo na simetričnih Li||Li celicah (Slika 9). Dve elektrodi velikosti  $2\text{ cm}^2$  sta bili ločeni z enim slojem Celgard 2400 separatorja in omočeni z  $20\ \mu\text{L}$  izbranega elektrolita (1 M LiTFSI TEGDME:DOL 1:1 ali 1 M LiTFSI TFEE:DOL 1:1). Spektri so bili pomerjeni čez obdobje 50 ur v območju 20 kHz do 10 mHz z amplitudo 10 mV (rms). Za »tradicionalni« elektrolit je bil visokofrekvenčni odsek na realni osi dokaj stabilen, med tem ko se je upornost pasivnega sloja na površini litija povečala iz  $150\ \Omega$  na skoraj  $300\ \Omega$ . Pri elektrolitu s fluoriranim etrom je bil prispevek pasivnega sloja bolj stabilen, vendar se je upornost elektrolita nekajkrat povečala (iz  $10\ \Omega$  na  $35\ \Omega$ ). Reakcija Li z elektrolitom je bila vidna tudi v povečanju difuzijskega prispevka pri nizkih frekvencah, kar nakazuje na povečanje viskoznosti elektrolita zaradi izrabljanja topil za stranske reakcije na Li površini.



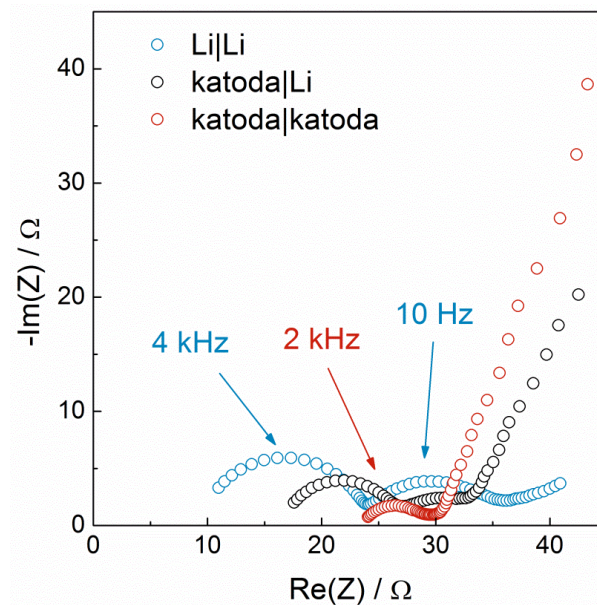
Slika 9: Impedančni spektri Li||Li celic pomerjenih pri OCV čez obdobje 50 ur. Prikazani so spektri pri 1h, 15 h, 25 h, 35 h in 45h. Na vstavljeni sliki je povečan visokofrekvenčni del spektrov, vse puščice pa kažejo smer spremembe s časom.

Sprememba mehanizma delovanja vidna kot nižji potencial za reakcijo žvepla do daljših polisulfidov (višjenapetostni plato) je bila študirana z več analiznimi tehnikami. *Operando* analiza rentgenske absorpcijske spektrometrije žveplovega K-roba je dokazala enak mehanizem delovanja preko nastanka polisulfidnih zvrsti v višjem platuju in  $\text{Li}_2\text{S}$  v spodnjem napetostnem platuju. Z uporabo UV-vis spektroskopije pa smo ovrednotili zmanjšano topnost polisulfidov v elektrolitu s fluoriranim etrom. Razlog za nižjo napetost celic smo s pomočjo raziskovalcev iz univerze Chalmers v Göthenburgu poiskali z modeliranjem kemijskih potencialov polisulfidnih zvrsti v različnih elektrolitih. Izkaže se, da je za slabšo topnost polisulfidov kriva slabša solvatacija  $\text{Li}^+$  ionov v fluoriranih etrih, kar povzroči tudi spremembo potenciala<sup>115</sup>.

Kot je razvidno iz Slike 2, k celotni notranji upornosti upornost elektrolita ( $R_{el}$ ) ne prispeva znatno, saj so ostali impedančni prispevki (reakcija in difuzija na obeh elektrodah) mnogo večji. V nadaljevanju nas je zanimala določitev fizikalnega vzroka posameznega prispevka, zaradi česar smo se osredotočili na impedančno analizo Li–S celic pri različnih stopnjah napolnjenosti.

### 6.3.2 Anodni prispevek k notranji upornosti

Kot omenjeno na začetku, iz meritve impedančnega spektra dvoelektrodne Li–S akumulatorske celice ni mogoče razbrati izvora posameznih prispevkov. V namen ločitve med prispevki pozitivne ter negativne elektrode so bile sestavljene simetrične celice<sup>90,121</sup>, pri katerih smo simulirali različne stopnje napolnjenosti. Pripravljeni sta bili dve čim bolj podobni akumulatorski celici, ki sta bili izpraznjeni do izbrane stopnje. Pomerjena sta bila impedančna spektra, nato pa sta se celici razstavili in iz njunih delov sestavili dve simetrični celici, katerima je bil prav tako izmerjen impedančni spekter (Slika 10).



Slika 10: Impedančni spektri simetričnih in akumulatorske celice pri 50% izpraznjenosti. Celice so bile pripravljene iz 1.5 cm<sup>2</sup> elektrod, GF/D separatorja in 60 μL na mg žvepla 1 M LiTFSI v TEGDME:DOL 2:1. Prirejeno iz reference<sup>104</sup>. Avtorske pravice 2017 American Chemical Society.

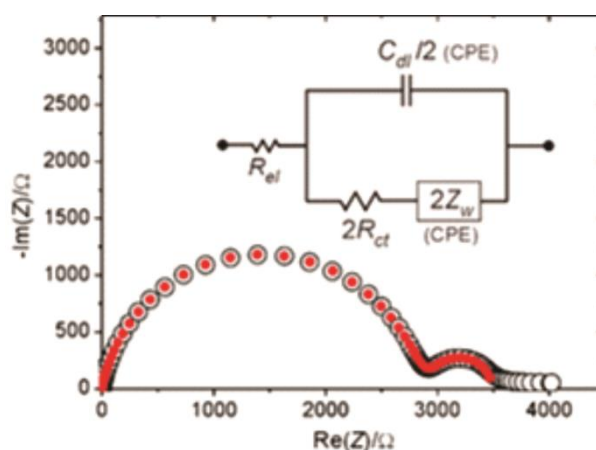
Izkaže se, da je prispevek anode skoncentriran na visokofrekvenčni del, kjer sta vidna dva polkrožna prispevka, medtem ko katodni prispevek prevladuje v nizkofrekvenčnem območju in je tudi najznatnejši prispevek v Li–S impedančnem spektru. Prispevek R1 (Slika 2) je bil tako pripisan anodi, ostali prispevki pa katodnemu delu. Če spremljamo razvoj R1 čez večje število ciklov se namreč izkaže, da se prispevek manjša, kar pripisujemo večanju površine Li zaradi dendritske rasti. Iz tega eksperimenta smo razbrali, da večina notranje upornosti izvira iz katodne strani celice, zaradi česar so bile nadaljnji poskusi posvečeni procesom, ki se na njej dogajajo.

### 6.3.3 Katodni prispevek k notranji upornosti

Velikost katodnega prispevka se giblje v velikostnem redu okoli 1–2 k $\Omega$ , vendar razumevanje elektrokemije polisulfidov otežuje kompleksna poroznost ogljikove elektrode.

#### a) Elektrokemija polisulfidov na elektrodah iz steklastega ogljika

Da bi razumeli fundamentalne procese reakcije in difuzije polisulfidov smo poenostavili sistem z uporabo planarne elektrode iz steklastega ogljika. Sestavljene so bile simetrične celice iz takih elektrod, žveplov material pa je bil v obliki različnih raztopin polisulfidov v 1 M LiTFSI TEGDME:DOL 1:1 elektrolitu dodan na separator.<sup>104</sup>



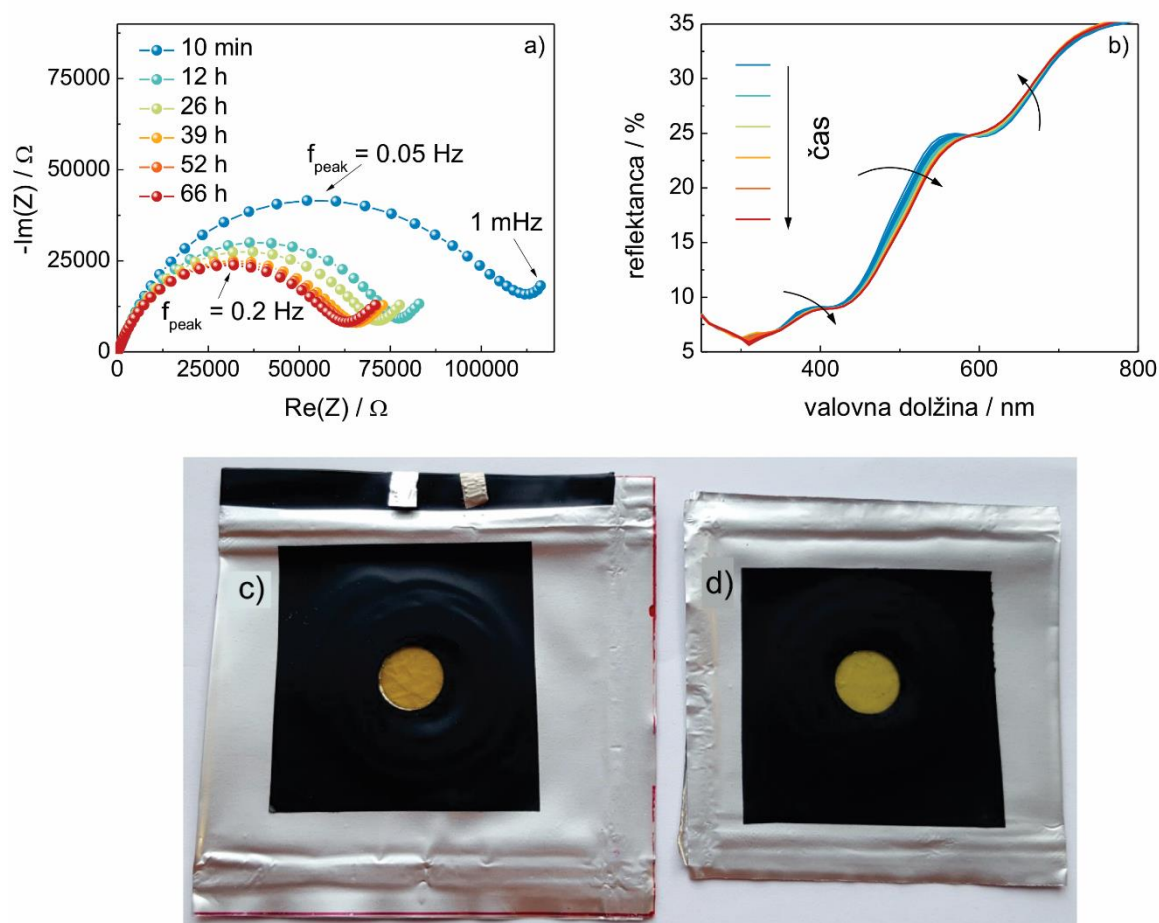
Slika 11: Nyquist prikaz impedančnega odziva  $S_8^{2-}/S_7^{2-}$  redoks para (oba v koncentraciji 0.05 M, Celgard separator, 10  $\mu$ L elektrolita) v frekvenčnem območju 1 MHz do 0.1 mHz v GC | GC celici. Fit s prikazanim ekvivalentnim električnim vezjem je izrisan z rdečimi krogi. Prirejeno iz reference<sup>104</sup>. Avtorske pravice 2017 American Chemical Society.

Impedančni odziv planarnih elektrod je dobro raziskan, kar nam je pomagalo pri nedvoumni določitvi izvora posameznih prispevkov. Izmerjen spekter je bil oblike tipične za Randles sisteme (Slika 11), kar pomeni, da smo lahko določili prispevek reakcije polisulfidov na elektrodni površini (polkrog pri višjih frekvencah) in prispevek difuzije polisulfidov do elektrode (nižje frekvence).

Pri več zaporednih meritvah impedančnih spektrov tako pripravljenih celic se je izkazalo, da se velikost prispevka redoks reakcije spreminja, včasih celo za faktor 2. Ker je znano, da so Li polisulfidi nestabilni in vključeni v vrsto ravnotežij<sup>124,125</sup>, sklepamo, da je razlog za spremembe v impedančnih spektrih disproporcionacija polisulfidov. Raziskava tega pojava je bila opravljena z *operando* UV-vis spektroskopijo, kjer se je ob impedančnih spektrih hkrati merilo še spremembo v obarvanosti separatorja (Slika 12). Namesto elektrod iz steklastega ogljika so se uporabile ploščice platine, da se izognemo absorpciji svetlobe na črni površini. V času

nekaj dni je bila poleg spremembe v impedančnih spektrih vidna tudi sprememba v spektrih UV-vis, ki nakazuje podaljšanje verige S atomov v polisulfidnih molekulah. Ker se celico v tem času ni ne praznilo in ne polnilo, sklepamo, da so poleg daljših polisulfidov nastali tudi krajši, vendar so se ti delno odložili v porah separatorja, zaradi česar spremembe barve ne zaznamo.

Za detekcijo mehanizma disproporcionacije v posamezni GC | GC celici smo razvili dve različni metodi, eno na podlagi priprave različnih razmerij polisulfidnih zvrsti in eno s pripravo celic z različnimi koncentracijami istih polisulfidov.<sup>104</sup>

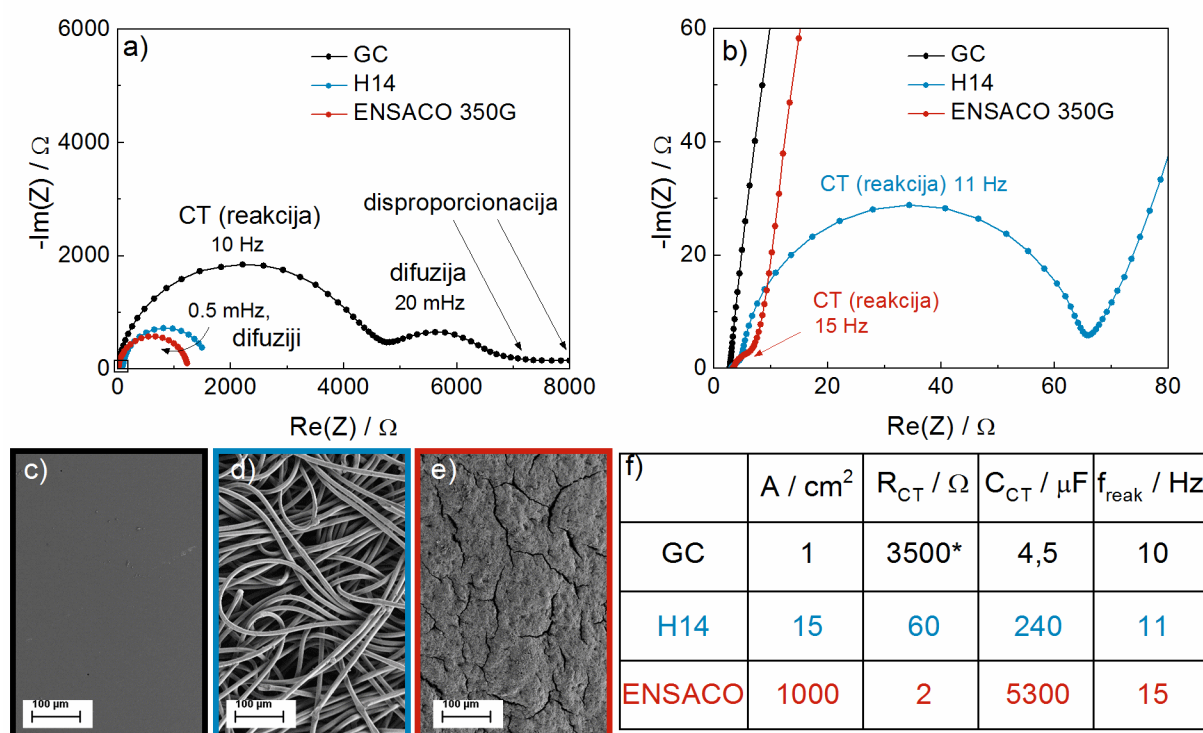


Slika 12: a) Sprememba v impedančnih spektrih Pt | Pt celice z 0.01 M  $\text{Li}_2\text{S}_4$  v TEGDME:DOL 1:1 (v:v) izmerjenimi med 1 MHz in 1 mHz, b) sprememba v UV-vis spektrih pomerjenih vsakih 80 minut, c) barva separatorja 95 ur po sestavi celice, d) sveža celica pripravljena na enak način.

S tem smo uspešno določili impedančni prispevek redoks reakcije polisulfidnih zvrsti na ogljikovih elektrodah in vzpostavili uporabnost modelne celice za določitve mehanizma posameznih procesov v Li – S akumulatorski celici.

### b) Impedančni odziv poroznih ogljikovih elektrod

Ker je impedančni prispevek zaradi redoks reakcije na površini elektrode linearno odvisen od velikosti le-te, so bili  $R_{CT}$  prispevki pri elektrodah s poroznih ogljikov manjši od prispevkov določenih v celicah s planarnimi elektrodami iz steklastega ogljika (Slika 13). Tako smo s primerjavo impedančnih odzivov simetričnih celic pripravljenih iz elektrod iz steklastega ogljika, ogljikovega filca in poroznega ogljika ENSACO uspešno določili fizikalne pomene posameznih prispevkov. Iz tega eksperimenta je jasno razvidno, da je pri visoko površinskih poroznih ogljikovih katodah največji prispevek zaradi difuzije polisulfidnih zvrsti v porah elektrode in separatorja. Podobno razmerje med tema dvema prispevkoma namreč ostane tudi, če predpostavimo, da se površina elektrode s praznjenjem akumulatorja zapira z neprevodnim filmom slabo topnih polisulfidnih zvrsti.



Slika 13: a) Impedančni odziv simetričnih ogljikovih celic pripravljenih z 0.1 M Li<sub>2</sub>S<sub>4</sub> v 1 M LiTFSI TEGDME:DOL 1:1 (v:v), posnetih pri OCV med 1 MHz in 0.1 mHz. b) povečava visokofrekvenčnega dela spektra, c) SEM slika elektrode iz steklastega ogljika (GC), d) SEM slika elektrode iz ogljikovega filca H14, e) SEM slika ENSACO 350G porozne elektrode, f) vrednosti parametrov prispevkov.

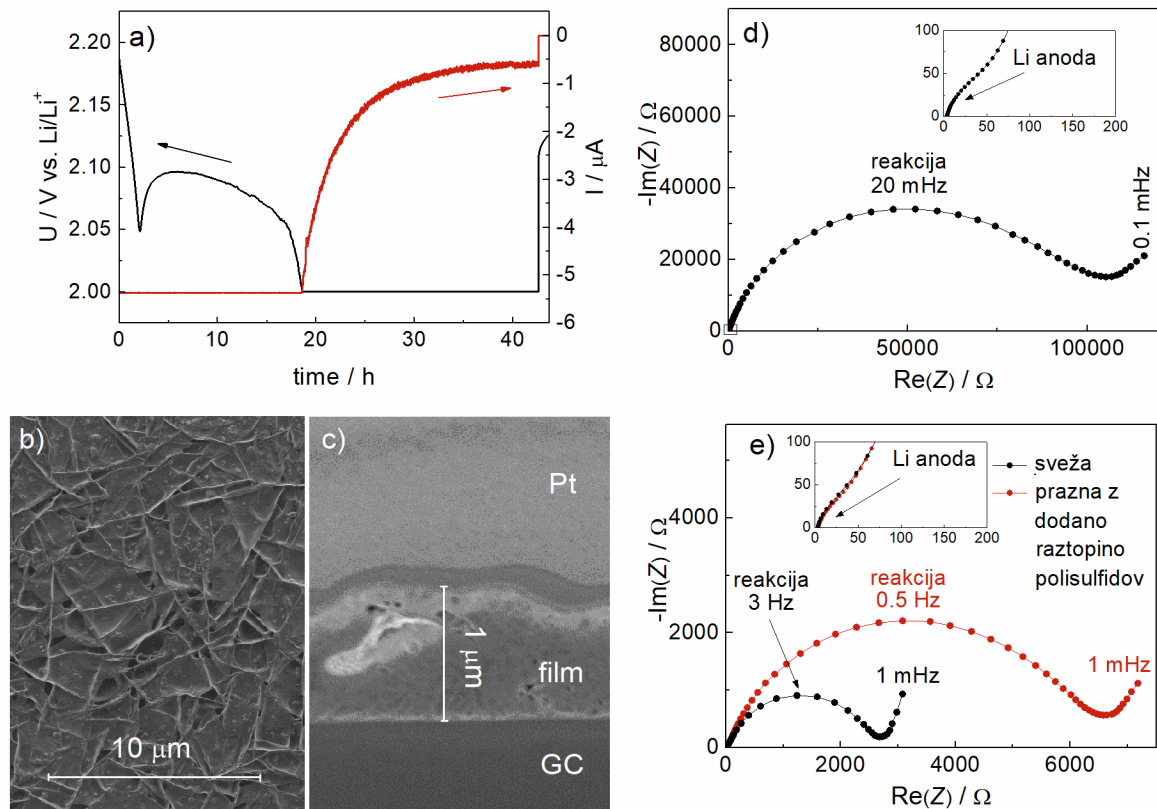
### c) Sprememba katodnega impedančnega odziva s praznjenjem akumulatorske celice

Celice pripravljene iz planarnih elektrod iz steklastega ogljika so bile ponovno uporabljene pri študiju sprememb impedančnega odziva med praznjenjem akumulatorskih celic. Pri zmanjšanju deleža napoljenosti se reakcijski prispevek večja, kar se v literaturi ponavadi pripisuje pasivaciji elektrode zaradi odlaganja neprevodnega filma Li<sub>2</sub>S<sup>75,82,84,128–140</sup>. Težava z

razlago tega pojava je v dejstvu, da je iz naših eksperimentov vidna tudi sprememba frekvence reakcijskega impedančnega prispevka in ker je površina ogljikovega filca 15x večja od površine elektrode steklastega ogljika, kljub temu pa smo iz nje dobili samo 1x večjo kapaciteto. Iz tega sledi, da razlogi za omejitve kapacitete niso tako enostavni, kot so bili zaenkrat prikazani. En izmed očitnih prispevkov k večanju reakcijske upornosti je tudi osiromašenje polisulfidnih zvrsti iz elektrolita, na žalost pa je delež posameznih prispevkov na isti celici težko razločiti, ker se vedno dogajata oba procesa.

Da bi bolje razumeli tvorbo filma smo odložili film  $\text{Li}_2\text{S}$  na planarno ogljikovo elektrodo (Slika 14a). Debelino filma smo določili tudi z analizo FIB-SEM (Slika 14b,c). Kot je razvidno iz slike, je bila debelina analiziranega filma ranga velikosti  $1\ \mu\text{m}$ , nekaj rangov velikosti večja kot predpostavljena debelina  $10\ \text{nm}$ , možna pri dvodimenzionalnem odlaganju  $\text{Li}_2\text{S}$ <sup>75,128,129</sup> omejenem z učinkom tuneliranja elektronov. Na osnovi tega predlagamo drugačen mehanizem tvorbe, kjer se lahko  $\text{Li}_2\text{S}$  odlaga v obliki poroznega tridimenzionalnega filma zaradi topnih polisulfidnih zvrsti, ki se disproporcionirajo<sup>104,141</sup> in delujejo kot redoks mediatorji.

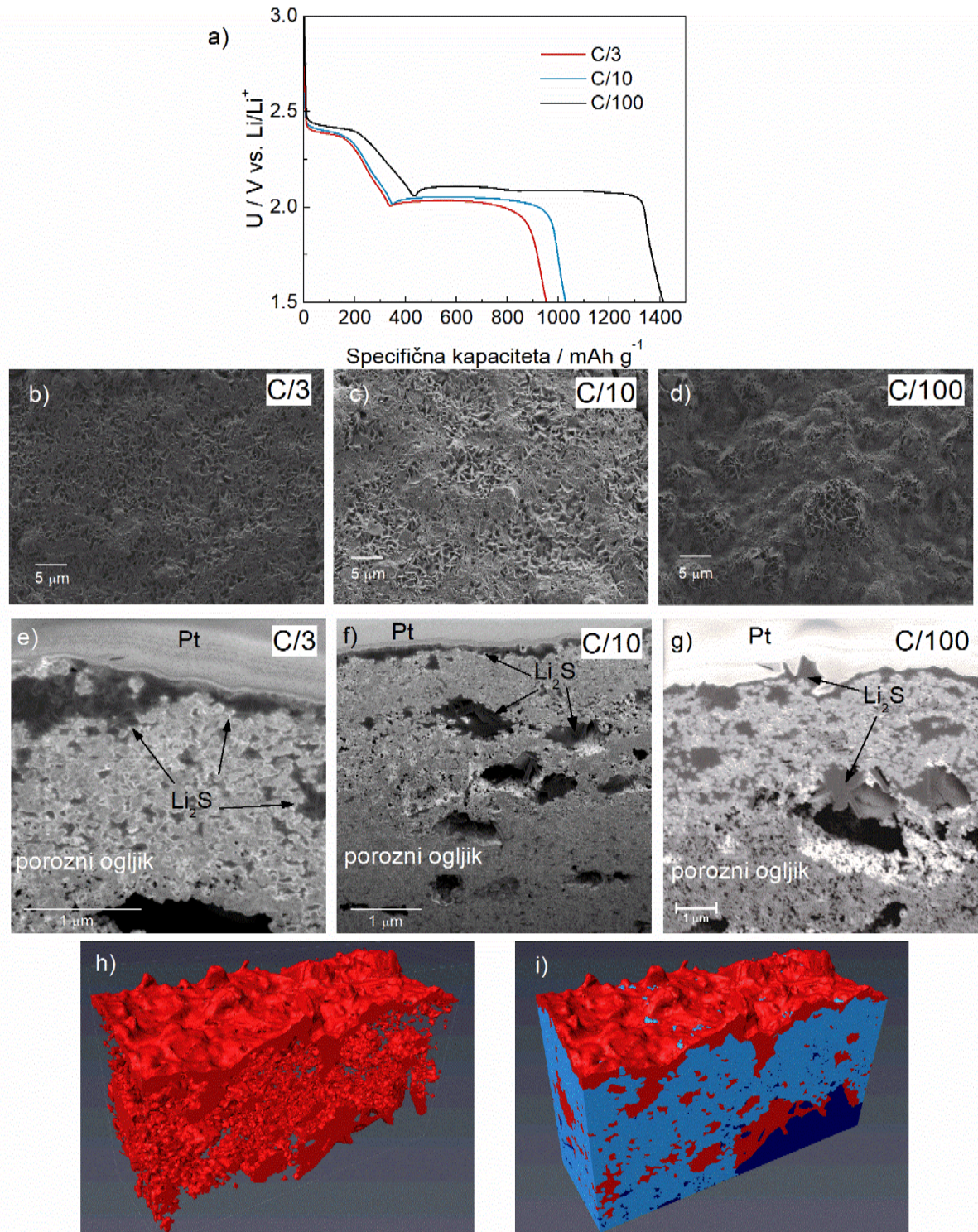
Da bi preverili, kateri izmed učinkov - pasivacija ali osiromašenje - prevlada pri povečanju impedančnih prispevkov, smo v izpraznjeno GC(film)||Li celico dodali svežo raztopino polisulfidov, pri čemer se je impedančni reakcijski prispevek drastično zmanjšal (Slika 14d,e). Eksperimenti tako nakazujejo, da je pri praznjenju Li–S akumulatorjev bolj odločujoč proces siromašnja elektrolita kot pa pasivacije elektrode. To hipotezo smo potrdili še s FIB-SEM analizo, kjer smo v celici z dodatkom polisulfidov, kljub večji težnji po disproporcionaciji in raztapljanju filma, dokazali prisotnost debelega sloja  $\text{Li}_2\text{S}$  na elektrodi.



Slika 14: a) Elektrokemijski eksperiment na GC | Li celici, b) SEM mikrograf filma odloženega na elektrodi, c) prerez in debelina odloženega filma, d) impedančni odziv celice po elektrokemijskem odlaganju filma, e) primerjava reakcijskega impedančnega prispevka sveže elektrode in elektrode z odloženim filmom, kjer je bil v celico dodana sveža raztopina polisulfidnih zvrsti v elektrolitu.

Podobno je hipotezo potrdil še eksperiment z dodatkom litijevega titanata s spinelno strukturo v kompozit žveplave katode. Ta litij-ionski katodni material je bil izbran zaradi potenciala, ki ga izkazuje med praznjenjem, saj je ta pod napetostjo nižjega platoja žvepla. Če bi litijev sulfid omejeval kapaciteto med praznjenjem Li–S akumulatorja, bi to pomenilo, da zaradi pasivacije elektrode tudi litijev titanat ne bi bil elektrokemijsko aktiven. V nasprotju s tem smo dokazali, da tudi ko se žveplave zvrsti iztrošijo celica še naprej deluje v potencialnem območju litijevega titanata.

Pomembno vprašanje se je dotikalo tudi morfologije odlaganja  $\text{Li}_2\text{S}$  v notranjosti porozne ogljikove strukture, oziroma če na njo vpliva velikost toka, ki ga uporabimo med praznjenjem celice. V namen te analize so bile katode izpraznjene z različnimi tokovnimi gostotami (C/3, C/10, C/100), pri čemer je bil z namenom zmanjšanja motenj žveplavih atomov v anionu LiTFSI sol v elektrolitu zamenjana z LiTDI. Preseke tako pripravljenih katod smo analizirali s FIB-SEM, pri čemer so bili v večjih porah zaznani večji kristaliti ( $1\ \mu\text{m}$ ) ne glede na uporabljen tokovno gostoto (Slika 15a-c). Hkrati smo lahko pri večjih povečavah zaznali poroznost odloženega filma, ki omogoča nadaljnje reakcije kljub svoji neprevodnosti (Slika 15a).



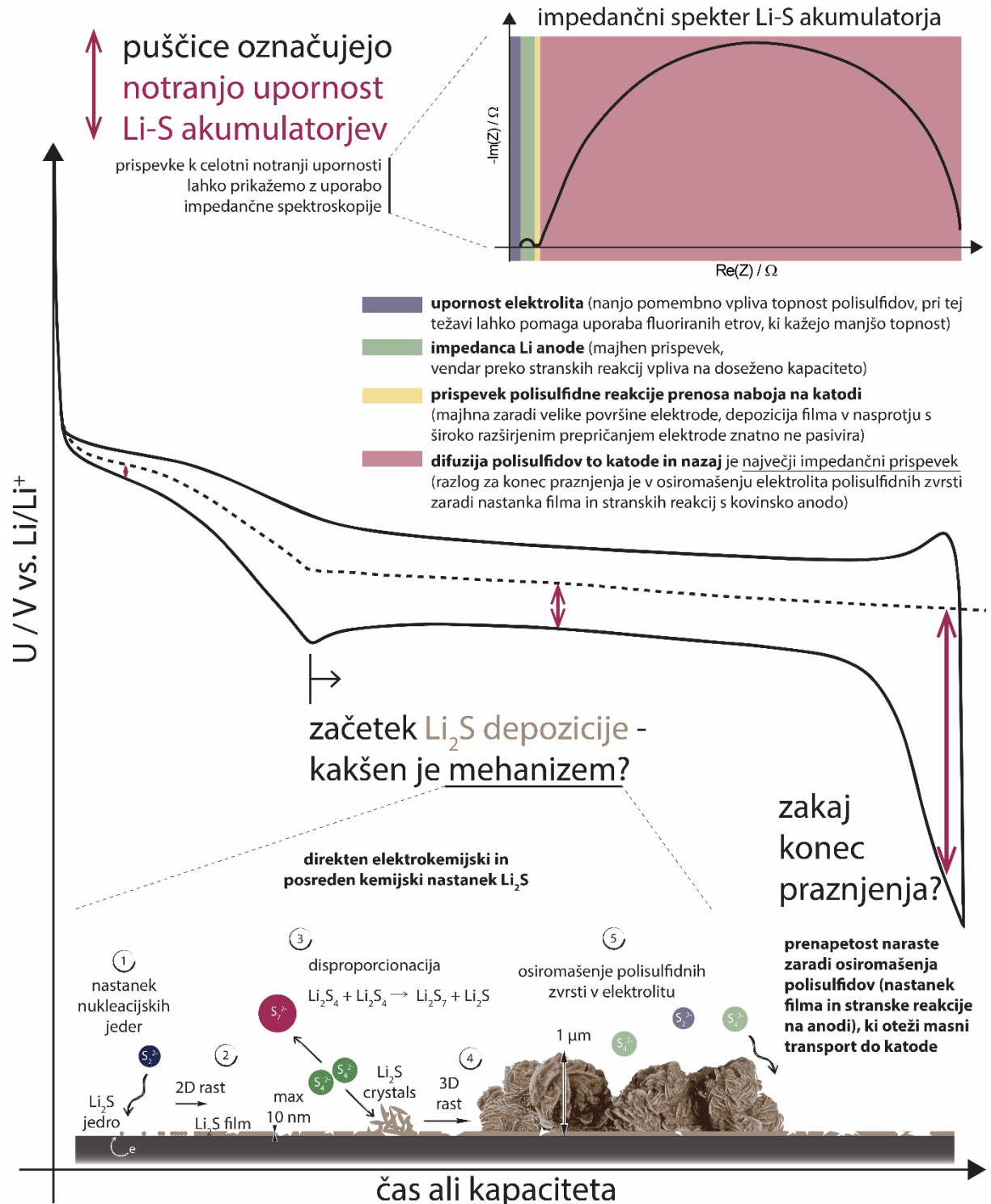
Slika 15: a) Elektrokemija med praznjenjem pri različnih tokovnih gostotah; b)-d) površina elektrode in struktura filma na elektrodah pripravljenih z različnim tokom; e)-g) preseki ENSACO poroznih elektrod pripravljenih pri različnih tokovnih gostotah, h) and i) 3D rekonstruirana struktura katode izpraznjene pri toku C/100.  $\text{Li}_2\text{S}$  faza je prikazana z rdečo, svetlo modra je faza ogljikove elektrode, temno modre so pore.

Za boljšo predstavo faze odloženega filma je bila opravljena še analiza 3D tomografije, za namene katere je bila analizirana katoda izpraznjena s tokom C/100. Pri tem smo lahko izločili fazo filma (Slika 15d,e, rdeče), na žalost pa resolucija ni bila dovolj dobra, da bi lahko prikazali še strukture v notranjosti faze. Pomemben izsledek te študije je bil tudi prikaz področij na površini elektrode, ki niso prekrivane s filmom  $\text{Li}_2\text{S}$ , kjer lahko redoks reakcija še naprej poteka (Slika 15e, svetlo modri otočki ogljika na površini).

Opravljeni eksperimenti so nam tako pomagali razložiti vlogo odlaganja  $\text{Li}_2\text{S}$  na površini pozitivne elektrode med praznjenjem Li–S akumulatorja. Čeprav je material neprevoden, se film odlaga v poroznih strukturah preko stranskih disproporcionacijskih reakcij topnih polisulfidnih zvrsti. Tako film ne pasivira površine, vendar njegov nastanek vseeno pomembno vpliva na konec praznjenja akumulatorja, saj hkrati poteka tudi osiromašenje elektrolita in so v celici vedno večje težave z masnim transportom  $\text{Li}_2\text{S}_x$  zvrsti do katode. Taka razlaga tudi zelo nazorno pokaže, kako pomembna je zaščita kovinske površine litija in preprečitev stranskih reakcij polisulfidov, ki zmanjšujejo vsebnost aktivnih zvrsti.

## 6.4 Zaključek

S tem doktorskim delom je bil natančno določen mehanizem praznjenja Li–S akumulatorja in spremembe v notranji upornosti, ki se pri tem dogajajo. Na spodnji shemi je prikazan poenostavljen prikaz.



Slika 16: Poenostavljen shematski prikaz pomembnih zaključkov ugotovljenih v okviru raziskav tega doktorskega dela.

Raziskan je bil vpliv fizikalno-kemijskih lastnosti elektrolita na delovanje celic in določene smernice za njihov nadaljnji razvoj. Prav tako smo s posebej zasnovanimi eksperimenti uspešno razlikovali med anodnimi in katodnimi impedančnimi prispevki in spremljali njihovo evolucijo čez praznjenje akumulatorja. Tako smo uspeli povezati posamezne prispevke z njihovim fizikalnim ozadjem, pri čemer smo določili, da je glavna ovira pri delovanju difuzija polisulfidnih zvrsti do elektrode. Ovrgli smo široko sprejet mehanizem odlaganja neprevodnega filma  $\text{Li}_2\text{S}$ , ki pasivira površino elektrode in postavili novo teorijo formacije poroznega depozita preko disproporcionacijskih reakcij polisulfidnih zvrsti. Razlog zakaj se iz Li–S akumulatorjev redko pridobi celotna teoretična kapaciteta je bil najden v procesu elektrodepozicije  $\text{Li}_2\text{S}$ , ki osiromaši koncentracije elektroaktivnih zvrsti v elektrolitu.

Hipoteze postavljene na začetku smo ovrednotili sledeče:

Notranjo upornost litij–žveplovega akumulatorja lahko okarakteriziramo s tehniko impedančne spektroskopije.

Hipotezo smo potrdili. S standardno potenciostatsko meritvijo impedančne spektroskopije pri potencialu odprtega kroga pri različnih stopnjah izpraznjenosti smo v Li–S akumulatorjih uspeli določiti prispevke k notranji upornosti Li–S akumulatorjev. Upornost elektrolita smo raziskali s pripravo elektrolitov z različnimi fizikalno-kemijskimi lastnostmi, z uporabo simetričnih celic pripravljenih pri različnih oksidacijskih stanjih polisulfidnih zvrsti ter poroznosti elektrodnega materiala pa smo uspešno ločili anodne in katodne prispevke, oziroma bolj natančno reakcijske in transportne prispevke na pozitivni elektrodi.

Izvedene so bile še meritve dinamične impedančne spektroskopije, za isti namen pa smo dokazali tudi možnost uporabe voltometrije z uporabo izmeničnega toka. Zaključimo lahko, da impedančna spektroskopija omogoča določitve velikosti izbranih prispevkov k notranji upornosti Li–S akumulatorskega sistema. To lahko po opravljeni podrobni analizi odzivov poenostavljenih simetričnih celic uporabimo za direktno študijo odzivov akumulatorjev.

Fizikalno–kemijske lastnosti elektrolita (viskoznost, gostota, specifična prevodnost, topnost polisulfidnih zvrsti) znatno vplivajo na delovanje litij–žveplovih akumulatorjev.

To hipotezo smo raziskali s študijo elektrolitskega sistema sestavljenega iz ionske tekočine [DEME][TFSI], topila 1,3-dioksolan in soli LiTFSI. Pri tem smo ugotovili, da sta med njimi najpomembnejše lastnosti nizka viskoznost, slaba topnost polisulfidnih zvrsti in zadostna koncentracija  $\text{Li}^+$  ionov, kar se kaže v boljši Coulombski učinkovitosti, višji doseženi kapaciteti, nižji prenapetosti med delovanjem in manjšem nižanju kapacitete s številom ciklov praznjenja in polnjenja. V nasprotju s hipotezo na izbranem sistemu znaten vpliv gostote in specifične prevodnosti ni bil ugotovljen, vendar se je pri tem zaključku pomembno zavedati, da pri elektrolitu na osnovi ionskih tekočin k specifični prevodnosti prispeva tudi transport njenih ionov, ne samo  $\text{Li}^+$  iona, katerega transport je pomemben za delovanje izbranega akumulatorskega sistema.

Vpliv topnosti polisulfidnih zvrsti je bil dodatno testiran s pripravo elektrolita na osnovi fluoriranega etra TFEE, s katerim smo uspeli pripraviti akumulatorske celice z nižjo vsebnostjo elektrolita, višjo količino žvepla na elektrodi in večjo končno energijo. Z uporabo različnih tehnik so bile razložene spremembe v mehanizmu delovanja. Njihov vzrok je v zmanjšani topnosti polisulfidnih zvrsti, ki jo povzroči slaba solvatacija  $\text{Li}^+$  iona v fluoriranih etrih.

Kovinska litijeva anoda zaradi dendritske rasti ter posledično večanja njene površine ne prispeva bistveno k notranji upornosti Li–S akumulatorja.

K prispevku kovinske litijeve anode k notranji upornosti Li–S akumulatorja spada upornost za reakcijo prenosa naboja, difuzijo  $\text{Li}^+$  ionov do elektrode in nazaj ter kompleksen pasivni sloj na površini elektrode, permeabilen za  $\text{Li}^+$  ione.

Med praznjenjem akumulatorja se litij raztaplja v elektrolitu v obliki  $\text{Li}^+$  ionov, med polnjenjem pa se nalaga nazaj na kovinsko površino v obliki iglic (dendritov). S tem se sčasoma površina anode drastično poveča (HSAL – nastanek filma z veliko površino), zaradi česar bi sklepali, da se bo anodna upornost z večanjem števila ciklov opravljenih z akumulatorjem manjšala. Ta hipoteza velja samo v primeru zadostne količine elektrolita prisotnega v celici in uporabe nizke tokovne gostote. Ob nastajanju dendritov se namreč porabi vedno več elektrolita za pasivacijo na novo nastalega sloja kovinskega litija, nižje tokovne gostote pa so povezane z manjšim deležem dendritske rasti. Iz podobnega razloga so bile tekom raziskave ugotovljene težave pri delovanju akumulatorske celice ob uporabi fluoriranega elektrolita.

Razen tega smo skozi raziskave ugotovili še druge pomembne vplive Li anode, ki spremenijo ostale prispevke k notranji upornosti Li–S akumulatorskega sistema. Kot že omenjeno zaradi pasivacije litija izgublamo elektrolit in večamo njegovo upornost, po drugi strani pa se polisulfidi v kontaktu z litijem reducirajo in se tako spremeni tudi impedančni odziv pozitivne elektrode. Tej izgubi aktivnega materiala pripisujemo tudi največji vpliv na doseganje kapacitete manjše od teoretične.

Če povzamemo, čeprav so reakcijski in difuzijski impedančni prispevki za redoks reakcijo  $\text{Li}^+$  ionov na kovinski litijevi površini nekajkrat manjši od prispevkov procesov na katodni strani, kovinska Li anoda znatno spremeni stanje v celici preko stranskih reakcij z elektrolitom in polisulfidnimi zvrstmi, zaradi česar je hipoteza, da je njen vpliv neznaten, ovržena.

Porozna katoda iz kompozita ogljik-žveplo najznatneje prispeva k notranji upornosti baterijske celice. Razlog je med drugim tudi v procesu odlaganja neprevodnega  $\text{Li}_2\text{S}$  na površino.

Z uporabo različnih sestav celic smo uspešno razločili reakcijske in difuzijske prispevke h katodnemu impedančnemu odzivu. Spremembe teh prispevkov smo spremljali tudi čez praznjenje akumulatorja, kjer se je izkazalo, da je največji prispevek k notranji upornosti Li–S akumulatorja v difuziji polisulfidnih zvrsti do površine elektrode, iz česar zaključujemo, da je najbolj omejujoč proces v delovanju akumulatorja masni transport.

Preko spremljanja praznjenja akumulatorskih celic smo ugotovili tudi, da na spremembo notranje upornosti pomembno vpliva odlaganje filma  $\text{Li}_2\text{S}$ , vendar rezultati kažejo na to, da je zaznan efekt zaradi osiromašenja polisulfidnih zvrsti iz elektrolita in ne zaradi pasivacije površine elektrode. Na osnovi teh dognanj smo pripravili tudi novo hipotezo nastanka filma  $\text{Li}_2\text{S}$ , kjer tvorba kristalizacijskih jeder poteka po direktni elektrokemijski redukciji polisulfidov, med tem ko nadaljnja rast poteka v treh dimenzijah s pomočjo disproporcionacijskih reakcij topnih polisulfidov, ki delujejo kot redoks mediatorji.

Ti izsledki kažejo na to, da se praznjenje Li–S predčasno zaključi zaradi osiromašenja polisulfidnih zvrsti iz elektrolita, saj se le-te porabijo za tvorbo filma. Film, čeprav neprevoden, tvori porozne strukture, ki omogočajo nadaljnje reakcije, vendar je zaradi nižje koncentracije polisulfidov otežena njihova difuzija do površine elektrode. Zaradi tega naraste prenapetost čez izbrano mejno napetost in se praznjenje konča pri manj kot teoretični kapaciteti. Pomemben vpliv na ta izkoristek ima še kovinska Li anoda, saj polisulfidi, ki pridejo v stik z njeno površino reagirajo po stranskih reakcijah in jih tako izgubimo za nadaljnjo elektrokemijsko uporabo.

## 7 Literature

1. Kiehne, HA, ed.: *Battery Technology Handbook*. Second edi. New York: Marcel Dekker, Inc.; 2003.
2. Pistoia, G: *Batteries for Portable Devices*. Amsterdam: Elsevier; 2005.
3. Dell, RM; Rand, DAJ: *Understanding Batteries*. Cambridge: The Royal Society of Chemistry; 2001.
4. Linden, D; Reddy, TB: *Handbook of Batteries*. third edit. New York: McGraw-Hill; 1995.
5. Crompton, TR: *Battery Reference Book*. Third edit. Oxford: Reed Educational and Professional Publishing Ltd.; 2000.
6. Winter, M; Brodd, RJ: What are batteries, fuel cells, and supercapacitors? *Chem. Rev.*, **2004**, *104*, 4245–4269.
7. Rosenman, A; Markevich, E; Salitra, G; Aurbach, D; Garsuch, A; Chesneau, FF: Review on Li-Sulfur Battery Systems: an Integral Perspective. *Adv. Energy Mater.*, **2015**, *5*, 1500212–1500233.
8. Yin, YX; Xin, S; Guo, YG; Wan, LJ: Lithium-sulfur batteries: Electrochemistry, materials, and prospects. *Angew. Chemie - Int. Ed.*, **2013**, *52*, 13186–13200.
9. Kumaresan, K; Mikhaylik, Y; White, RE: A Mathematical Model for a Lithium–Sulfur Cell. *J. Electrochem. Soc.*, **2008**, *155*, A576–A582.
10. Dominko, R; Patel, MUM; Lapornik, V; Vizintin, A; Koželj, M; N. Tušar, N; Arčon, I; Stievano, L; Aquilanti, G: Analytical Detection of Polysulfides in the Presence of Adsorption Additives by Operando X-ray Absorption Spectroscopy. *J. Phys. Chem. C*, **2015**, *119*, 19001–19010.
11. Manthiram, A; Fu, Y; Chung, S; Zu, C; Su, Y: Rechargeable Lithium – Sulfur Batteries. *Chem. Rev.*, **2014**, *114*, 11751–11787.
12. Zhang, T; Marinescu, M; O'Neill, L; Wild, M; Offer, G: Modeling the voltage loss mechanisms in lithium-sulfur cells: the importance of electrolyte resistance and precipitation kinetics. *Phys. Chem. Chem. Phys.*, **2015**, *17*, 22581–22586.
13. Patel, MUM; Arčon, I; Aquilanti, G; Stievano, L; Mali, G; Dominko, R: X-ray absorption near-edge structure and nuclear magnetic resonance study of the lithium-sulfur battery and its components. *ChemPhysChem*, **2014**, *15*, 894–904.
14. Marinescu, M; Zhang, T; Offer, GJ: A zero dimensional model of lithium–sulfur batteries during charge and discharge. *Phys. Chem. Chem. Phys.*, **2016**, *18*, 584–593.
15. Wakihara, M; Yamamoto, O, eds.: *Lithium Ion Batteries - Fundamentals and Performance*. Weinheim: WILEY-VCH Verlag; 1998.
16. Zhang, SS: Liquid electrolyte lithium/sulfur battery: Fundamental chemistry, problems, and solutions. *J. Power Sources*, **2013**, *231*, 153–162.
17. Wei Seh, Z; Li, W; Cha, JJ; Zheng, G; Yang, Y; McDowell, MT; Hsu, P-C; Cui, Y: Sulphur–TiO<sub>2</sub> yolk–shell nanoarchitecture with internal void space for long-cycle lithium–sulphur batteries. *Nat. Commun.*, **2013**, *4*, 1331.

18. Guo, J; Xu, Y; Wang, C: Sulfur-Impregnated Disordered Carbon Nanotubes Cathode for Lithium-Sulfur Batteries. *Nano Lett.*, **2011**, *11*, 4288–4294.
19. Xu, W; Wang, J; Ding, F; Chen, X; Nasybulin, E; Zhang, Y; Zhang, J-G: Lithium metal anodes for rechargeable batteries. *Energy Environ. Sci.*, **2014**, *7*, 513–537.
20. Herbert, D; Ulam, J: Electric dry cells and storage batteries. 1962, 2–4.
21. Rao, ML.: Organic electrolyte cells. *US Pat. 3,413,154*, 1966, Nov 26.
22. Nole, DA; Moss, V: Battery Employing Lithium-Sulphur Electrodes with Non-Aqueous Electrolyte. *US Pat. 3,532,543*, 1970, 3–5.
23. Peled, E; Yamin, H: Electrochemical cell. *US Pat. 4,410,609*, 1983.
24. Rauh, RD; Abraham, KM; Pearson, GF; Surprenant, JK; Brummer, SB: A Lithium / Dissolved Sulfur Battery with an Organic Electrolyte. *J. Electrochem. Soc.*, **1979**, *126*, 525–527.
25. Yamin, H; Gorenstein, A; Penciner, J; Sternberg, Y; Peled, E: Lithium Sulfur Battery - Oxidation/Reduction Mechanisms of Polysulfides in THF Solutions. *J. Electrochem. Soc.*, **1988**, *135*, 1045–1048.
26. Peled, E; Sternberg, Y; Gorenstein, A; Lavi, Y: Lithium-Sulfur Battery : Evaluation of Dioxolane-Based Electrolytes. *J. Electrochem. Soc.*, **1989**, *136*, 2–6.
27. Peled, E; Gorenstein, A; Segal, M; Sternberg, Y: Rechargeable lithium-sulfur battery (extended abstract). *J. Power Sources*, **1989**, *26*, 269–271.
28. Marmorstein, D; Yu, TH; Striebel, KA; McLarnon, FR; Hou, J; Cairns, EJ: Electrochemical performance of lithium/sulfur cells with three different polymer electrolytes. *J. Power Sources*, **2000**, *89*, 219–226.
29. Jeon, BH; Yeon, JH; Kim, KM; Chung, IJ: Preparation and electrochemical properties of lithium–sulfur polymer batteries. *J. Power Sources*, **2002**, *109*, 89–97.
30. Wang, J; Yang, J; Xie, J; Xu, N: A Novel Conductive Polymer-Sulfur Composite Cathode Material for Rechargeable Lithium Batteries. *Adv. Mater.*, **2002**, *14*, 963–965.
31. Chang, DR; Lee, SH; Kim, SW; Kim, HT: Binary electrolyte based on tetra(ethylene glycol) dimethyl ether and 1,3-dioxolane for lithium-sulfur battery. *J. Power Sources*, **2002**, *112*, 452–460.
32. Shin, JH; Kim, KW; Ahn, HJ; Ahn, JH: Electrochemical properties and interfacial stability of (PEO)<sub>10</sub>LiCF<sub>3</sub>SO<sub>3</sub>–Ti<sub>n</sub>O<sub>2n-1</sub> composite polymer electrolytes for lithium/sulfur battery. *Mater. Sci. Eng. B*, **2002**, *95*, 148–156.
33. Web of Science [v.5.25] - Result Analysis for “Lithium - sulfur battery.”
34. Vizintin, A; Chabanne, L; Tchernychova, E; Arčon, I; Stievano, L; Aquilanti, G; Antonietti, M; Fellingner, TP; Dominko, R: The mechanism of Li<sub>2</sub>S activation in lithium-sulfur batteries: Can we avoid the polysulfide formation? *J. Power Sources*, **2017**, *344*, 208–217.
35. Wang, C; Wang, X; Yang, Y; Kushima, A; Chen, J; Huang, Y; Li, J: Slurryless Li<sub>2</sub>S/Reduced Graphene Oxide Cathode Paper for High-Performance Lithium Sulfur Battery. *Nano Lett.*, **2015**, *15*, 1796–1802.

36. Meini, S; Elazari, R; Rosenman, A; Garsuch, A; Aurbach, D: The use of redox mediators for enhancing utilization of Li<sub>2</sub>S cathodes for advanced Li-S battery systems. *J. Phys. Chem. Lett.*, **2014**, *5*, 915–918.
37. Wu, F; Lee, JT; Zhao, E; Zhang, B; Yushin, G: Graphene–Li<sub>2</sub>S–Carbon Nanocomposite for Lithium–Sulfur Batteries. *ACS Nano*, **2016**, *10*, 1333–1340.
38. Pan, F; Wang, Q: Redox species of redox flow batteries: A review. *Molecules*, **2015**, *20*, 20499–20517.
39. Fan, FY; Woodford, WH; Li, Z; Baram, N; Smith, KC; Helal, A; McKinley, GH; Carter, WC; Chiang, Y-M: Polysulfide Flow Batteries Enabled by Percolating Nanoscale Conductor Networks. *Nano Lett.*, **2014**, *14*, 2210–2218.
40. Li, J; Yang, L; Yang, S; Lee, JY: The Application of Redox Targeting Principles to the Design of Rechargeable Li-S Flow Batteries. *Adv. Energy Mater.*, **2015**, *5*, 1501808.
41. Borchardt, L; Oschatz, M; Kaskel, S: Carbon Materials for Lithium Sulfur Batteries - Ten Critical Questions. *Chem. - A Eur. J.*, **2016**, *22*, 7324–7351.
42. Zheng, S; Chen, Y; Xu, Y; Yi, F; Zhu, Y; Liu, Y; Yang, J; Wang, C: *In Situ* Formed Lithium Sulfide/Microporous Carbon Cathodes for Lithium-Ion Batteries. *ACS Nano*, **2013**, *7*, 10995–11003.
43. Zhang, F; Zhang, X; Dong, Y; Wang, L; Li, L; Chen, S; Zhao, T; Nie, Z; Saraf, L V.; Aksay, IA; Liu, J; Zhang, JG: Facile and effective synthesis of reduced graphene oxide encapsulated sulfur via oil/water system for high performance lithium sulfur cells. *J. Mater. Chem.*, **2012**, *22*, 11452.
44. Song, M-S; Han, S-C; Kim, H-S; Kim, J-H; Kim, K-T; Kang, Y-M; Ahn, H-J; Dou, SX; Lee, J-Y: Effects of Nanosized Adsorbing Material on Electrochemical Properties of Sulfur Cathodes for Li/S Secondary Batteries. *J. Electrochem. Soc.*, **2004**, *151*, A791–A795.
45. Ji, L; Rao, M; Zheng, H; Zhang, L; Li, Y; Duan, W; Guo, J; Cairns, EJ; Zhang, Y: Graphene Oxide as a Sulfur Immobilizer in High Performance Lithium/Sulfur Cells. *J. Am. Chem. Soc.*, **2011**, *133*, 18522–18525.
46. Ji, X; Lee, KT; Nazar, LF: A highly ordered nanostructured carbon–sulphur cathode for lithium–sulphur batteries. *Nat. Mater.*, **2009**, *8*, 500–506.
47. Ahn, W; Kim, K-B; Jung, K-N; Shin, K-H; Jin, C-S: Synthesis and electrochemical properties of a sulfur-multi walled carbon nanotubes composite as a cathode material for lithium sulfur batteries. *J. Power Sources*, **2012**, *202*, 394–399.
48. Rao, M; Song, X; Cairns, EJ: Nano-carbon/sulfur composite cathode materials with carbon nanofiber as electrical conductor for advanced secondary lithium/sulfur cells. *J. Power Sources*, **2012**, *205*, 474–478.
49. Li, N; Zheng, M; Lu, H; Hu, Z; Shen, C; Chang, X; Ji, G; Cao, J; Shi, Y: High-rate lithium–sulfur batteries promoted by reduced graphene oxide coating. *Chem. Commun.*, **2012**, *48*, 4106–4108.
50. Wang, H; Yang, Y; Liang, Y; Robinson, JT; Li, Y; Jackson, A; Cui, Y; Dai, H: Graphene-Wrapped Sulfur Particles as a Rechargeable Lithium–Sulfur Battery Cathode Material with High Capacity and Cycling Stability. *Nano Lett.*, **2011**, *11*, 2644–2647.

51. Ji, X; Evers, S; Black, R; Nazar, LF: Stabilizing lithium–sulphur cathodes using polysulphide reservoirs. *Nat. Commun.*, **2011**, *2*, 325–331.
52. Evers, S; Yim, T; Nazar, LF: Understanding the Nature of Absorption/Adsorption in Nanoporous Polysulfide Sorbents for the Li–S Battery. *J. Phys. Chem. C*, **2012**, *116*, 19653–19658.
53. Kang, SH; Zhao, X; Manuel, J; Ahn, HJ; Kim, KW; Cho, KK; Ahn, JH: Effect of sulfur loading on energy density of lithium sulfur batteries. *Phys. Status Solidi Appl. Mater. Sci.*, **2014**, *211*, 1895–1899.
54. Cheon, S-E; Ko, K-S; Cho, J-H; Kim, S-W; Chin, E-Y; Kim, H-T: Rechargeable Lithium Sulfur Battery - ii. Rate Capability and Cycle Characteristics. *J. Electrochem. Soc.*, **2003**, *150*, A800.
55. Zhou, K; Fan, XJ; Wei, XF; Liu, JH: The strategies of advanced cathode composites for lithium-sulfur batteries. *Sci. China Technol. Sci.*, **2017**, *60*, 175–185.
56. Li, Z; Huang, J; Yann Liaw, B; Metzler, V; Zhang, J: A review of lithium deposition in lithium-ion and lithium metal secondary batteries. *J. Power Sources*, **2014**, *254*, 168–182.
57. Liang, X; Pang, Q; Kochetkov, IR; Sempere, MS; Huang, H; Sun, X; Nazar, LF: A facile surface chemistry route to a stabilized lithium metal anode. *Nat. Energy*, **2017**, *6*, 17119.
58. Zheng, G; Wang, C; Pei, A; Lopez, J; Shi, F; Chen, Z; Sendek, AD; Lee, H-W; Lu, Z; Schneider, H; Safont-Sempere, MM; Chu, S; Bao, Z; Cui, Y: High-Performance Lithium Metal Negative Electrode with a Soft and Flowable Polymer Coating. *ACS Energy Lett.*, **2016**, *1*, 1247–1255.
59. Ding, F; Xu, W; Graff, GL; Zhang, J-GJ; Sushko, ML; Chen, X; Shao, Y; Engelhard, MH; Nie, Z; Xiao, J; Liu, X; Sushko, P V.; Liu, J; Zhang, J-GJ: Dendrite-Free Lithium Deposition via Self-Healing Electrostatic Shield Mechanism. *J. Am. Chem. Soc.*, **2013**, *135*, 4450–4456.
60. Choudhury, S; Archer, LA: Lithium Fluoride Additives for Stable Cycling of Lithium Batteries at High Current Densities. *Adv. Electron. Mater.*, **2016**, *2*, 1500246.
61. Zhang, K; Lee, GH; Park, M; Li, W; Kang, YM: Recent Developments of the Lithium Metal Anode for Rechargeable Non-Aqueous Batteries. *Adv. Energy Mater.*, **2016**, *6*, 1–14.
62. Xu, K: Nonaqueous liquid electrolytes for lithium-based rechargeable batteries. *Chem. Rev.*, **2004**, *104*, 4303–4417.
63. Park, J; Ueno, K; Tachikawa, N; Dokko, K; Watanabe, M: Ionic Liquid Electrolytes for Lithium-Sulfur Batteries. *J. Phys. Chem. C*, **2013**, *117*, 20531–20541.
64. Scheers, J; Fantini, S; Johansson, P: A review of electrolytes for lithium–sulphur batteries. *J. Power Sources*, **2014**, *255*, 204–218.
65. Barghamadi, M; Best, AS; Bhatt, AI; Hollenkamp, AF; Musameh, M; Rees, RJ; Rüther, T: Lithium-Sulfur Batteries- the solution is in the electrolyte, but is the electrolyte a solution? *Energy Environ. Sci.*, **2014**, *7*, 3902–3920.
66. Zhang, S; Ueno, K; Dokko, K; Watanabe, M: Recent Advances in Electrolytes for Lithium-

- Sulfur Batteries. *Adv. Energy Mater.*, **2015**, *5*, 1500117.
67. Chen, R; Qu, W; Guo, X; Li, L; Wu, F: The pursuit of solid-state electrolytes for lithium batteries: from comprehensive insight to emerging horizons. *Mater. horizons*, **2016**, *3*, 487–516.
68. Dirlam, PT; Glass, RS; Char, K; Pyun, J: The use of polymers in Li-S batteries: A review. *J. Polym. Sci. Part A Polym. Chem.*, **2017**, *55*, 1635–1668.
69. Osada, I; de Vries, H; Scrosati, B; Passerini, S: Ionic-Liquid-Based Polymer Electrolytes for Battery Applications. *Angew. Chemie - Int. Ed.*, **2015**, 500–513.
70. Lee, YM; Choi, N-S; Park, JH; Park, J-K: Electrochemical performance of lithium/sulfur batteries with protected Li anodes. *J. Power Sources*, **2003**, *119*, 964–972.
71. Mikhaylik, Y V.; Kovalev, I; Schock, R; Kumaresan, K; Xu, J; Affinito, J: High Energy Rechargeable Li-S Cells for EV Application: Status, Remaining Problems and Solutions. In: *ECS Transactions*. Vol 25. The Electrochemical Society; 2010:23–34.
72. Mikhaylik, Y V.: Electrolytes for Li-S cells. *US Pat. 7,354,680*, 2008.
73. Aurbach, D; Pollak, E; Elazari, R; Salitra, G; Kelley, CS; Affinito, J: On the Surface Chemical Aspects of Very High Energy Density, Rechargeable Li-Sulfur Batteries. *J. Electrochem. Soc.*, **2009**, *156*, A694–A702.
74. Lin, Z; Liu, Z; Fu, W; Dudney, NJ; Liang, C: Phosphorous pentasulfide as a novel additive for high-performance lithium-sulfur batteries. *Adv. Funct. Mater.*, **2013**, *23*, 1064–1069.
75. Gerber, LCH; Frischmann, PD; Fan, FY; Doris, SE; Qu, X; Scheuermann, AM; Persson, K; Chiang, Y-M; Helms, BA: Three-Dimensional Growth of Li<sub>2</sub>S in Lithium–Sulfur Batteries Promoted by a Redox Mediator. *Nano Lett.*, **2016**, *16*, 549–554.
76. Zhang, SS: Improved Cyclability of Liquid Electrolyte Lithium/Sulfur Batteries by Optimizing Electrolyte/Sulfur Ratio. *Energies*, **2012**, *5*, 5190–5197.
77. Hagen, M; Fanz, P; Tübke, J: Cell energy density and electrolyte/sulfur ratio in Li-S cells. *J. Power Sources*, **2014**, *264*, 30–34.
78. Vizintin, A; Patel, MUM; Genorio, B; Dominko, R: Effective Separation of Lithium Anode and Sulfur Cathode in Lithium-Sulfur Batteries. *ChemElectroChem*, **2014**, *1*, 1040–1045.
79. Su, Y-S; Manthiram, A: Lithium–sulphur batteries with a microporous carbon paper as a bifunctional interlayer. *Nat. Commun.*, **2012**, *3*, 1166–1171.
80. Yuan, L; Qiu, X; Chen, L; Zhu, W: New insight into the discharge process of sulfur cathode by electrochemical impedance spectroscopy. *J. Power Sources*, **2009**, *189*, 127–132.
81. Kolosnitsyn, VS; Kuzmina, E V.; Karaseva, E V.; Mochalov, SE: A study of the electrochemical processes in lithium-sulphur cells by impedance spectroscopy. *J. Power Sources*, **2011**, *196*, 1478–1482.
82. Barchasz, C; Leprêtre, JC; Alloin, F; Patoux, S: New insights into the limiting parameters of the Li/S rechargeable cell. *J. Power Sources*, **2012**, *199*, 322–330.
83. Deng, Z; Zhang, Z; Lai, Y; Liu, J; Li, J; Liu, Y: Electrochemical Impedance Spectroscopy

- Study of a Lithium/Sulfur Battery: Modeling and Analysis of Capacity Fading. *J. Electrochem. Soc.*, **2013**, *160*, A553–A558.
84. Canas, NA; Hirose, K; Pascucci, B; Wagner, N; Friedrich, KA; Hiesgen, R: Investigations of lithium-sulfur batteries using electrochemical impedance spectroscopy. *Electrochim. Acta*, **2013**, *97*, 42–51.
  85. Risse, S; Canas, NA; Wagner, N; Härk, E; Ballauff, M; Friedrich, KA: Correlation of capacity fading processes and electrochemical impedance spectra in lithium/sulfur cells. *J. Power Sources*, **2016**, *323*, 107–114.
  86. Fronczek, DN; Bessler, WG: Insight into lithium-sulfur batteries: Elementary kinetic modeling and impedance simulation. *J. Power Sources*, **2013**, *244*, 183–188.
  87. Ganesan, A; Varzi, A; Passerini, S; Shaijumon, MM: Graphene derived carbon confined sulfur cathodes for lithium-sulfur batteries: Electrochemical impedance studies. *Electrochim. Acta*, **2016**, *214*, 129–138.
  88. Kazazi, M; Vaezi, MR; Kazemzadeh, A: Enhanced rate performance of polypyrrole-coated sulfur/MWCNT cathode material: A kinetic study by electrochemical impedance spectroscopy. *Ionics (Kiel)*, **2014**, *20*, 635–643.
  89. Peled, E; Menkin, S: Review—SEI: Past, Present and Future. *J. Electrochem. Soc.*, **2017**, *164*, A1703–A1719.
  90. Walus, S: Accumulateur Lithium / Soufre : développement et compréhension des mécanismes électrochimiques. 2015.
  91. Bieker, G; Winter, M; Bieker, P: Electrochemical in situ investigations of SEI and dendrite formation on the lithium metal anode. *Phys. Chem. Chem. Phys.*, **2015**, *17*, 8670–8679.
  92. Cheng, X-B; Zhang, R; Zhao, C-Z; Wei, F; Zhang, J-G; Zhang, Q: A Review of Solid Electrolyte Interphases on Lithium Metal Anode. *Adv. Sci.*, **2016**, *3*, n/a-n/a.
  93. Crowther, O; West, AC: Effect of Electrolyte Composition on Lithium Dendrite Growth. *J. Electrochem. Soc.*, **2008**, *115*, A806–A811.
  94. Patel, MUM; Demir-Cakan, R; Morcrette, M; Tarascon, JM; Gaberscek, M; Dominko, R: Li-S battery analyzed by UV/vis in operando mode. *ChemSusChem*, **2013**, *6*, 1177–1181.
  95. Patel, MUM; Dominko, R: Application of in operando UV/Vis spectroscopy in lithium-sulfur batteries. *ChemSusChem*, **2014**, *7*, 2167–2175.
  96. Aquilanti, G; Giorgetti, M; Dominko, R; Stievano, L; Arčon, I; Novello, N; Olivi, L: *Operando* characterization of batteries using x-ray absorption spectroscopy: advances at the beamline XAFS at synchrotron Elettra. *J. Phys. D. Appl. Phys.*, **2017**, *50*, 74001.
  97. Barsoukov, E; Macdonald, JR: *Impedance Spectroscopy Theory, Experiment, and Applications*. second edi. Wiley & Sons, Inc.; 2005.
  98. Denuault, G; Sosna, M; Williams, K-J: Classical Experiments. In: Zoski CG, ed. *Handbook of Electrochemistry*. Amsterdam: Elsevier; 2007:431–469.
  99. Wang, J: *Analytical Electrochemistry*. second edi. Hoboken: John Wiley & Sons; 2006.
  100. Barthel, J; Wachter, R; Gores, H-J: Temperature Dependence of Electrolyte

- Conductance in Non-Aqueous Solutions. In: Conway BE, Bockris JO, eds. *Modern Aspects of Electrochemistry*. New York: Plenum press; 1979:1–78.
101. Barthel, J; Feuerlein, F; Neueder, R; Watcher, R: Calibration of Conductance Cells at Various Temperatures. *J. Solut. Chem.*, **1980**, *9*, 209–2019.
  102. Bešter-Rogač, M; Habe, D: Modern Advances in Electrical Conductivity Measurements of Solutions. *Acta Chim. Slov.*, **2006**, *53*, 391–395.
  103. Ravel, B; Newville, M: ATHENA, ARTEMIS, HEPHAESTUS: Data analysis for X-ray absorption spectroscopy using IFEFFIT. *J. Synchrotron Radiat.*, **2005**, *12*, 537–541.
  104. Drvarič Talian, S; Moškon, J; Dominko, R; Gaberšček, M: Reactivity and Diffusivity of Li Polysulfides: A Fundamental Study Using Impedance Spectroscopy. *ACS Appl. Mater. Interfaces*, **2017**, *9*, 29760–29770.
  105. Drvarič Talian, S; Bešter-Rogač, M; Dominko, R: The physicochemical properties of a [DEME][TFSI] ionic liquid-based electrolyte and its influence on the performance of lithium–sulfur batteries. *Electrochim. Acta*, **2017**, *252*, 147–153.
  106. Levine, I: Electrical conductivity of electrolyte solutions. In: *Physical Chemistry*. sixth edit. Boston: McGraw-Hill; 2009:496–497.
  107. Suo, L; Hu, Y-S; Li, H; Armand, M; Chen, L: A new class of Solvent-in-Salt electrolyte for high-energy rechargeable metallic lithium batteries. *Nat. Commun.*, **2013**, *4*, 1481.
  108. Shin, ES; Kim, K; Oh, SH; Cho, W II: Polysulfide dissolution control: the common ion effect. *Chem. Commun.*, **2013**, *49*, 2004–2006.
  109. Broadhead, J; Kuo, HC: Electrochemical principles and reactions. In: Linden D, Reddy TB, eds. *Handbook of Batteries*. third edit. New York: McGraw-Hill; 2002:2.1.
  110. Cheng, L; Curtiss, LA; Zavadil, KR; Gewirth, AA; Shao, Y; Gallagher, KG: Sparingly Solvating Electrolytes for High Energy Density Lithium–Sulfur Batteries. *ACS Energy Lett.*, **2016**, *1*, 503–509.
  111. Gu, S; Qian, R; Jin, J; Wang, Q; Guo, J; Zhang, S; Zhuo, S; Wen, Z: Suppressing the dissolution of polysulfides with cosolvent fluorinated diether towards high-performance lithium sulfur batteries. *Phys. Chem. Chem. Phys.*, **2016**, *18*, 29293–29299.
  112. Azimi, N; Xue, Z; Bloom, I; Gordin, ML; Wang, D; Daniel, T; Takoudis, C; Zhang, Z: Understanding the effect of a fluorinated ether on the performance of lithium-sulfur batteries. *ACS Appl. Mater. Interfaces*, **2015**, *7*, 9169–9177.
  113. Cuisinier, M; Cabelguen, P-E; Adams, BD; Garsuch, A; Balasubramanian, M; Nazar, LF: Unique behaviour of nonsolvents for polysulphides in lithium–sulphur batteries. *Energy Environ. Sci.*, **2014**, *7*, 2697–2705.
  114. Lee, CW; Pang, Q; Ha, S; Cheng, L; Han, SD; Zavadil, KR; Gallagher, KG; Nazar, LF; Balasubramanian, M: Directing the Lithium-Sulfur Reaction Pathway via Sparingly Solvating Electrolytes for High Energy Density Batteries. *ACS Cent. Sci.*, **2017**, *3*, 605–613.
  115. Drvarič Talian, S; Jeschke, S; Vizintin, A; Pirnat, K; Arčon, I; Aquilanti, G; Johansson, P; Dominko, R: Fluorinated Ether Based Electrolyte for High-Energy Lithium–Sulfur

- Batteries: Li<sup>+</sup> Solvation Role Behind Reduced Polysulfide Solubility. *Chem. Mater.*, **2017**, *29*, 10037–10044.
116. Klamt, A: Conductor-like Screening Model for Real Solvents: A New Approach to the Quantitative Calculation of Solvation Phenomena. *J. Phys. Chem.*, **1995**, *99*, 2224–2235.
  117. Klamt, A; Eckert, F: COSMO-RS: a novel and efficient method for the a priori prediction of thermophysical data of liquids. *Fluid Phase Equilib.*, **2000**, *172*, 43–72.
  118. Klamt, A: The COSMO and COSMO-RS solvation models. *Wiley Interdiscip. Rev. Comput. Mol. Sci.*, **2011**, *1*, 699–709.
  119. Klamt, A: COSMO-RS for aqueous solvation and interfaces. *Fluid Phase Equilib.*, **2016**, *407*, 152–158.
  120. Rey, I; Johansson, P; Lindgren, J; Lassègues, JC; Grondin, J; Servant, L: Spectroscopic and Theoretical Study of (CF<sub>3</sub>SO<sub>2</sub>)<sub>2</sub>N<sup>-</sup> (TFSI<sup>-</sup>) and (CF<sub>3</sub>SO<sub>2</sub>)<sub>2</sub>NH (HTFSI). *J. Phys. Chem. A*, **1998**, *102*, 3249–3258.
  121. Conder, J; Villevieille, C; Trabesinger, S; Novák, P; Gubler, L; Bouchet, R: Electrochemical impedance spectroscopy of a Li–S battery: Part 1. Influence of the electrode and electrolyte compositions on the impedance of symmetric cells. *Electrochim. Acta*, 2017.
  122. Schranzhofer, H; Bugajski, J; Santner, HJ; Korepp, C; Möller, KC; Besenhard, JO; Winter, M; Sitte, W: Electrochemical impedance spectroscopy study of the SEI formation on graphite and metal electrodes. *J. Power Sources*, **2006**, *153*, 391–395.
  123. Woo, J-J; Maroni, VA; Liu, G; Vaughey, JT; Gosztola, DJ; Amine, K; Zhang, Z: Symmetrical Impedance Study on Inactivation Induced Degradation of Lithium Electrodes for Batteries Beyond Lithium-Ion. *J. Electrochem. Soc.*, **2014**, *161*, A827–A830.
  124. Lowe, MA; Gao, J; Abruña, HD: Mechanistic insights into operational lithium–sulfur batteries by in situ X-ray diffraction and absorption spectroscopy. *RSC Adv.*, **2014**, *4*, 18347.
  125. Rauh, RD; Shuker, FS; Marston, JM; Brummer, SB: Formation of lithium polysulfides in aprotic media. *J. Inorg. Nucl. Chem.*, **1977**, *39*, 1761–1766.
  126. Vetter, KJ: *Electrochemical Kinetics: Theoretical Aspects*. revised ed. Elsevier; 2013.
  127. Thorat, I V.; Stephenson, DE; Zacharias, NA; Zaghbi, K; Harb, JN; Wheeler, DR: Quantifying tortuosity in porous Li-ion battery materials. *J. Power Sources*, **2009**, *188*, 592–600.
  128. Fan, FY; Carter, WC; Chiang, Y-M: Mechanism and Kinetics of Li<sub>2</sub>S Precipitation in Lithium-Sulfur Batteries. *Adv. Mater.*, **2015**, *27*, 5203–5209.
  129. Fan, FY; Chiang, Y-M: Electrodeposition Kinetics in Li-S Batteries: Effects of Low Electrolyte/Sulfur Ratios and Deposition Surface Composition. *J. Electrochem. Soc.*, **2017**, *164*, A917–A922.
  130. Yan, J; Liu, X; Li, B: Capacity fade analysis of sulfur cathodes in lithium– sulfur batteries. *Adv. Sci.*, **2016**, *3*.
  131. Liu, Z; Mukherjee, PP: Mesoscale Elucidation of Surface Passivation in the Li-Sulfur Battery Cathode. *ACS Appl. Mater. Interfaces*, **2017**, *9*, 5263–5271.

132. Lang, SY; Shi, Y; Guo, YG; Wang, D; Wen, R; Wan, LJ: Insight into the Interfacial Process and Mechanism in Lithium–Sulfur Batteries: An In Situ AFM Study. *Angew. Chemie - Int. Ed.*, **2016**, *55*, 15835–15839.
133. Busche, MR; Adelhelm, P; Sommer, H; Schneider, H; Leitner, K; Janek, J: Systematical electrochemical study on the parasitic shuttle-effect in lithium-sulfur-cells at different temperatures and different rates. *J. Power Sources*, **2014**, *259*, 289–299.
134. Demir-Cakan, R; Morcrette, M; Gangulibabu; Guéguen, A; Dedryvère, R; Tarascon, J-M: Li–S batteries: simple approaches for superior performance. *Energy Environ. Sci.*, **2013**, *6*, 176.
135. Noh, H; Song, J; Park, J-K; Kim, H-T: A new insight on capacity fading of lithium–sulfur batteries: The effect of Li<sub>2</sub>S phase structure. *J. Power Sources*, **2015**, *293*, 329–335.
136. Waluś, S; Barchasz, C; Bouchet, R; Martin, JF; Leprêtre, JC; Alloin, F: Investigation of non-woven carbon paper as a current collector for sulfur positive electrode—Understanding of the mechanism and potential applications for Li/S batteries. *Electrochim. Acta*, **2016**, *211*, 697–703.
137. Xu, R; Lu, J; Amine, K: Progress in Mechanistic Understanding and Characterization Techniques of Li-S Batteries. *Adv. Energy Mater.*, **2015**, *5*, 1–22.
138. Thangavel, V; Xue, K-H; Mammeri, Y; Quiroga, M; Mastouri, A; Guéry, C; Johansson, P; Morcrette, M; Franco, AA: A Microstructurally Resolved Model for Li-S Batteries Assessing the Impact of the Cathode Design on the Discharge Performance. *J. Electrochem. Soc.*, **2016**, *163*, A2817–A2829.
139. Peng, HJ; Zhang, G; Chen, X; Zhang, ZW; Xu, WT; Huang, JQ; Zhang, Q: Enhanced Electrochemical Kinetics on Conductive Polar Mediators for Lithium–Sulfur Batteries. *Angew. Chemie - Int. Ed.*, **2016**, *55*, 12990–12995.
140. Kim, KR; Lee, K-S; Ahn, C-Y; Yu, S-H; Sung, Y-E: Discharging a Li-S battery with ultra-high sulphur content cathode using a redox mediator. *Sci. Rep.*, **2016**, *6*, 32433.
141. Hart, CJ; Cuisinier, M; Liang, X; Kundu, D; Garsuch, A; Nazar, LF: Rational design of sulphur host materials for Li–S batteries: correlating lithium polysulphide adsorptivity and self-discharge capacity loss. *Chem. Commun.*, **2015**, *51*, 2308–2311.
142. Kolosnitsyn, VS; Kuzmina, E V.; Mochalov, SE: Determination of lithium sulphur batteries internal resistance by the pulsed method during galvanostatic cycling. *J. Power Sources*, **2014**, *252*, 28–34.

## 8 List of figures

Figure 1: Battery operation during a) discharge and b) charge. ....	2
Figure 2: Stages of discharge of Li–S battery. Yellow, red and orange circles represent sulfur and different length polysulfide species. Grey circles represent $\text{Li}^+$ ions formed by Li stripping. ....	8
Figure 3: Schematic depiction of Li-S battery during charge with solid sulfur and $\text{Li}_2\text{S}$ forming on the cathode and lithium dendrites on the anode. Yellow, red and orange circles represent sulfur and different length polysulfide species. Grey circles represent $\text{Li}^+$ ions in solution and Li atoms deposited in dendritic form. ....	8
Figure 4: Insulating nature of the final discharge product can cause clogging of the available positive electrode surface area. Yellow, red and orange circles represent sulfur and different length polysulfide species. Grey circles represent $\text{Li}^+$ ions formed by Li stripping. ....	9
Figure 5: Polysulfide redox shuttle phenomenon. Yellow, red and orange circles represent sulfur and different length polysulfide species. Grey circles represent $\text{Li}^+$ ions formed by Li stripping. ....	9
Figure 6: Self-discharge phenomenon in Li–S batteries due to dissolution of sulfur from the cathode. Yellow, red and orange circles represent sulfur and different length polysulfide species. Grey circles represent $\text{Li}^+$ ions. ....	10
Figure 7: Dendritic growth of lithium during charging. Yellow, red and orange circles represent sulfur and different length polysulfide species. Grey circles represent $\text{Li}^+$ ions in solution and Li atoms deposited in dendritic form. ....	10
Figure 8: Number of scientific reports on Li–S batteries through the years (Web of science analysis conducted on the 15 <sup>th</sup> of May 2018 with the search query "lithium-sulfur battery"). <sup>33</sup> ....	11
Figure 9: An example of a simple impedance spectrum in Nyquist plot representation with its equivalent circuit model. ....	21
Figure 10: Voltage curve during one cycle of impedance spectra measurement at different DOD. Insert shows three parts of the program during discharge – green is the galvanostatic period, red relaxation time and blue PEIS measurement. ....	26
Figure 11: Specific discharge capacities and Coulombic efficiencies through 50 cycles of the experiment with intermittent impedance spectra measurements. ....	27
Figure 12: A typical impedance spectrum of a Li-S battery cell (sulfolane based electrolyte) in the first cycle at app. 50% DOD (white circles). Fit (red circles) with the equivalent circuit model shown. Reprinted with permission from reference <sup>104</sup> . Copyright 2017 American Chemical Society. ....	28
Figure 13: Resistive intercept change through the first cycle for the three electrolytes tested. ....	29
Figure 14: Resistive intercept change through 50 cycles at different DOD for three different electrolytes – a) 1 M LiTFSI in sulfolane:DOL 1:1, b) 1 M LiTFSI in TEGDME:DOL 2:1 and c) 1 M LiTFSI in [DEME][TFSI]:DOL 1:2. ....	30

Figure 15: Physicochemical properties of [DEME][TFSI]:DOL mixtures without LiTFSI salt at different molar ratios and temperatures a) conductivity, b) dynamic viscosity, c) density. ....	31
Figure 16: Physicochemical properties of [DEME][TFSI]:DOL:LiTFSI mixtures at 298.15 K a) conductivity, b) dynamic viscosity, c) density. ....	34
Figure 17: Conductance of the electrolyte mixtures determined from resistive intercept measurements a) freshly assembled battery cells with no polysulfides dissolved, b) after the 10 <sup>th</sup> charge. Concentration of the LiTFSI salt varied from 0.1 to 1.0 M and the X([DEME][TFSI]) between 0.1, 0.2, and 0.4. ....	36
Figure 18: Coulombic efficiencies over 100 cycles. a-c shows a comparison of mixtures with the same ionic liquid molar content and different concentrations of LiTFSI salt with a) X=0.101, b) X=0.199, c) X=0.401. d-f show the comparison of performance of electrolytes with the same LiTFSI concentration with d) 0.1 M LiTFSI, e) 0.5 M LiTFSI, f) 1.0 M LiTFSI. X represents the molar ratio of [DEME][TFSI] in its mixture with DOL. ....	37
Figure 19: Overpotentials over 100 cycles: a-c show a comparison of mixtures with the same ionic liquid molar content and different concentrations of LiTFSI salt with a) X=0.101, b) X=0.199, c) X=0.401; d-f show the comparison of performance of electrolytes with the same LiTFSI concentration with d) 0.1 M LiTFSI, e) 0.5 M LiTFSI, f) 1.0 M LiTFSI. X represents the molar ratio of [DEME][TFSI] in its mixture with DOL. ....	38
Figure 20: Impedance spectra for charged battery cells after 10 cycles of use, comparison of different lithium salt concentrations in the same compositions of dioxolane and ionic liquid: a) X=0.101, b) X=0.199, c) X=0.401 (Insets show the high frequency regions of the spectra). X represents the molar ratio of [DEME][TFSI] in its mixture with DOL. ....	38
Figure 21: Specific discharge capacities trend over 100 cycles: a-c show a comparison of mixtures with the same ionic liquid molar content and different concentrations of LiTFSI salt with a) X=0.101, b) X=0.199, c) X=0.401; d-f show the comparison of performance of electrolytes with the same LiTFSI concentration with d) 0.1 M LiTFSI, e) 0.5 M LiTFSI, f) 1.0 M LiTFSI. X represents the molar ratio of [DEME][TFSI] in its mixture with DOL. ....	39
Figure 22: Electrochemical performance of TFEE based electrolyte compared to a conventionally used TEGDME based one a) capacity and coulombic efficiency at different C-rates, b) voltage profile in the 50 <sup>th</sup> cycle. Solvent ratio was kept to 1:1 (v:v). ....	41
Figure 23: GITT experiment comparison a) Li–S cell with 1 M LiTFSI TFEE:DOL 1:1 (v:v). Electrode loading was 3.8 mg S cm <sup>-2</sup> , 6.5 μL of electrolyte per mg S was used and one layer of Celgard 2400 separator. b) Li – S cell with the “traditional” electrolyte composition 1 M LiTFSI in TEGDME:DOL 1:1 (v:v). Setup was similar as with a) with the exception of electrolyte amount (15 μL of electrolyte per mg S) and GITT setting (current stopped every 30 minutes). ....	41
Figure 24: Cycling behavior at for electrolytes prepared from different mixtures of TFEE and DOL –1:2; 1:1; 2:1 (all v:v mixtures with 1 M LiTFSI) a) discharge capacity and coulombic efficiency during 100 cycles of use, b) charge and discharge voltage profiles for 2 <sup>nd</sup> , 50 <sup>th</sup> and 100 <sup>th</sup> cycle of use. ....	42

Figure 25: Discharge capacity and Coulombic efficiency for a high energy Li–S cell with 6.5 $\mu\text{L}$ per mg S and 10 $\mu\text{L}$ per mg S of 1 M LiTFSI TFEE:DOL 1:1 electrolyte. Sulfur loading was 4 mg $\text{cm}^{-2}$ .....	43
Figure 26: Post mortem analysis on the high energy Li-S battery cell, a) side of the anode which was facing away from the separator, b) Li surface after cycling, c) Celgard 2400 separator with the cathode facing side, d) Celgard 2400 separator with the anode facing side .....	43
Figure 27: Impedance spectra of Li   Li symmetrical cells (2 $\text{cm}^2$ ) measured at OCV over the course of 50 hours. Spectra were measured consecutively in the range of 20 kHz–10 mHz with the amplitude of 10 mV (rms), while measurements at 1 h, 15 h, 25 h, 35 h and 45 h are shown on the figure. Inset shows the high frequency part of the spectra more clearly; all arrows indicate change with time. Cells were constructed with one layer of Celgard 2400 separator and 20 $\mu\text{L}$ of chosen electrolyte. ....	44
Figure 28: ATR-IR spectra of DOL and TFEE pure solvents, their 1:1 (v:v) mixture and the solutions with LiTFSI salt. Horizontal lines indicate additional bands due to LiTFSI .....	46
Figure 29: Sulphur K-edge XANES <i>operando</i> experiment a) electrochemical discharge profile measured, b) relative amounts of determined compounds, c) <i>operando</i> sulfur K-edge XANES spectra of the Li-S battery during the first discharge. ....	47
Figure 30: Linear combination fit of the sulfur K-edge XANES spectra in the intermediate states during discharge: (a) as prepared, (b) 220 $\text{mAh g}^{-1}$ , (c) 440 $\text{mAh g}^{-1}$ , and (d) 660 $\text{mAh g}^{-1}$ . Open cycles - experiment; black line- fit with linear combination of the four reference XANES profiles plotted below. The uncertainty of each component in the linear combination fit is $\pm 1\%$ or lower. ....	48
Figure 31: UV-vis spectroscopy experiment for 1 M LiTFSI TFEE:DOL 1:1 electrolyte, a) discharge and charge profile at C/20, b) spectra change during discharge and c) spectra of standard solutions in TFEE electrolyte, .....	49
Figure 32: A schematic representation of symmetrical cells approach – two very similar discharged batteries (top) were disassembled and their parts used to construct two symmetrical cells (bottom). ....	51
Figure 33: Impedance spectra of symmetrical (orange for cathode-cathode and red for anode-anode cells) and battery cells (measured spectra in grey and calculated spectra in black). a) fresh battery, b) battery at approximately 50% DOD, c) fully discharged battery. Battery cells were constructed with 1.5 $\text{cm}^2$ size, glassy fibre GF/D separator and 60 $\mu\text{L}$ per mg S of 1 M LiTFSI in TEGDME:DOL 2:1. ....	52
Figure 34: R1 (lithium anode contribution) change through 50 cycles at different DOD for three different electrolytes – a) 1 M LiTFSI in sulfolane:DOL 1:1, b) 1 M LiTFSI in TEGDME:DOL 2:1 and c) 1 M LiTFSI in [DEME][TFSI]:DOL 1:2. ....	53
Figure 35: a) EIS spectra from 1 MHz to 1 mHz of symmetrical Li   Li cells with different catholyte compositions before stripping and deposition. b) EIS spectra for the same cells after 50 cycles of stripping and deposition. In all the figures, 1 <sup>st</sup> , 50 <sup>th</sup> and 100 <sup>th</sup> spectra are shown which corresponds to 1 h, 66 h and 130 h after cell assembly on a) and 1 h, 66 h and 130 h	

after the end of stripping and deposition experiment on b). The direction of the arrow points to the increase with time. Insets on b) show magnification of the first measured spectrum after stripping and deposition experiment. ....	54
Figure 36: Galvanostatic stripping and deposition study on Li Li symmetric cells with various polysulfide concentrations.....	56
Figure 37: Li Li impedance response evolution when no supporting Li <sup>+</sup> salt was used for catholyte preparation (Celgard 2400 separator, 10 μL of electrolyte, spectra measured with 10 mV amplitude from 1 MHz to 1 mHz except for the first spectrum where the measurement was done to 10 mHz).....	57
Figure 38: UV-vis spectra measured on Li  Li cell (a) and the corresponding discoloration of the separator from the initial state before measurements (b, green) to the final state (c, almost colourless).....	58
Figure 39: R <sub>2</sub> (middle frequency cathode resistance) change through 50 cycles at different DOD for three different electrolytes – a) 1 M LiTFSI in sulfolane:DOL 1:1, b) 1 M LiTFSI in TEGDME:DOL 2:1 and c) 1 M LiTFSI in [DEME][TFSI]:DOL 1:2. ....	59
Figure 40: R <sub>3</sub> (low frequency cathode resistance) change through 50 cycles at different DOD for three different electrolytes – a) 1 M LiTFSI in sulfolane:DOL 1:1, b) 1 M LiTFSI in TEGDME:DOL 2:1 and c) 1 M LiTFSI in [DEME][TFSI]:DOL 1:2. ....	60
Figure 41: Galvanostatic cycling of a GC Li battery cell at C/20 current. 0.1 M Li <sub>2</sub> S <sub>4</sub> in 1 M LiTFSI in TEGDME:DOL 1:1 (v:v) was employed and the capacity calculated with respect to the amount of sulfur added in the initial catholyte solution. ....	61
Figure 42: C/50 cycles with OCV relaxation periods measured on a GC catholyte ceramic membrane electrolyte Li cell. The capacity calculated is with respect to the amount of sulfur added with the initial catholyte. ....	62
Figure 43: Nyquist (a) and Bode plots (b) of impedance response of a S <sub>8</sub> <sup>2-</sup> /S <sub>7</sub> <sup>2-</sup> redox pair (both in concentration of 0.05 M, Celgard 2400 separator was used and 10 μL of electrolyte) in the frequency range of 1 MHz to 0.1 mHz in GC GC cell (white circles). Fit using the equivalent circuit is shown in red. Adapted with permission from reference <sup>104</sup> . Copyright 2017 American Chemical Society.....	63
Figure 44: R <sub>ct</sub> and i <sup>0</sup> dependence upon the predominating polysulfide in the system. Each point is an average of at least 10 measurements. Reprinted with permission from reference <sup>104</sup> . Copyright 2017 American Chemical Society. ....	63
Figure 45: a) Drift of EIS spectra of a Pt Pt cell containing 0.01 M Li <sub>2</sub> S <sub>4</sub> in TEGDME:DOL 1:1 (v:v) measured from 1 MHz to 1 mHz b) drift in UV-vis spectra measured every 80 minutes reflecting a change of concentration of species, c) colour of the separator 95 h after cell assembly, d) a freshly prepared cell with the same electrolyte composition.....	64
Figure 46: a) Relative change of the charge transfer resistance for selected polysulfides and polysulfide pairs (total nominal concentration of 0.1 M) during EIS measurements on GC GC cells, b) time evolution of the impedance spectra of the 0.09 M Li <sub>2</sub> S <sub>6</sub> /0.01 M Li <sub>2</sub> S <sub>7</sub> pair in 1 M LiTFSI in TEGDME:DOL 1:1 (v:v).....	65

- Figure 47: a) Experimental values of  $R_{ct}$  (points) at different molar ratios of  $S_7^{2-}$  and  $S_8^{2-}$ . Simulated curves for the reaction given by Equation 15 (red) and Equation 18 (blue). b) Different degrees of disproportionation of  $S_7^{2-}$  (20% to 80% in steps of 20%). c)  $R_{ct}$  variation with degree of disproportionation. The numbers refer to the percentage of the oxidized form in the initial mixture. d)  $R_{ct}$  dependence on the initial concentration of the polysulfide ( $S_4^{2-}$ , circles). Fitting with two curves as explained in the text. Adapted with permission from reference <sup>104</sup>. Copyright 2017 American Chemical Society. .... 67
- Figure 48: Diffusion resistance dependence on the concentration of polysulfides ( $S_4^{2-}$ ). Concentrations to 0.032 M are displayed, since determination became unreliable due to the contribution of  $R_{ct}$  prevailing. Adapted with permission from reference <sup>104</sup>. Copyright 2017 American Chemical Society. .... 68
- Figure 49: Limitations and instability issues in measuring the diffusional arc. .... 69
- Figure 50: a) Impedance spectra of symmetrical carbon cells with 0.1 M  $Li_2S_4$  in 1 M LiTFSI TEGDME:DOL 1:1 (v:v) at OCV between 1 MHz and 0.1 mHz. b) magnification of the high frequency part of the spectra, c) SEM image of the GC electrode, d) SEM image of the H14 carbon felt electrode, e) SEM image of the ENSACO 350G porous electrode, f) values for the electrode specific surface areas and reaction contribution parameters. \*value for  $R_{CT}$  for GC electrode is an average due to large disproportionation change. .... 71
- Figure 51: a) discharge and charge voltage profile during impedance spectra measurements on a conventional cell assembled with 1 M LiTFSI in TEGDME:DOL 2:1 electrolyte (60  $\mu$ L/mg S) and glassy fibre separator; b) impedance spectra change during the first discharge and c) charge. The electrode size was 1.5 cm<sup>2</sup>. .... 72
- Figure 52: a) and c): Discharge voltage profiles of GC | Li and H14 | Li cells assembled with a Celgard separator and 10  $\mu$ L or 40  $\mu$ L of 0.1 M  $Li_2S_4$  in 1 M LiTFSI in TEGDME:DOL 1:1 (v:v), respectively. b) and d): Impedance spectra at various DOD after 15 minutes of relaxation. Inset show the Li anode contribution. .... 73
- Figure 53: a) Voltage vs. time dependence during dynamic impedance measurement on a GC | Li cell with 10  $\mu$ L of 0.1 M  $Li_2S_4$  in 1 M LiTFSI in TEGDME:DOL 1:1 (v:v). Current was C/20, alternating current amplitude C/200, frequency range between 1 MHz to 2 mHz. b) Corresponding impedance spectra during discharge. .... 74
- Figure 54: a) Total current transient for the ACV measurement and the excitation potential signal as a function of time and  $E_{dc}$  component b) magnitude of the ac component of the current. The dc part of the potential was scanned with 0.05 mV/s to 1.5 V versus Li/Li<sup>+</sup> starting at the OCV potential of 2.31 V vs. Li/Li<sup>+</sup>, the amplitude of the superimposed voltage sinusoidal signal was 10 mV (rms) and frequency 5 mHz. .... 75
- Figure 55: Discharge of a GC | Li cell with 10  $\mu$ L of 0.5 M  $Li_2S_4$  catholyte solution in the supporting electrolyte. a) Potential and current transient during deposition of  $Li_2S$ . b) SEM image of the film deposit on the GC electrode formed by the procedure in a). c) cross-section of the deposit on the GC electrode showing a porous and thick film in the size order of 1  $\mu$ m. d) Impedance spectrum of a GC | Li cell after film deposition e) Comparison of GC | Li cell

impedance before film deposition (fresh) and after film deposition, when fresh catholyte solution (additional 10 $\mu\text{L}$ of 0.5 M $\text{Li}_2\text{S}_4$ catholyte solution) was added. ....	76
Figure 56: Impedance spectra of fresh and discharged H14   Li cell assembled with 40 $\mu\text{L}$ of 0.1 M $\text{Li}_2\text{S}_4$ catholyte solution in the supporting electrolyte. a) Impedance spectra of a H14(film)   Li cell after electrochemical film deposition similar to Figure 55a, b) impedance spectra of fresh H14   Li cell and a discharged H14   Li cell with a film deposit, where fresh catholyte has been added. Note the size difference of the $R_{CT}$ between the fresh cell and the discharged cell with fresh catholyte added. ....	77
Figure 57: SEM images of the film deposit on a glassy carbon electrode, where fresh catholyte solution has been added – a) and b) different magnifications of top down view indicating islands of thicker deposit; c) magnification of the area indicated in b) with asterisks marking bright spots, where the film deposit was very thin. According to this analysis we estimated the amount of accessible surface area of the electrode to between 5 and 15%; d) and e) top down view and the corresponding cross section of a part where a thicker “island” deposit of approx. 900 nm thickness can be seen, note the porous structure of the film; f), g), h) and i) top down view and the cross section view of two different spots where thinner (100 nm) film is evident. The asterisks mark the spots where the film is likely below 10 nm thickness and reaction can take place (in correspondence with asterisks from c)).....	78
Figure 58: SEM images of the film deposit on a carbon felt electrode, where fresh catholyte solution has been added (Figure 56) – a) and b) different magnifications of thin film deposit; c) and d) porous structure of a thicker deposit; e and f) large particle-like deposit. ....	79
Figure 59: LTO addition to the Li-S battery cell. a) electrochemical discharge and charge with electrochemical response of both redox active materials in the composite electrode, b) fresh electrode with arrows pointing to the LTO particles, c) and d) discharged electrode showing large deposits of $\text{Li}_2\text{S}$ . ....	80
Figure 60: a) Electrochemical discharge with different current densities, b)-d) top down view of different size deposits, e-g) cross sections of ENSACO porous electrodes discharged at C/3, C/10 and C/100 current, respectively, h) and i) 3D reconstructed image of the cathode discharged at C/100. $\text{Li}_2\text{S}$ film in red, porous carbon in light blue and open pore structure in dark blue. Blue spots on the surface show parts of the carbon electrodes not covered with the film.....	82
Figure 61: Simplified schematic representation of major conclusions from this doctoral thesis work.....	84

## 9 List of tables

Table 1: Densities of [DEME][TFSI] and dioxolane at various molar ratios at temperatures between 278.15 K and 313.15 K.....	32
Table 2: Dynamic viscosities of [DEME][TFSI] and dioxolane at various molar ratios at temperatures between 278.15 K and 313.15 K.....	32
Table 3: Conductivities of [DEME][TFSI] and dioxolane at various molar ratios at temperatures between 278.15 K and 313.15 K.....	33
Table 4: Densities of [DEME][TFSI] and dioxolane at various molar ratios and different LiTFSI salt concentrations at temperatures between 278.15 K and 313.15.....	34
Table 5: Kinematic viscosities of [DEME][TFSI] and dioxolane at various molar ratios and different LiTFSI salt concentrations at temperatures between 278.15 K and 313.15.....	35
Table 6: Conductivities of [DEME][TFSI] and dioxolane at various molar ratios and different LiTFSI salt concentrations at temperatures between 278.15 K and 313.15 .....	35
Table 7: Diffusion parameters for GC   GC cells with different types of separator. 0.05 M Li <sub>2</sub> S <sub>6</sub> 0.05 M Li <sub>2</sub> S <sub>8</sub> in 1 M LiTFSI in TEGDME:DOL 1:1 (v:v) was used. Reprinted with permission from reference <sup>123</sup> . Copyright 2017 American Chemical Society.....	70

## 10 Attachments

Copyright permission for reprinting and adaptation of figures and tables from Drvarič Talian, S; Moskon, J; Dominko, R; Gaberscek, M: Reactivity and Diffusivity of Li Polysulfides: A Fundamental Study Using Impedance Spectroscopy. *ACS Appl. Mater. Interfaces*, **2017**, *9*, 29760–29770, IF 7.5.



RightsLink®

Home

Create Account

Help



ACS Publications  
Most Trusted. Most Cited. Most Read.

**Title:** Reactivity and Diffusivity of Li Polysulfides: A Fundamental Study Using Impedance Spectroscopy  
**Author:** Sara Drvarič Talian, Jože Moškon, Robert Dominko, et al  
**Publication:** Applied Materials  
**Publisher:** American Chemical Society  
**Date:** Sep 1, 2017

Copyright © 2017, American Chemical Society

LOGIN

If you're a copyright.com user, you can login to RightsLink using your copyright.com credentials. Already a RightsLink user or want to [learn more?](#)

### PERMISSION/LICENSE IS GRANTED FOR YOUR ORDER AT NO CHARGE

This type of permission/license, instead of the standard Terms & Conditions, is sent to you because no fee is being charged for your order. Please note the following:

- Permission is granted for your request in both print and electronic formats, and translations.
- If figures and/or tables were requested, they may be adapted or used in part.
- Please print this page for your records and send a copy of it to your publisher/graduate school.
- Appropriate credit for the requested material should be given as follows: "Reprinted (adapted) with permission from (COMPLETE REFERENCE CITATION). Copyright (YEAR) American Chemical Society." Insert appropriate information in place of the capitalized words.
- One-time permission is granted only for the use specified in your request. No additional uses are granted (such as derivative works or other editions). For any other uses, please submit a new request.

If credit is given to another source for the material you requested, permission must be obtained from that source.

BACK

CLOSE WINDOW

Copyright © 2018 Copyright Clearance Center, Inc. All Rights Reserved. [Privacy statement](#). [Terms and Conditions](#). Comments? We would like to hear from you. E-mail us at [customercare@copyright.com](mailto:customercare@copyright.com)